Neutron scattering on strongly correlated electron systems: MnSi, $CeCu_{5.5}Au_{0.5}$, $La_{2-x}Sr_xCuO_4$ and $HgBa_2CuO_{4+\delta}$

Zur Erlangung des akademischen Grades eines

DOKTORS DER NATURWISSENSCHAFTEN

von der Fakultät für Physik des
Karlsruher Institut für Technologie (KIT)

genehmigte

DISSERTATION

von

Dipl.-Phys. Andreas Hamann
aus Saarbrücken

Tag der mündlichen Prüfung: 16.07.2010

Referent: Prof. Dr. H. v. Löhneysen
Korreferent: Prof. Dr. G. Weiß

Contents

Introduction

Neutron scattering is an extremely powerful and versatile tool for exploring crystal and magnetic structures as well as their excitations in solids. Consequently, it allows to study a plethora of phenomena in condensed matter physics. In this work, neutron scattering is used to investigate strongly correlated electron systems. Owing to the strong interaction between their electrons, it is not evident whether the Fermi liquid (FL) theory while successfully describing ordinary metals [1, 2] is applicable to these systems, too. In the following, three different classes of materials will be investigated each of which reveals a variety of intriguing properties that cannot be explained by the FL theory.

In the first chapter, the basic concepts of neutron scattering with a triple-axis spectrometer are briefly introduced. Further, all formulas required for the data analysis in the following chapters are provided. Special emphasis is laid on discussing the experimental resolution and how it is to be taken into account in the data evaluation.

The second and largest chapter is devoted to the weak itinerant magnet MnSi. Below the Curie-temperature $T_C = 29.5\,\mathrm{K}$ magnetic moments order in a helical arrangement with a very long wavelength of about $180\,\mathrm{\AA}$ and the axis locked along a favored direction. The electrical resistivity reveals a T^2 dependence below T_C as expected for a Fermi liquid. Hydrostatic pressure continuously reduces T_C, resulting in a 'quantum critical point' (QCP) at $p_c = 14.6\,\mathrm{kbar}$, i.e., a magnetic instability where $T_C = 0$. For pressures $p \gtrsim p_c$ a hitherto unique magnetic state, so-called 'partial magnetic order', has been found with long-range helical correlations but disordered propagation directions [3]. Significant deviations from FL behavior, nicknamed non-FL (NFL) behavior, appear nearby in the phase diagram. Previous measurements [4] pointed towards a similar magnetic state present at ambient pressure just above T_C. We investigated the temperature dependent dynamics of the magnetic correlations by means of quasielastic scattering of ultra-high resolution. In order to explain not only our experimental findings but other unusual properties as well, we performed calculations on finite-size spin clusters modeling MnSi. In fact, our results elucidate many anomalous features on a qualitative basis.

The third chapter addresses the pressure dependence of magnetic order in the heavy fermion (HF) system $CeCu_{6-x}Au_x$. The undoped ($x = 0$) parent compound $CeCu_6$

does not order magnetically and is rather well described by FL theory. Doping with Au introduces long-range antiferromagnetism (AF) for $x > x_c \approx 0.1$ with a Néel temperature $T_{\mathrm{N}}(x)$ increasing linearly with x up to $x = 1$. In the vicinity of the quantum critical point at $x = x_c$ (where $T_{\mathrm{N}}(x)$ vanishes) NFL behavior has been observed in macroscopic quantities such as thermodynamic and transport properties [5, 6]. The magnetic ground state can be tuned not only by Au concentration x but also by applying hydrostatic pressure p or a magnetic field B. Pressure reverses the effect of Au doping and hence reduces $T_{\mathbf{N}}$ of magnetically ordered $CeCu_{6-x}Au_x$ with $x > 0.1$. Adjusting the pressure appropriately even drives $T_{\mathbf{N}}$ to zero resulting in a 'p-tuned' QCP at $x > x_c$. Remarkably, the NFL behavior at the respective 'p-tuned' QCP has been found to be identical to the 'x-tuned' QCP at $x = x_c$ and ambient pressure, indicating a striking equivalence of the tuning behavior with x or p. In this work we tested whether this equivalence holds on a microscopic level, i.e., by virtue of the magnetic ordering wave vector $\mathbf{q}_m$. Previous experiments with neutrons [7] revealed an abrupt variation of $\mathbf{q}_m$ between $x = 0.4$ and $x = 0.5$ at ambient pressure. Therefore, we investigated the pressure dependence of $\mathbf{q}_m$ in $CeCu_{5.5}Au_{0.5}$ with elastic neutron scattering to see whether $\mathbf{q}_m$ corresponding to $x = 0.4$ can be recovered by applying pressure which would corroborate the x - p equivalence even far away from the QCP.

The fourth chapter deals with phonon anomalies in cuprate high-T_c superconductors (HTSC). Conventional superconductivity is mediated by phonons as described by the Bardeen-Cooper-Schrieffer (BCS) theory from 1957 [8]. Therefore, the role of phonons in the mechanism of HTSC has been considered very early. As one could not think of electron-phonon coupling with a strength leading to transition temperatures near 100 K, phonons were discarded and the main focus of research was on magnetic mechanisms. The discovery of anomalous behavior of certain lattice vibrations, somehow related to superconductivity, led to a renewed interest in phonon-mediated coupling and triggered a systematic study of phonons in many cuprate compounds [9, 10]. One of the most extensively studied systems is $La_{2-x}Sr_xCuO_4$ (LSCO) where superconductivity is found for $0.06 \leq x < 0.3$. In the optimally doped system with $x = 0.15$ a very pronounced phonon anomaly was observed which is absent in overdoped non-superconducting LSCO with $x = 0.3$, indicating a close link to superconductivity. However, it remains to be shown that the phonon anomaly vanishes in underdoped non-superconducting systems ($x < 0.06$), too. This was done in this work by means of inelastic neutron scattering. We further performed a study of another cuprate superconductor, i.e., $HgBa_2CuO_{4+\delta}$ (Hg1201), for which a similar phonon anomaly had been reported in the literature [11] but only data of marginal quality had been presented. Due to the small size of available samples, we had to use inelastic X-ray scattering instead of neutron scattering.

Chapter 1

Experimental method

Neutron scattering is an extremely powerful and versatile technique for exploring condensed matter. This was generally recognized by the awarding of the Nobel Prize in Physics in 1994 to C. G. Shull (MIT, USA) and B. N. Brockhouse (McMaster University, Canada) "for their pioneering contributions to the development of elastic and inelastic neutron scattering" [12]. Among a variety of scattering instruments which are widely discussed in literature [13, 14, 15], the most important turned out to be the triple-axis spectrometer (TAS): It allows for a well defined measurement of the scattering function $S(\mathbf{Q}, \omega)$ in momentum ($\hbar\mathbf{Q}$) and energy ($\hbar\omega$) space and thereby enables one to study nuclear and magnetic structures as well as their excitations.

Several physical properties of the neutron make it an ideal probe with which to investigate solids and liquids (see Tab. 1.1). Since its mass m_n is close to that of the proton, high energy neutrons from the reactor core can be moderated by multiple scattering from atoms of comparable mass. The temperature T of the moderating medium in turn defines the Maxwellian velocity distribution of the thermalized neutron beam

$$\Phi(v) \propto v^3 \exp\left(-\frac{mv^2}{2k_\mathrm{B}T}\right) , \tag{1.1}$$

where $\Phi(v)dv$ is the neutron flux, i.e., the number of neutrons per unit area per second with velocities between v and $v + dv$. It assumes its maximum at

$$v = \sqrt{\frac{3k_\mathrm{B}T}{m}} , \tag{1.2}$$

corresponding to a kinetic energy of

$$E = \frac{1}{2}m_\mathrm{n}v^2 = \frac{\hbar^2k^2}{2m_\mathrm{n}} = \frac{h^2}{2m_\mathrm{n}\lambda^2} = \left(\frac{3}{2}\right)k_\mathrm{B}T . \tag{1.3}$$

Following usual conventions, the factor 3/2 is omitted in the following such that a neutron with energy E corresponds to a temperature $T = E/k_\mathrm{B}$. Thus, the temperature

Quantity	Value at $E = 10\,\mathrm{meV}$
Mass m_n	$1.675 \cdot 10^{-27}\,\mathrm{kg}$
Spin	1/2
Magnetic moment μ_n	-1.913 nuclear magnetons, μ_n
Charge	0
Wavelength λ	$2.86\,\mathrm{\AA}$
Wave vector k	$2.20\,\mathrm{\AA}^{-1}$
Velocity v	$1.38\,\mathrm{km\,s^{-1}}$
Temperature T	$116.05\,\mathrm{K}$

Table 1.1: Properties of neutrons with $E = 10\,\mathrm{meV}$. Note that the wavelength is of the order of typical interatomic distances in solids. Values have been adopted from Table 1.5 in [13].

of the moderator can be chosen appropriately to match the wavelength and energy scale of interest, e.g., for studying phonons or spin waves in solids. Generally, three types of sources are to be mentioned: Cold, thermal and hot sources use moderators at typical temperatures of about 20 K, 300 K or 2000 K to produce neutrons the energy distribution of which is peaked around 5 meV, 25 meV or 100 meV, respectively. Typical materials utilized as moderator are liquid H_2 (cold), liquid D_2O (thermal) or a block of graphite (hot).

Despite the charge of the three valence quarks that build the neutron, its net charge is zero. As an important consequence, the neutron interacts only very weakly with electrons and atomic nuclei and thus penetrates deeply into the sample. Essentially, it interacts with the nuclei of the atoms on a length-scale of 1 fm, which can be considered point-like for the purpose of most experiments. The description of this isotropic neutron-nucleus interaction is provided by a single parameter, the so called scattering length b, that characterizes the scattering cross section for a single nucleus to be $4\pi b^2$. Typical values of the scattering length for most atoms are of order $10^{-14}\,\mathrm{m}$.

On the other hand, the neutron's internal substructure of quarks results in a net spin 1/2 that couples to magnetic moments of unpaired electrons or magnetic atoms. Hence, in addition to nuclear phenomena, magnetic structures can be investigated as well. The effective magnetic scattering length p for a magnetic atom with a moment of $1\,\mu_\mathrm{B}$ is of the same order of magnitude as b, i.e., magnetic scattering is typically comparable in intensity with nuclear scattering. By controlling and analyzing the neutron's polarisation it is even possible to distinguish between nuclear and magnetic contributions to the scattering intensity.

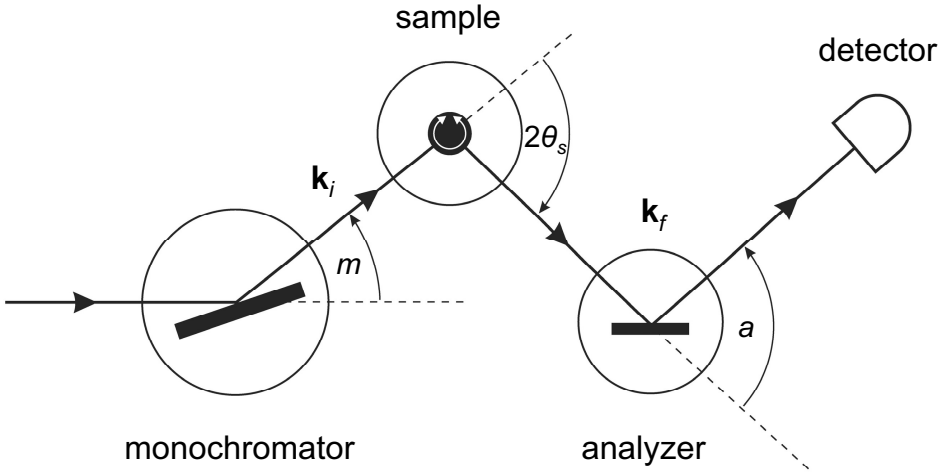

Figure 1.1: General beam path of the neutrons at a triple-axis spectrometer as adopted from [16]. The three axes are called monochromator-axis (variation of $\mathbf{k}_i$), sample-axis (variation of the scattering angle $2\theta_s$, i.e., the direction of $\mathbf{k}_f$) and analyzer-axis (variation of the final energy E_f, i.e., $k_f := ||\mathbf{k}_f||$).

In this chapter, the basic concepts of neutron scattering with a TAS are briefly introduced following closely the more general discussion of [13, 14]. Giving detailed derivations is beyond the scope of this work, instead emphasis is laid on quickly providing all formulas required for the analysis of the data hereinafter.

1.1 Conventions

Fig. 1.1 shows the schematic setup of a triple-axis spectrometer (TAS). Thermalized neutrons from the reactor core are monochromatized by Bragg scattering from the monochromator crystal. The resulting beam is characterized by wave vector $\mathbf{k}_i$ (incident) and hits the sample. After interaction with its structure, the outgoing beam is Bragg scattered one more time at the analyzer crystal before the neutron intensity is measured in the detector. Appropriate setting of $2\theta_s$ and a with respect to the crystallographic orientation of the sample allows to control $\mathbf{k}_f$ (final) and thereby define the momentum and energy transfer to the sample:

$$\begin{aligned} \mathbf{Q} &:= \mathbf{k}_f - \mathbf{k}_i && \text{(momentum transfer)} \\ \hbar\omega &:= \frac{\hbar^2}{2m_\mathrm{n}} \left(\mathbf{k}_i^2 - \mathbf{k}_f^2\right) && \text{(energy transfer)} . \end{aligned} \tag{1.4}$$

Elastic scattering (diffraction) implies $||\mathbf{k}_i|| = ||\mathbf{k}_f|| =: k$ and $\hbar\omega = 0$. In this case,

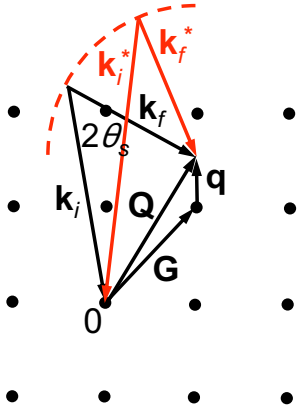

Figure 1.2: Vector diagram of inelastic scattering for neutron energy loss ($k_i > k_f$, compare Eq. (1.11)) as adopted from [13]. Zero defines the arbitrary origin of reciprocal space. Wave vectors shown in black are chosen such that the momentum $\mathbf{Q} = \mathbf{G} + \mathbf{q}$ is transferred to the sample. $\mathbf{G}$ denotes a reciprocal lattice vector and $\mathbf{q}$ represents the momentum transfer within a Brillouin zone such as mediated by a phonon or magnon. Red wave vectors $\mathbf{k}_i^*$ and $\mathbf{k}_f^*$ illustrate how another energy transfer $\hbar\omega$ can be measured while keeping $\mathbf{Q}$ const.: $\mathbf{k}_f^*$ is of the same exact length as $\mathbf{k}_f$ but $\mathbf{k}_i^*$ is much longer than $\mathbf{k}_i$ resulting in a higher energy transfer to the sample.

neutrons are scattered from the sample when satisfying the Bragg condition

$$\mathbf{Q} = \mathbf{G}\,, \tag{1.5}$$

with $\mathbf{G}$ being a reciprocal lattice vector. This can be beautifully illustrated in the concept of the Ewald circle. On the other hand, for geometrical reasons

$$||\mathbf{Q}|| = 2k\sin\theta_s \tag{1.6}$$

generally holds, such that

$$||\mathbf{G}|| = 2k\sin\theta_s \tag{1.7}$$

is another formulation of Eq. (1.5). It can be transformed to

$$\lambda = 2d_{hkl}\sin\theta_s\,, \tag{1.8}$$

when noting that

$$G_{hkl} = \frac{2\pi}{d_{hkl}}\,, \tag{1.9}$$

where d_{hkl} is the spacing of corresponding planes in real space that are defined by Miller indices h, k and l.

In the case of inelastic scattering (spectroscopy), momentum conservation requires

$$\mathbf{Q} = \mathbf{G} + \mathbf{q}\,. \tag{1.10}$$

For reasons that will be explained in Section 1.2.1.1 (Bose factor), the spectrometer is usually operated in the 'neutron energy loss mode' (Fig. 1.2). Following the conventions of Eq. (1.4), this means that the energy transfered to the sample is positive:

$$\hbar\omega = \frac{\hbar^2}{2m_\mathrm{n}}\left(\mathbf{k}_i^2 - \mathbf{k}_f^2\right) > 0 \quad \text{(neutron energy loss)}\,. \tag{1.11}$$

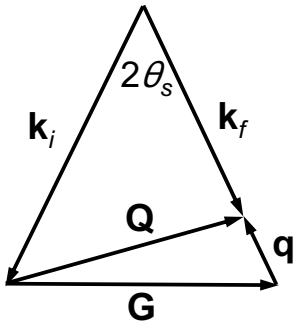

Figure 1.3: from [13]

Regarding a two-axis diffractometer where no analyzer crystal is used, final neutrons resulting from elastic as well as inelastic processes are detected together: all $\mathbf{k}_f$ that point into the same direction (i.e., into the detector) will contribute to the measured intensity, regardless of their length k_f (i.e., energy). This scenario is illustrated in Fig. 1.3, where $\mathbf{k}_f$ of the inelastic scattering process shown points into the same direction that the corresponding elastic $\mathbf{k}_f$ would with $\mathbf{q} = 0$ and $\mathbf{Q} = \mathbf{G}$. The two axis diffractometer corresponds to a TAS operated with $a = 0°$ (compare Fig. 1.1). However, the great advantage of a TAS is the opportunity of selecting the final energy of all neutrons reaching the detector. Therefore the inelastic process shown in Fig. 1.3 can be measured exclusively without elastic contribution. Since an inelastic signal is usually several orders of magnitude weaker in intensity than a nuclear Bragg peak, the energy discrimination provided by the analyzer axis has turned out to be key to investigating inelastic phenomena in condensed matter.

1.2 Scattering formulas

In triple-axis spectroscopy, the quantity measured always is the rate of neutrons that are scattered into a certain solid angle $d\Omega_f$ (in the direction $\mathbf{k}_f$) with energies between between E_f and $E_f + dE_f$. This rate is the product of the flux $\Phi(k_i)$ incident on the sample and the double-differential cross section $d^2\sigma/d\Omega_f dE_f$, which can be separated into the coherent and incoherent part:

$$\frac{d^2\sigma}{d\Omega_f dE_f} = \left(\frac{d^2\sigma}{d\Omega_f dE_f}\right)_{coh} + \left(\frac{d^2\sigma}{d\Omega_f dE_f}\right)_{incoh} . \tag{1.12}$$

Collective phenomena among different atoms contribute to the coherent part, regardless of whether they are elastic or inelastic. Examples of such collective effects are nuclear and magnetic Bragg scattering as well as inelastic scattering from phonons and magnons. For simplicity of describing the incoherent part, a scattering system consisting of a single element is considered. The incoherent scattering then results from a random distribution of different scattering lengths b_r, occurring in the sample with probability p_r. For instance, b_r can vary among different isotopes r or different nuclear spin states r of the the same element. The coherent part of the double-differential cross section depends on the average scattering length:

$$\sigma_{coh} = 4\pi \left(\sum_r p_r b_r\right)^2 = 4\pi \left(\bar{b}\right)^2 . \tag{1.13}$$

However, the total scattering cross section is given by

$$\sigma_{tot} = 4\pi \sum_r p_r b_r^2 = 4\pi \overline{b^2} \,. \tag{1.14}$$

Therefore, the incoherent contribution $\sigma_{incoh} = \sigma_{tot} - \sigma_{coh}$ can be understood as resulting from a non-zero variance ς of the distribution of the b_r:

$$\sigma_{incoh} = 4\pi \underbrace{\left(\overline{b^2} - \overline{b}^2\right)}_{\varsigma} \,. \tag{1.15}$$

Samples with strong incoherent scattering can be used to check the alignment of the spectrometer: For small Q and low temperatures, incoherent scattering from vanadium metal is roughly isotropic in space (i.e., $\mathbf{Q}$-independent) and fully elastic (i.e., $E = 0$). For this reason, an energy-scan on vanadium at any $\mathbf{Q}$ has to reveal a maximum of the scattering intensity at $E = 0$.[1] If this is not the case, the spectrometer is not well aligned.

In the rest of this chapter, the incoherent part of the double-differential cross section in Eq. (1.12) is neglected unless explicitly mentioned otherwise, and b denotes the mean value $\overline{b}$. Also, all formulas are derived assuming that the neutron scatters from the sample perturbing the system very weakly. This means that it changes the occupation of eigenstates $|\lambda\rangle$ but not the eigenstates themselves. Consequently, Fermi's Golden Rule can be used as a starting point:

$$\frac{d^2\sigma}{d\Omega_f dE_f} = \frac{k_f}{k_i} \left(\frac{m_\mathrm{n}}{2\pi\hbar^2}\right)^2 \left|\langle \mathbf{k}_f \lambda_f \sigma_f | V | \mathbf{k}_i \lambda_i \sigma_i \rangle\right|^2 \delta(\hbar\omega + E_i - E_f) \,. \tag{1.16}$$

Generally, the neutron is specified not only by its wavevector $\mathbf{k}$ but also by its spin state σ. The potential V describes the nature of the scattering process, particularly whether it is nuclear or magnetic. Because of the assumed weakness of the interaction, the interaction matrix element can usually be evaluated using the Born approximation, where incident and outgoing neutrons are treated as plane waves.

1.2.1 Nuclear scattering

Assuming that the nuclear scattering potential $V(\mathbf{r})$ is a delta function (Fermi pseudopotential), its Fourier transform $V(\mathbf{Q})$ in Eq. (1.16) is proportional to the scattering length b and one can finally show [13] that

$$\frac{d^2\sigma}{d\Omega_f dE_f} = N \frac{k_f}{k_i} b^2 S(\mathbf{Q}, \omega) \,, \tag{1.17}$$

[1] See Fig. 1.5 (b) that is explained in the corresponding section.

where N is the number of nuclei and S is the scattering function mentioned at the beginning of this chapter. Eq. (1.17) applies to samples consisting of a single element. Generally, site-dependent scattering lengths have to be included in the scattering function S (as will be the case from Section 1.2.1.1 on). Let $\mathbf{r}_l$ be the position vector of the lth nucleus and let $\langle \mathbf{A} \rangle$ denote the thermal average of the operator $\mathbf{A}$ at a temperature T, i.e.,

$$\langle \mathbf{A} \rangle = \sum_{\lambda_i} p(\lambda_i) \langle \lambda_i | \mathbf{A} | \lambda_i \rangle \,, \tag{1.18}$$

with $|\lambda_i\rangle$ being the initial eigenstate of the sample occurring with probability $p(\lambda_i)$. Then the coherent scattering function reads:

$$S(\mathbf{Q}, \omega) = \frac{1}{2\pi\hbar N} \sum_{ll'} \int_{-\infty}^{\infty} dt \left\langle e^{-i\mathbf{Q}\cdot\mathbf{r}_{l'}(0)} e^{i\mathbf{Q}\cdot\mathbf{r}_l(t)} \right\rangle e^{-i\omega t} \,. \tag{1.19}$$

Hence, coherent scattering describes interference effects by depending on the time-correlation of the positions of the same ($l = l'$) *and* different ($l \neq l'$) nuclei[2].

1.2.1.1 Elastic scattering

In case of elastic coherent scattering from a crystal that is characterized by a Bravais lattice and a polyatomic basis, the differential cross section is then given by

$$\left(\frac{d\sigma}{d\Omega} \right)_{el} \propto \sum_{\mathbf{G}} \delta(\mathbf{Q} - \mathbf{G}) |F_n(\mathbf{G})|^2 \,, \quad \text{where} \tag{1.20}$$

$$F_n(\mathbf{G}) = \sum_j b_j e^{i\mathbf{G}\cdot\mathbf{d}_j} e^{-W_j} \,. \tag{1.21}$$

The delta function is associated with the Bragg condition (Eq. (1.5)). The static nuclear structure factor $F_n(\mathbf{G})$ describes interference effects resulting from scattering off different atoms j at positions $\mathbf{d}_j$ within the unit cell. Furthermore, thermal fluctuations of the nuclei about respective equilibrium positions reduce the measured intensity. This effect is accommodated by the Debye-Waller factor $\exp(-2W)$, where

$$W = \frac{1}{2} \left\langle (\mathbf{Q} \cdot \mathbf{u})^2 \right\rangle \tag{1.22}$$

and $\mathbf{u}$ denotes the instantaneous displacement of the nuclei from their equilibrium positions.

[2] On the contrary, incoherent scattering is described by the same Eq. (1.19) but summing exclusively over the temporal correlation of the positions of the *same* nuclei, thus neglecting interference effects.

1.2.1.2 Inelastic scattering

If during the scattering process the neutron loses the energy $\hbar\omega$, this energy is transferred to the sample causing a transition between any pairs of energy levels that are separated by $\hbar\omega$. The reverse process where the neutron gains energy is also possible, causing a transition between the same pairs of levels, but now the energy of the initial state is higher than the energy of the final state. The probability of the system being initially in the higher energy state is lower than its probability of being in the lower energy state, i.e., excitation creation is more likely that excitation annihilation. This fact is taken into account by the principle of detailed balance:

$$S(-\mathbf{Q}, -\omega) = e^{-\frac{\hbar\omega}{k_\mathbf{B}T}} S(\mathbf{Q}, \omega) \,. \tag{1.23}$$

Furthermore, the scattering amplitude S is related to the imaginary part of the dynamical susceptibility $\chi''(\mathbf{Q}, \omega)$ via the fluctuation-dissipation theorem:

$$S(\mathbf{Q}, \omega) = \frac{1}{1 - e^{-\frac{\hbar\omega}{k_\mathbf{B}T}}} \chi''(\mathbf{Q}, \omega) \,. \tag{1.24}$$

Phonons

Phonons are quantized excitations of the crystal lattice. Their bosonic nature forces them to obey the Bose statistics, where the Bose factor gives the average occupation of a state with energy $\hbar\omega$ at a temperature T:

$$n(\omega, T) = \frac{1}{e^{\frac{\hbar\omega}{k_\mathbf{B}T}} - 1} \,. \tag{1.25}$$

A crystal containing $\mathcal{N}$ unit cells with p atoms per unit cell has $3p$ phonon branches each of which consists of $\mathcal{N}$ modes. The relation between the momentum $\hbar\mathbf{q}$ and the $3p$ possible energies $\hbar\omega_{\mathbf{q}s}$ is provided by the dispersion of respective branches, labeled with the number s. At a particular $\mathbf{q}$, each phonon mode is characterized by its polarization vectors (eigenvectors) ξ_{js} . Modes with $\xi||\mathbf{q}$ are called longitudinal and those with $\xi\perp\mathbf{q}$ are called transverse. In case of neutron scattering from phonons, the imaginary part of the dynamical susceptibility reads

$$\chi''(\mathbf{Q}, \omega) \propto \sum_{\mathbf{G},\mathbf{q}} \delta(\mathbf{Q} - \mathbf{q} - \mathbf{G}) \sum_s \frac{1}{\omega_{\mathbf{q}s}} |\mathcal{F}(\mathbf{Q})|^2 \cdot \big[\underbrace{\delta(\omega - \omega_{\mathbf{q}s})}_{\substack{\text{neutron} \\ \text{energy loss}}} - \underbrace{\delta(\omega + \omega_{\mathbf{q}s})}_{\substack{\text{neutron} \\ \text{energy gain}}} \big] \,, \tag{1.26}$$

where the dynamic structure factor $\mathcal{F}(\mathbf{Q})$ is given by

$$\mathcal{F}(\mathbf{Q}) = \sum_j \frac{b_j}{\sqrt{m_j}} (\mathbf{Q} \cdot \xi_{js}) e^{i\mathbf{Q}\cdot\mathbf{d}_j} e^{-W_j} \,. \tag{1.27}$$

The first delta function accommodates the conservation of momentum (Eq. (1.10)), the second and third one distinguish between creation and annihilation of phonons. Note that χ'' is inversely proportional to the phonon frequencies $\omega_{\mathbf{q}s}$. In comparison to the static structure factor F_n (Eq. (1.38)), the dynamic structure factor $\mathcal{F}$ contains some additional elements, namely the mass of the jth atom m_j and the scalar product $\mathbf{Q} \cdot \xi_{js}$. Due to this product, an appropriate choice of scans in different Brillouin zones often allows to determine phonon eigenvectors: Only the component of the eigenvector that is parallel to $\mathbf{Q}$ contributes to the scattering intensity. In the simple case of long-wavelength acoustic modes, where all atoms are moving in phase, $\mathbf{Q}||\mathbf{q}$ would detect the longitudinal mode (ξ_L) only, because $\mathbf{q}||\xi_L$ and $\mathbf{Q} \cdot \xi_L \neq 0$ as opposed to the transverse mode (ξ_T) where $\mathbf{q} \perp \xi_T$ and therefore $\mathbf{Q} \cdot \xi_T = 0$.

The minus sign between the delta functions in Eq. (1.26) results from the principle of detailed balance requiring that $\chi''(\mathbf{Q}, \omega)$ be odd in ω in cases where $S(-\mathbf{Q}, \omega) = S(\mathbf{Q}, \omega)$. A priori, χ'' is neither temperature dependent, nor does it implicate different probabilities for processes where the neutron gains or loses energy. Inserting Eq. (1.26) into Eq. (1.24) and noting that

$$1 + n(\omega, T) = -n(-\omega, T) \tag{1.28}$$

holds for all ω reveals

$$\begin{aligned} S(\mathbf{Q}, \omega) \quad \propto \quad & \sum_{\mathbf{G},\mathbf{q}} \delta(\mathbf{Q} - \mathbf{q} - \mathbf{G}) \sum_s \frac{1}{\omega_{\mathbf{q}s}} |\mathcal{F}(\mathbf{Q})|^2 \cdot \\ & \cdot \Big[\underbrace{\big(1 + n(\omega_{\mathbf{q}s}, T)\big) \cdot \delta(\omega - \omega_{\mathbf{q}s})}_{\text{neutron energy loss}} + \underbrace{\big(n(\omega_{\mathbf{q}s}, T)\big) \cdot \delta(\omega + \omega_{\mathbf{q}s})}_{\text{neutron energy gain}} \Big] . \end{aligned} \tag{1.29}$$

Here, the different statistical weight of neutron energy gain and loss becomes obvious: At low temperatures (i.e., $\hbar_{\mathbf{q}s}\omega \gg k_\mathrm{B}T$), $n_{\mathbf{q}s} \approx 0$ and neutron energy gain processes are very unlikely because there are only very few excitations to be annihilated. On the other hand, at high temperatures (i.e., $\hbar_{\mathbf{q}s}\omega \ll k_\mathrm{B}T$), $n_{\mathbf{q}s} \approx 1 + n_{\mathbf{q}s} \approx k_\mathrm{B}T/\hbar\omega_{\mathbf{q}s}$ resulting in an equal probability for excitation creation and annihilation. Since neutron experiments investigating condensed matter usually have to be performed at low temperatures to scatter from ordered phases, the spectrometer is mostly operated in the 'neutron energy loss mode'.

All delta functions in the second line of Eq. (1.29) model the hypothetical case of infinite lifetimes of the phonons. However, in real systems, the lifetime of phonons becomes finite due to phonon-phonon interaction (anharmonicity effects), electron-phonon interaction as well as crystal imperfections. In the first approximation, the time dependent decay of phonons is described by an exponential function of which the Fourier transform is Lorentzian. Hence, Lorentzian energy distributions are used in

Eq. (1.29) instead of delta functions to model the intrinsic lineshape of phonons:

$$\delta(\omega \pm \omega_{\mathbf{q}s}) \rightarrow L(\omega; \omega_{\mathbf{q}s}, \Gamma_{\mathbf{q}s}) = \underbrace{A \cdot \frac{2}{\pi\Gamma_{\mathbf{q}s}}}_{\text{amplitude}} \cdot \frac{\left(\frac{\Gamma_{\mathbf{q}s}}{2}\right)^2}{(\omega - \omega_{\mathbf{q}s})^2 + \left(\frac{\Gamma_{\mathbf{q}s}}{2}\right)^2} \,. \tag{1.30}$$

A denotes the area of the Lorentzian and its full-width at half-maximum (FWHM) is given by $\Gamma_{\mathbf{q}s}$. In the damped harmonic-oscillator model [17], the phonon frequencies $\omega_{\mathbf{q}s}$ are simultaneously substituted by renormalized frequencies $\omega'_{\mathbf{q}s}$:

$$\omega_{\mathbf{q}s} \rightarrow \omega'_{\mathbf{q}s} = \sqrt{\omega_{\mathbf{q}s}^2 - \left(\frac{\Gamma_{\mathbf{q}s}}{2}\right)^2} \,. \tag{1.31}$$

In this work, frequencies of investigated phonons are usually much bigger than their FWHM rendering a discrimination between $\omega'_{\mathbf{q}s}$ and $\omega_{\mathbf{q}s}$ unnecessary. In addition, the most interesting parameter that is to be extracted from the data with high precision is the phonon's intrinsic linewidth which is not dependent on ω.

1.2.2 Magnetic scattering

In order to derive the double differential cross section for magnetic scattering, the interaction matrix element in Eq. (1.16) has to be evaluated regarding the appropriate magnetic potential $V = V_m$. It is assumed that the neutron scatters from the localized magnetic moments of atoms. Furthermore, a weak dipole-dipole interaction of the neutron with the magnetic atom is considered. A discussion of the general case where the magnetic atoms carry spin and orbital momentum can be found in [14]. Regarding this work, the restriction to spin only is sufficient to describe investigated phenomena. Analogous to Eqs. (1.17) and (1.19), the scattering of unpolarized neutrons from a system consisting of a single element is considered in the following, until mentioned otherwise. In this case, the magnetic scattering length p has to be not included in the scattering function S but appears as factor in the double differential cross section, just as b does in Eq. (1.17). It is defined by the magnetic form factor $f(\mathbf{Q})$,

$$p = \gamma r_0 \underbrace{\int \rho_s(\mathbf{r}) e^{i\mathbf{Q}\cdot\mathbf{r}} d\mathbf{r}}_{f(\mathbf{Q})} \,, \tag{1.32}$$

where $\rho_s(\mathbf{r})$ is the spin density, r_0 is the classical electron radius and $\gamma = 1.913$ denotes the gyromagnetic ratio. Furthermore, only the component of the spin $\mathbf{s}$ perpendicular to $\mathbf{Q}$ contributes to the measured intensity:

$$\mathbf{s}_\perp = \mathbf{s} - \hat{\mathbf{Q}}(\hat{\mathbf{Q}} \cdot \mathbf{s}) \,, \quad \text{with} \quad \hat{\mathbf{Q}} := \frac{\mathbf{Q}}{||\mathbf{Q}||} \,. \tag{1.33}$$

Noting that

$$||\mathbf{s}_\perp||^2 = \sum_{\alpha,\beta} \left(\delta_{\alpha\beta} - \hat{Q}_\alpha \hat{Q}_\beta\right) s^*_\alpha s_\beta \,, \tag{1.34}$$

where α and β label x, y, z components, the double differential cross section reads:

$$\begin{aligned} \frac{d^2\sigma}{d\Omega_f dE_f} &= \frac{N}{\hbar}\frac{k_f}{k_i} p^2 e^{-2W} \sum_{\alpha,\beta} \left(\delta_{\alpha\beta} - \hat{Q}_\alpha \hat{Q}_\beta\right) s^{\alpha\beta}(\mathbf{Q},\omega) \,, \quad \text{with} \\ & s^{\alpha\beta}(\mathbf{Q},\omega) = \frac{1}{2\pi}\int_{-\infty}^{\infty} dt\, e^{-i\omega t} \sum_l e^{i\mathbf{Q}\cdot\mathbf{r}_l} \left\langle s_0^\alpha(0) s_l^\beta(t)\right\rangle \,. \end{aligned} \tag{1.35}$$

Angle brackets $\langle \cdots \rangle$ are defined in Eq. (1.18), e^{-2W} is the Debye-Waller factor and l labels lattice sites. In the case of static spins, Eq. (1.35) can be reduced to

$$\begin{aligned} \frac{d^2\sigma}{d\Omega_f dE_f} \propto\ & \frac{k_f}{k_i} \sum_{\alpha,\beta} \left(\delta_{\alpha\beta} - \hat{Q}_\alpha \hat{Q}_\beta\right) \sum_{l,l'} \sum_{\lambda_i,\lambda_f} p(\lambda_i) \langle \lambda_i | e^{-i\mathbf{Q}\cdot\mathbf{r}_{l'}} s^\alpha_{l'} | \lambda_f \rangle \cdot \\ & \cdot \langle \lambda_f | e^{i\mathbf{Q}\cdot\mathbf{r}_l} s^\beta_l | \lambda_i \rangle \cdot \delta(E_{\lambda_i} - E_{\lambda_f} + \hbar\omega) \,. \end{aligned} \tag{1.36}$$

Since a weak interaction of the neutron with the magnetic atom is considered, initial and final states $|\lambda_{i,f}\rangle$ differ only in the orientations of the spins and the positions of the nuclei. However, the spin quantum number is conserved.

1.2.2.1 Elastic scattering

In case of elastic magnetic scattering from a magnetically ordered crystal that is characterized by a Bravais lattice and a polyatomic basis, the differential cross section is given by

$$\left(\frac{d\sigma}{d\Omega}\right)_{el} \propto \sum_{\mathbf{G}_m} \delta(\mathbf{Q} - \mathbf{G}_m) |F_m(\mathbf{G}_m)|^2 \,, \quad \text{where} \tag{1.37}$$

$$F_m(\mathbf{G}_m) = \sum_j p_j \mathbf{s}_{\perp j} e^{i\mathbf{G}_m\cdot\mathbf{d}_j} e^{-W_j} \,. \tag{1.38}$$

The delta function is associated with the Bragg condition (Eq. (1.5)) involving the *magnetic* reciprocal lattice vector $\mathbf{G}_m$. Due to the magnetic unit cell usually being larger than the chemical unit cell, typically $\mathbf{G}_m$ is smaller than $\mathbf{G}$. The static magnetic structure factor $F_m(\mathbf{G}_m)$ describes interference effects resulting from scattering off different atoms j at positions $\mathbf{d}_j$ within the magnetic unit cell.

1.2.2.2 Inelastic scattering

Let T_c denote the temperature of the magnetic phase transition. At temperatures $T < T_c$, magnetic moments fluctuate in collective manner that is due to their coupling in the ordered phase. The quanta of these collective excitations are referred to as magnons. Analogous to the case of collective nuclear excitations (phonons), a double differential cross section can be derived describing the scattering of neutrons from magnons [14]. On the other hand, at temperatures above the critical temperature T_c, thermal energy causes magnetic fluctuations as well. Neutron scattering from these 'critical' fluctuations is regarded in the following.

Critical scattering

The generalized susceptibility $\chi(\mathbf{Q},\omega)$ consists of a real and imaginary part:

$$\chi(\mathbf{Q},\omega) = \chi'(\mathbf{Q},\omega)' + i\chi''(\mathbf{Q},\omega)\,, \tag{1.39}$$

where the imaginary part χ'' can be measured with neutron scattering. The Kramers-Kronig relation provides a connection between χ' and χ'':

$$\chi'(\mathbf{Q},\omega) = \frac{1}{\pi}\int_{-\infty}^{\infty} d\omega' \frac{\chi''(\mathbf{Q},\omega')}{\omega-\omega'}\,, \tag{1.40}$$

which in turn allows a comparison of neutron results with bulk measurements: $\chi'(\mathbf{Q},0)$ denotes the static susceptibility which in the limit $\mathbf{Q}\rightarrow\mathbf{0}$ becomes the bulk susceptibility $\chi_b := \chi'(\mathbf{0},0)$ such as measured with a dc-magnetometer. It can be shown that Eqs. (1.39) and (1.40) hold if

$$\chi''(\mathbf{Q},\omega) = \chi'(\mathbf{Q},0)\omega F(\mathbf{Q},\omega)\,, \tag{1.41}$$

with the general spectral weight function $F(\mathbf{Q},\omega)$ being an even function of ω and satisfying

$$\int_{-\infty}^{\infty} F(\mathbf{Q},\omega)d\omega = 1\,. \tag{1.42}$$

In case of critical scattering at small $\mathbf{q}$, where

$$\mathbf{q} = \mathbf{Q} - \mathbf{G}_m \quad \text{and} \quad q := \frac{\mathbf{q}}{||\mathbf{q}||}\,, \tag{1.43}$$

mean-field theory yields the q-dependent static susceptibility

$$\chi'(\mathbf{Q},0) = \frac{c_0}{\kappa(T)^2+q^2}\,, \tag{1.44}$$

with

$$\kappa(T)^2 = \kappa_0^2(T-T_c) \tag{1.45}$$

and respective constants c_0 and κ_0. Concerning the spectral weight function $F(\mathbf{Q},\omega)$, it turns out that a Lorentzian with a $\mathbf{q}$-dependent linewidth $\Gamma(\mathbf{q})$ models the physics appropriately:

$$F(\mathbf{Q},\omega) = \frac{1}{\pi}\frac{\frac{\Gamma(\mathbf{q})}{2}}{\omega^2 + \left(\frac{\Gamma(\mathbf{q})}{2}\right)^2} . \tag{1.46}$$

Inserting Eqs. (1.46) and (1.44) in Eq. (1.41) and noting the fluctuation-dissipation theorem (Eq. (1.24)), the scattering function finally reads:

$$S(\mathbf{Q},\omega) \propto \frac{1}{\pi} \cdot \underbrace{\frac{\omega}{1 - e^{\frac{-\hbar\omega}{k_\mathrm{B}T}}}}_{(*)} \cdot \frac{c_0}{\kappa(T)^2 + q^2} \cdot \frac{\frac{\Gamma(\mathbf{q})}{2}}{\omega^2 + \left(\frac{\Gamma(\mathbf{q})}{2}\right)^2} . \tag{1.47}$$

At the limits of low or high energies, the factor $(*)$ reveals the following behavior:

$$(*) = \frac{\omega}{1 - e^{\frac{-\hbar\omega}{k_\mathrm{B}T}}} \rightarrow \begin{cases} k_\mathrm{B}T & \text{for } k_\mathrm{B}T \gg \hbar\omega \\ \omega & \text{for } k_\mathrm{B}T \ll \hbar\omega \end{cases} . \tag{1.48}$$

Thus, energy scans ($\mathbf{q} = const.$) just above T_c covering a very narrow range around zero (i.e., $k_\mathrm{B}T \gg \hbar\omega$) exhibit a truly Lorentzian line shape. On the other hand, when scanning a wider range in energy the factor $(*)$ becomes ω-dependent and changes the Lorentzian line shape. Finally, for $k_\mathrm{B}T \ll \hbar\omega$, the Lorentzian is multiplied with a simple factor ω that causes the maximum in intensity to shift to $\omega_{max} = \Gamma/2$.

1.3 Resolution effects and special elements of a TAS

So far, only the *intrinsic signal* from different systems has been taken into account, neglecting experimental resolution effects. These are briefly described in this section.

In a real neutron scattering experiment, the intrinsic signal $S(\mathbf{Q},\omega)$ has to be convoluted with the resolution function of the instrument $R(\mathbf{Q}-\mathbf{Q}_0, \omega-\omega_0)$ to describe the measured neutron intensity $I(\mathbf{Q}_0,\omega_0)$:

$$I(\mathbf{Q}_0,\omega_0) = \int d\omega d\mathbf{Q}\; R(\mathbf{Q}-\mathbf{Q}_0, \omega-\omega_0) \cdot S(\mathbf{Q},\omega) . \tag{1.49}$$

The measured intensity in turn is defined as the flux Φ_D reaching the detector normalized to the flux Φ_M measured by the monitor that is placed directly in front of the sample:

$$I(\mathbf{Q}_0,\omega_0) = \frac{\Phi_\mathrm{D}(\mathbf{Q}_0,\omega_0)}{\Phi_\mathrm{M}(\mathbf{Q}_0,\omega_0)} . \tag{1.50}$$

Usually, the detector signal is accumulated until a fixed number of monitor counts is detected. Note that the resolution function depends exclusively on the configuration of the spectrometer and the mosaic spread of the sample. It is peaked at $\mathbf{Q}_0, \omega_0$ and decreases for deviations from these values such that contours of constant amplitude describe a 4D ellipsoid in $(\mathbf{Q}, \omega)$ space. However, for a given spectrometer configuration, the volume, shape and orientation of that ellipsoid can change with $\mathbf{Q}$ and ω.

In order to obtain higher neutron intensity, the monochromator and analyzer usually consist of several small single crystals with sufficiently broad mosaic spread[3], which are mounted with adjustable curvature to focus the beam horizontally and vertically. Resulting finite beam divergences in turn can be controlled by appropriate collimation: Soller collimators consist of parallel steel blades coated with a material that absorbs neutrons (e.g., cadmium). The spacing of the blades and their length sets the maximal divergence of the neutrons passing through. Typically, up to four collimators are used to control horizontal (in plane) beam divergence, that is to say in front of and behind both the monochromator and analyzer crystal. For the benefit of beam intensity, one usually refrains from vertical (out of plane) collimation. Assuming that collimator transmission functions and mosaic distributions are Gaussian, the resolution function can be modeled with a Gaussian, too:

$$R(\mathbf{Q}-\mathbf{Q}_0, \omega-\omega_0; \mathbf{G}) = R_0 \, e^{-\frac{1}{2}(\mathbf{Q}-\mathbf{Q}_0,\omega-\omega_0)^{\mathrm{T}} \, \mathbf{G} \, (\mathbf{Q}-\mathbf{Q}_0,\omega-\omega_0)} \,, \tag{1.51}$$

where R_0 and the 4×4 matrix $\mathbf{G}$ are functions of $\mathbf{Q}_0$ and ω_0. Generally, $\mathbf{G}$ contains off-diagonal elements, and hence the principal axes of the resolution ellipsoid do not coincide with the axes defined by $\mathbf{Q}$ and ω. On the other hand, assuming that the in plane collimation in sufficiently small, the vertical direction is uncoupled from the other three coordinates. Collimation predominantly affects the FWHM of the resolution ellipsoid in $\mathbf{Q}$ space, whereas its energy width can be controlled with the appropriate choice of the incident neutron energy. A proper description of how the resolution ellipsoid can be calculated from a given spectrometer configuration is beyond the scope of this work. The basic relation of the incident energy with the experimental energy resolution is explained in the following. For the general case of Bragg scattering from a crystal, the Bragg condition yields the absolute energy resolution ΔE:

$$\Delta E \propto E \cot\theta \,, \quad \text{with} \quad 0 < \theta < \frac{\pi}{2} \,. \tag{1.52}$$

Neutrons are Bragg scattered twice at the monochromator and analyzer crystal, respectively. To minimize the energy width ΔE it is thus advantageous to choose lower energies (i.e., longer wavelengths λ) that are Bragg reflected at higher angles θ. Even

[3]Crystals with perfect lattice would produce infinitely sharp Bragg peaks. Since spectrometers can never be perfectly aligned, a finite width of Bragg peaks is necessary to obtain neutron flux. This finite width is achieved by small imperfections of the crystal lattice.

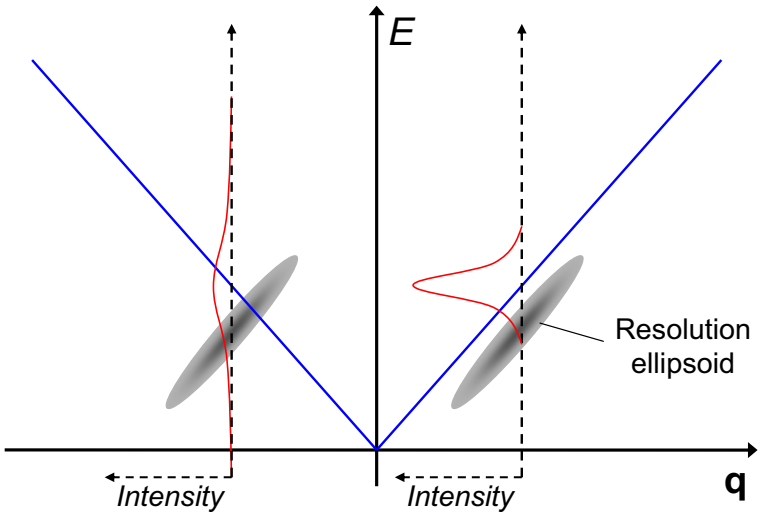

Figure 1.4: Schematic projection of the four-dimensional resolution ellipsoid onto the plane defined by E and $\mathbf{q}$. A linear dispersion relation such as that of acoustic phonons is shown in blue. The peaks shown in red reveal the measured neutron intensity resulting from a scan along E at different $\mathbf{q}$ (dashed coordinate systems). At positive $\mathbf{q}$, the two longer axes of the resolution ellipsoid are parallel to dispersion, and hence a narrow peak will be measured. This scenario corresponds to the 'focused' condition. In the opposite case, at negative $\mathbf{q}$ with the longest axis orthogonal, the peak may be so broad as to be undetectable.

if a certain energy E is needed to perform the experiment, energy resolution can still be improved by maximizing θ by the use of another scattering plane providing smaller inter planar spacing.

Performing an E or $\mathbf{Q}$ scan means sweeping the resolution ellipsoid through the four-dimensional $(\mathbf{Q}, \omega)$ space picking up intensity from structures defined by the scattering function. Thereby, the form of obtained spectra depends very much on the orientation of the resolution ellipsoid relative to these structures. As an example, Fig. 1.4 shows how a longitudinal phonon dispersion is measured in the 'focused' condition.

Special problems

In general, one has to carefully interpret experimental measurements keeping in mind that the non-ideal behavior of the elements of the spectrometer and the sample environment might cause scattering artifacts that can easily be mistaken as intrinsic features. These artifacts are often referred to as 'spurious peaks' or 'spurions'. Their proper identification can be crucial to extract the physically relevant information from the scattering results.

Some spurious effects being directly related to the instrumental resolution are pre-

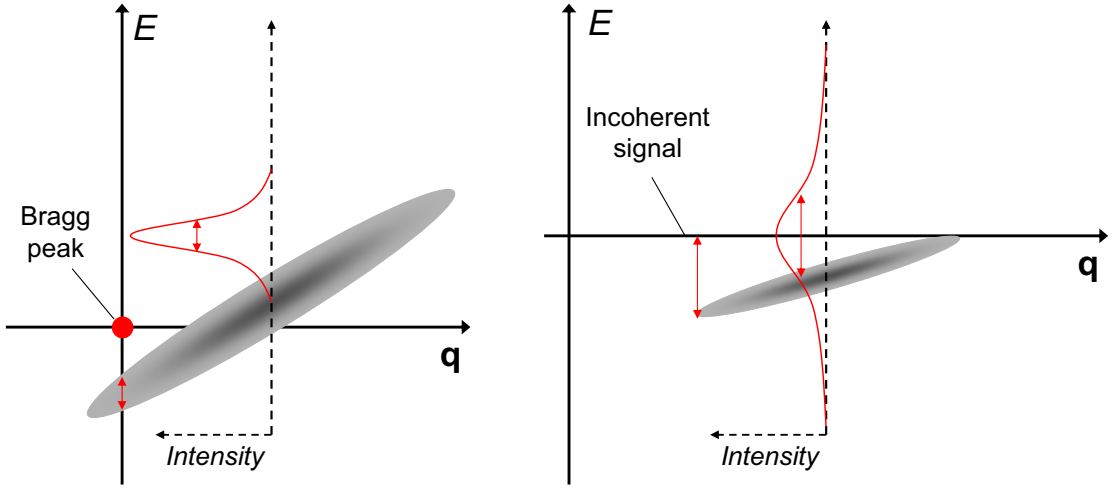

(a) 'Bragg tail' (b) Incoherent scattering

Figure 1.5: Typical resolution effects that can easily be mistaken as originating from intrinsic features. (a) Scanning in close vicinity to a Bragg peak might reveal a sharp peak at finite $\mathbf{q}$ and E such as expected when investigating acoustic phonons. In fact, this peak results from elastic Bragg peak intensity that is picked up with the tail of the resolution ellipsoid. (b) Magnetic critical scattering around $E = 0$ at some magnetic reciprocal lattice vector has to be carefully distinguished from the signal that is due to nuclear incoherent scattering present at all $\mathbf{q}$. The latter is temperature independent as opposed to critical scattering that usually broadens substantially with increasing temperature.

sented in Fig. 1.5, where panel (a) shows how a peak can be easily misinterpreted as resulting from a phonon but in fact is due to elastic Bragg scattering (so-called 'Bragg tail'). Fig. 1.5 (b) reveals the signature of incoherent scattering from the sample that has to be subtracted from the data when investigating features with energy around zero (e.g., magnetic critical scattering).

Furthermore, artifacts that are not related to the experimental resolution can mimic intrinsic effects. As one example, 'accidental Bragg scattering' due to incoherent or diffuse scattering at the monochromator or analyzer crystal is explained in Fig. 1.6. As a second example, higher-order neutrons (harmonics) in the incident beam can give rise to spurious effects. In the Bragg condition (Eq. (1.8)) only first-order neutrons with energy E are considered, whereas for a given angular setting θ_s of the monochromator crystal, higher energy neutrons with energy n^2E and wavelength λ_n are diffracted as well, where

$$\lambda_n = \frac{\lambda_{max}}{n} \quad \text{and} \quad \lambda_{max} = 2d_{hkl}\sin\theta_s \qquad (n \in \mathbb{N})\,. \tag{1.53}$$

Although the flux of higher-order neutrons with $n \geq 2$ is usually much weaker than

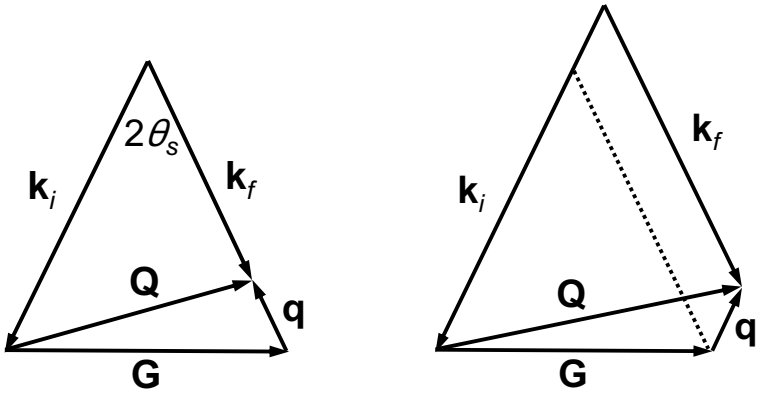

(a) Accidental Bragg scattering from the analyzer.

(b) Accidental Bragg scattering from the monochromator.

Figure 1.6: Schematic diagrams from [13] illustrating two conditions for accidental Bragg scattering. (a) The elastic process corresponding to $\mathbf{Q} = \mathbf{G}$ produces neutrons travelling parallel to $\mathbf{k}_f$ but with magnitude k_i. If there is some incoherent or diffuse scattering at the analyzer, these neutrons will reach the detector in addition to those due to the desired inelastic process where $\mathbf{Q} = \mathbf{G} + \mathbf{q}$. (b) Incoherent scattering at the monochromator provides neutrons travelling parallel to $\mathbf{k}_i$ but with magnitude k_f. Having scattered elastically from the sample, these neutrons travel to the detector with the same $\mathbf{k}_f$ as those participating in the inelastic process.

that of first-order neutrons, they can still mimic weak intrinsic features of the scattering function. In order to suppress such artifacts, several filters can be installed along the neutron beam path depending on the incident neutron energy. In the thermal regime pyrolytic graphite (PG) is by far the most commonly used filter of higher-order neutrons. In most experiments, the final neutron wave vector is fixed and the PG filter is placed between the sample and the analyzer. According to Fig. 1.7, higher order contaminations can be most effectively eliminated when fixing the final energy at 14.7 meV or 30.5 meV (corresponding to $k_f = 2.662\,\text{Å}^{-1}$ or $3.834\,\text{Å}^{-1}$) where the transmission of first-order neutrons is strongly favored. In the cold energy regime, working with fixed k_i is advantageous if extremely high energy resolution is needed. In this case a Beryllium filter cooled to liquid nitrogen (LN_2) temperature ($\sim 77\,\text{K}$) can be installed in the incident neutron beam blocking all neutron with $E > 5.2\,\text{meV}$ (corresponding to $k_i > 1.583\,\text{Å}^{-1}$).

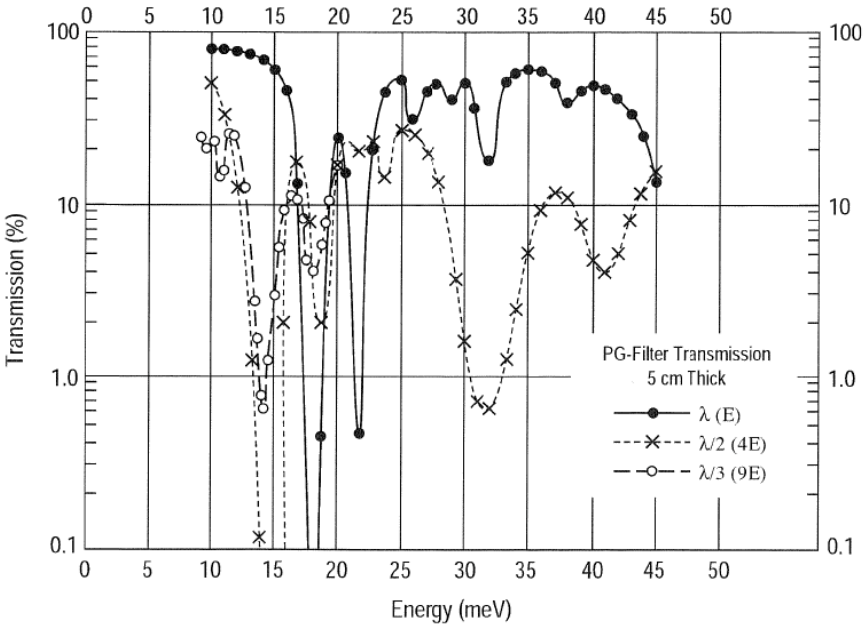

Figure 1.7: Transmission of a 5-cm-thick PG filter vs. energy of higher order harmonics as adopted from [13]. (Note the logarithmic scale of the ordinate.) The crystallographic *c*-axis has to be oriented along the neutron wave vector **k**.

Chapter 2

Spin dynamics in MnSi

2.1 Introduction

MnSi is one of the most extensively studied itinerant-electron magnets. Its crystallizes in the cubic B20 structure that is depicted in Fig. 2.1 (a). Three well-defined energy scales can be distinguished at all temperatures, pressures and magnetic fields at which this system has been investigated [18, 3]:

(1) The strongest energy scale is the tendency to itinerant ferromagnetism that can be described with

$$\mathcal{H}_{\mathrm{FM}} = \sum_{i,j} J_{i,j}\, \mathbf{s}_i \cdot \mathbf{s}_j \,, \tag{2.1}$$

where $J_{i,j}$ is the exchange integral with respect to spins i and j.

(2) As the B20 structure lacks inversion symmetry, weak spin-orbit coupling results in a Dzyaloshinsky-Moriya (DM) interaction

$$\mathcal{H}_{\mathrm{DM}} = \sum_{i,j} \mathbf{D}_{i,j} \cdot (\mathbf{s}_i \times \mathbf{s}_j) \,, \quad \text{with } \mathbf{D}_{i,j} = -\mathbf{D}_{j,i} \,. \tag{2.2}$$

The DM vector $\mathbf{D}_{i,j}$ is determined by bond symmetry and its magnitude by the strength of the spin-orbit coupling which is intermediate between (1) and (3) [19, 20].

(3) The weakest energy scale is provided by the crystal potential.

This hierarchy of energy scales results in a magnetic phase transition at $T_{\mathrm{C}} = 29.5\,\mathrm{K}$ below which magnetic moments of $0.4\,\mu_{\mathrm{B}}$ per formula unit order in a helical arrangement such as shown schematically in Fig. 2.1 (b) [24, 25]. Due to (1) and (2), spins align ferromagnetically in horizontal planes and turn from one plane to the next exhibiting

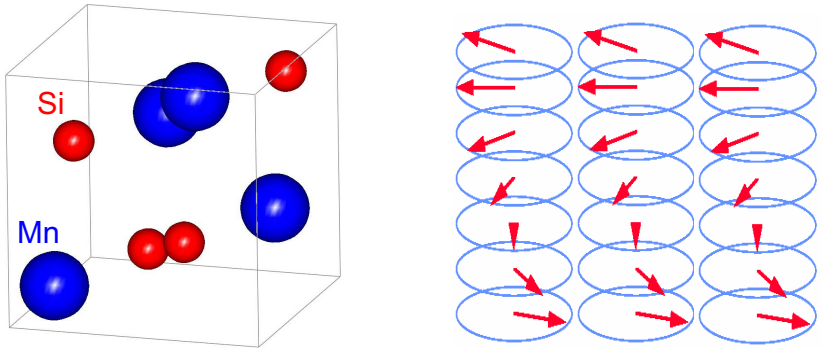

(a) (b)

Figure 2.1: (a) Cubic B20 structure of MnSi with the lattice constant $a = 4.558\,\text{Å}$. The unit cell contains four Mn (blue) and Si (red) atoms, respectively, that are placed at the positions (u, u, u), $(0.5+u, 0.5-u, -u)$, $(0.5-u, -u, 0.5+u)$, $(-u, 0.5+u, 0.5-u)$, with $u_{\text{Mn}} = 0.138$ and $u_{\text{Si}} = 0.845$ [21]. (b) Schematic alignment of magnetic moments as ferromagnetic spiral, from [22].

well-defined chirality given by the sign of $\mathbf{D}_{i,j}$. The relative weakness of the DM interaction results in the long wavelength of the helix of about 180 Å. The crystal potential in turn locks the helical propagation vector $\mathbf{k}_{\text{h}}$ along equivalent $\langle 1\,1\,1\rangle$ directions [24]. A qualitative illustration of the scattering intensity in $\mathbf{Q}$ space characteristic of this magnetic state is given in Fig. 2.2 (a) (left inset), where sharp magnetic Bragg peaks (denoted as black dots) are found in $\langle 1\,1\,1\rangle$ directions on the surface of a tiny sphere the radius of which corresponds to the helix pitch ($q = 0.037\,\text{Å}^{-1}$). Furthermore, hydrostatic pressure p reduces the magnetic transition temperature T_{C}, driving it to zero at $p_c = 14.6\,\text{kbar}$. In close vicinity to that quantum critical point (QCP), so-called 'partial magnetic order' (PO) has been found below a crossover temperature T_0 [3]. PO is characterized by long-range helical correlations but with disordered propagation directions, resulting in scattering intensity on a slightly bigger sphere ($q = 0.043\,\text{Å}^{-1}$) being resolution limited in longitudinal (radial) direction but very broad in transverse (tangential) direction as roughly depicted by the shading in Fig. 2.2 (a) (right inset). Note that the intensity is highest around the $\langle 1\,1\,0\rangle$ directions indicative of a change in the crystal potential now weakly favouring $\langle 1\,1\,0\rangle$. Measurements of the resistivity (Fig. 2.2 (b)) revealed a T^2 dependence below T_{C} as expected from a Fermi liquid (FL). On the other hand, an abrupt change to a $T^{3/2}$ dependence occurs at $p > p_c$ persisting over three decades in temperature [23, 26].

However, the ambient-pressure phase reveals anomalous features as well. The simple band theory was found inappropriate for describing the magnetic properties above the Curie temperature, where the effective magnetic moment of $1.4\,\mu_{\text{B}}$ is much higher than

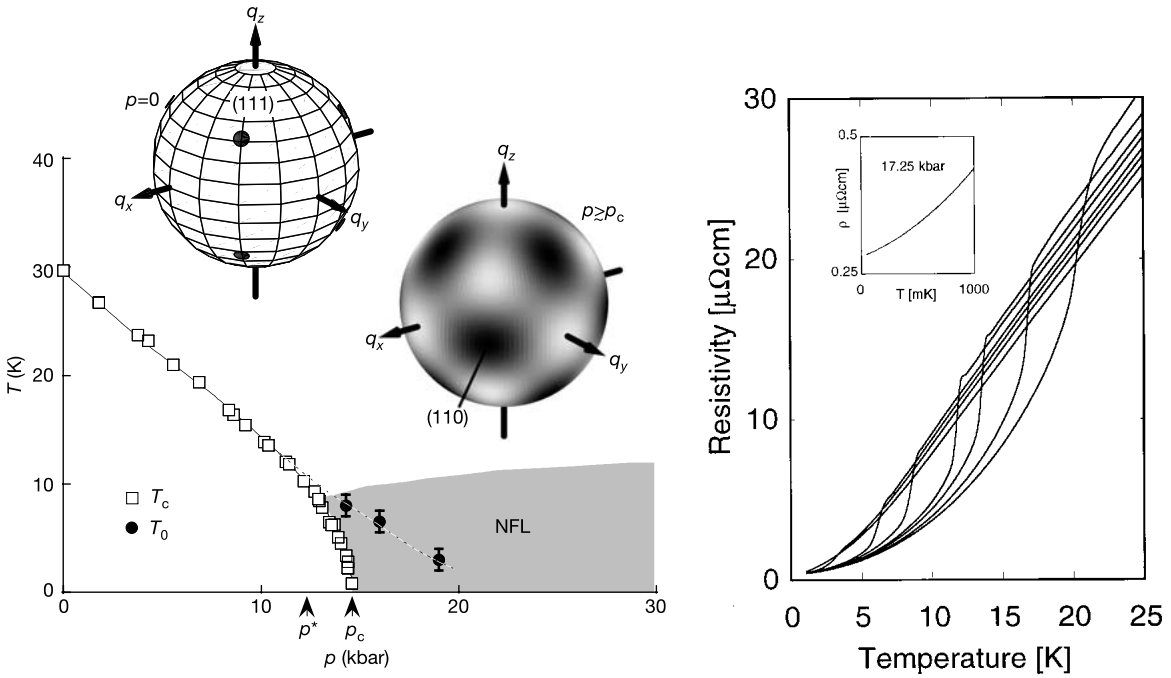

Figure 2.2: Schematic $T - p$ phase diagram of MnSi with qualitative illustration of the scattering intensity characteristic of the magnetic state at $p = 0$ (left inset) and $p \gtrsim p_c$ (right inset) as shown in [3]. The Curie temperature T_C corresponds to shoulders in the resistivity $\rho(T)$ as shown in (b) and decreases linearly up to $p^* = 12\,\text{kbar}$ before it vanishes completely at the critical pressure $p_c = 14.6\,\text{kbar}$. T_0 marks a crossover temperature below which 'partial magnetic order' (right inset) was found, possibly related to an extended non-Fermi-liquid (NFL) phase (shaded). (b) Specific resistivity ρ as function of temperature T at different pressures as depicted in [23] (5.55, 8.35, 10.40, 11.40, 12.90, 13.55, 14.30 and 15.50 kbar going down, starting from the top curve at the right). The shoulder in ρ vs T marks T_C that decreases towards absolute zero at p_c. The inset reveals the NFL-form of $\rho \propto T^{3/2}$ at pressure above p_c. Note that this behavior extends over several orders of magnitude in temperature.

the saturation moment of $0.4\,\mu_B$ at the lowest T [27]. In fact, Ishikawa et al. found in 1982 that the spectrum of spin fluctuations above T_C fits the Moriya-Kawabata (MK) renormalization theory for weak itinerant ferromagnets and hence is responsible for the Curie-Weiss dependence of the static susceptibility [28]. But in contrast to a Heisenberg system where Eq. (1.47) applies with $\Gamma(q) \propto q^2/\chi(q)$, the MK theory yields $\Gamma(q) \propto q/\chi(q)$. Twenty years later, in 2002, experiments with polarized neutrons demonstrated that these paramagnetic fluctuations are chiral and are centered not at the incommensurate positions of the magnetic Bragg peaks in the ordered phase but

on the same sphere in **Q** space as described above [21, 4]. Recently, neutron scattering experiments of Pappas et al. [29] proved that the helical phase undergoes a phase transition to an exotic spin liquid with a substantial chiral component consistent with skyrmion formation [30]. Another puzzling property of MnSi is the mosaic spread of the helical propagation vector (3.35° from [31]) that is orders of magnitude larger than the mosaic of the crystal lattice (0.2°) [32]. In addition, the specific heat [33] and ultrasound attenuation [34] exhibit a two-component lineshape at the Curie temperature T_C that is indicative of the phase transition being weakly first order with a strong second order component. This behavior is in pronounced contrast to conventional theory.

To gain more insight into the origin of these features we investigated the spin dynamics in the paramagnetic phase of MnSi at ambient pressure with neutron scattering experiments of ultra-high resolution. This study is presented in the next section. In order to explain not only our experimental findings but other unusual properties as well, we performed calculations on finite-size spin clusters modeling MnSi. In fact, our results elucidate many anomalous features mentioned above on a qualitative basis, as will be shown in section 2.3.

2.2 Experimental results

We performed our experiment on the cold triple-axis neutron spectrometer 4F operated at the 'Laboratoire Léon Brillouin' of the CEA, Saclay (France). Extremely high wavevector resolution was required to scan at reduced wave vectors as small as $q = 0.037\,\text{Å}^{-1}$ without significant contamination by the nuclear Bragg peak. The 4F spectrometer is the same instrument on which partial order at high pressure was discovered. Without being confined to the small sample space provided by pressure cells we measured two big samples[1] with respective volumes of 1 and $4\,\text{cm}^3$, both nearly perfect single crystals with resolution-limited mosaic spread.

One set of measurements had k_i fixed at $1.15\,\text{Å}^{-1}$ with the collimations of open-20'(between double monochromator)-20'-20', resulting in $30\,\mu$eV energy resolution (high resolution condition). In order to obtain much higher scattering intensity, a second set was taken with $k_i = 1.5\,\text{Å}^{-1}$ and collimation of open-open-40'-20', yielding a relaxed energy resolution of $145\,\mu$eV. A third and fourth set of measurements was performed on a thermal triple-axis neutron spectrometer, 1T again at the Saclay reactor. These scans had k_f fixed at $1.97\,\text{Å}^{-1}$ ($2.662\,\text{Å}^{-1}$) with 25'-20'-20'-20' collimation resulting in an energy resolution of $290\,\mu$eV ($600\,\mu$eV).

All data presented in the following were collected near the (1 1 0) nuclear Bragg peak. The scattering plane was spanned by reciprocal [1 1 0] and [0 0 1] axes. In case

[1]The samples were grown by Th. Wolf (Institut für Festkörperphysik, Karlsruhe Institute of Technology (KIT), Germany).

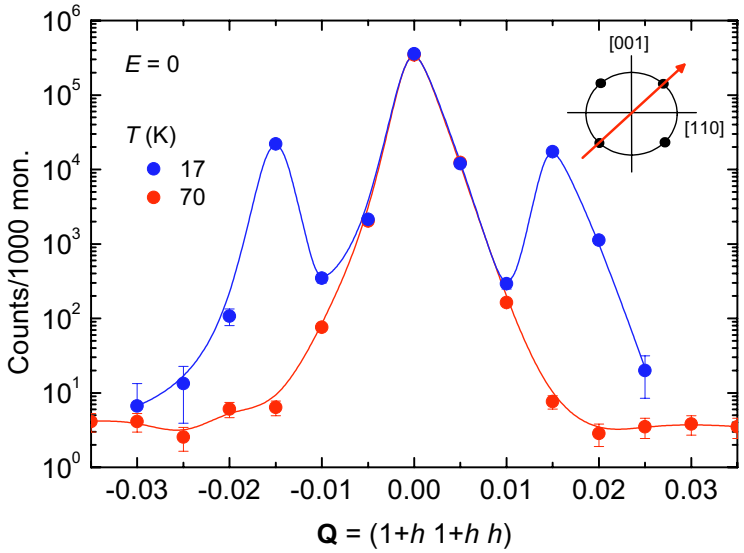

Figure 2.3: Elastic **Q** scans in the [1 1 1] direction. Schematic inset shows the trajectory of the scans in the [1 1 0]/[0 0 1] scattering plane around the nuclear (1 1 0) Bragg peak in the center. Black dots depict the positions of the magnetic Bragg peaks below T_C. Lines are a guide to the eye. At 17 K, i.e., well below $T_C = 29.5$ K, sharp magnetic satellite peaks appear on both sides around the nuclear peak. Their position corresponds to the spiral pitch. The nuclear Bragg peak is temperature independent, thus equally present at 70 K.

of energy scans with fixed k_i, Eq. (4.22) in [13] was taken into account to compensate for the changing resolution volume associated with the analyzer arm. Scans on the thermal TAS were corrected for the $\lambda/2$ contribution at the monitor.

2.2.1 Q scans indicating partial order at ambient pressure

Fig. 2.3 shows scans performed in the [1 1 1] direction at temperatures well below and above $T_C = 29.5$ K. At 70 K, scattering from the nuclear Bragg peak causes huge intensity at (1 1 0). As the nuclear structure of MnSi is temperature independent[2], the nuclear Bragg peak is equally present below T_C but, in addition, the signature of scattering from magnetic order shows up as sharp satellite peaks on both sides around the nuclear peak. Note that magnetic Bragg intensity is about one order of magnitude lower than nuclear Bragg intensity. Previous experiments with small-angle neutron scattering[3] (SANS) [4] revealed that sharp Bragg spots originating from the

[2]Thermal expansion causing Bragg peak positions to shift is taken into account by adjusting lattice parameters at different temperatures, respectively.

[3]Small-angle neutron scattering allows to measure the energy-integrated neutron intensity in close vicinity to the nuclear (0 0 0) Bragg peak (the direct beam).

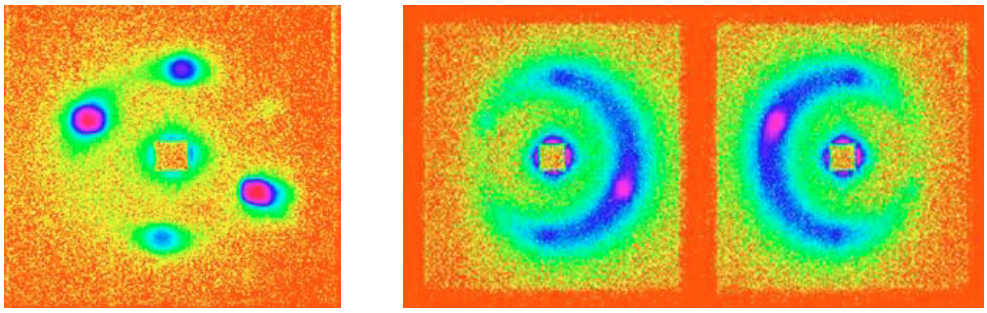

(a) $T < T_C$ (b) $T \gtrsim T_C$

Figure 2.4: Scattering intensity in the reciprocal [1 1 0]/[0 0 1] scattering plane as obtained with SANS using polarized neutrons, from [4]. The direct beam at $\mathbf{Q} = (0\ 0\ 0)$ in the center of the map was masked. (a) Below T_C, scattering from the locked helix results in sharp magnetic Bragg spots corresponding to the periodicity of 180 Å and appearing along $\langle 1\ 1\ 1 \rangle$. Four spots are visible due to their broad magnetic mosaic spread (3.35°). (In the hypothetical case of perfect magnetic mosaic spread, only one spot would be visible.) (b) Only 0.3 K above T_C, diffuse scattering intensity looks like half-moons (left, right with opposite neutron polarization). Their sum would correspond to unpolarized spectra and forms a circle matching the same periodicity. (Weak spots on the half-moons are reminiscent of former Bragg peaks below T_C.)

helical structure below T_C transform into a circle of scattering intensity as the sample is heated above T_C (Fig. 2.4). This circle resembles the signature of partial order such as shown in Fig. 2.2 (a) but with more or less uniform intensity on the surface of the sphere. With our high-resolution TAS, we were able to investigate in detail the temperature dependence of this feature.

Longitudinal scans through the surface of the sphere comparable to those shown in Fig. 2.3 but along [1 1 0] and above T_C are depicted in Fig. 2.5 (a). The inset shows that just above T_C at 30 K, critical scattering appearing as sharp satellite peaks can be clearly distinguished from the nuclear Bragg peak that is about three orders of magnitude higher in intensity. This scan was performed in the high-resolution condition resulting in a small resolution ellipsoid providing very good resolution but low scattering intensity. In order to trace the satellites towards higher temperatures, where we expected a quick broadening, we increased k_i and loosened the collimation to enlarge the resolution ellipsoid picking up more intensity. In fact, the main panel of Fig. 2.5 (a) reveals that upon raising T, the magnetic satellites broaden significantly and move very slightly away from the nuclear Bragg peak. This signature persists to at least 100 K, i.e., about three times T_C.

Fig. 2.5 (b) shows elastic $\mathbf{Q}$ scans in transverse direction along circumference of the satellite ring measured with very small temperature steps. Data obtained above

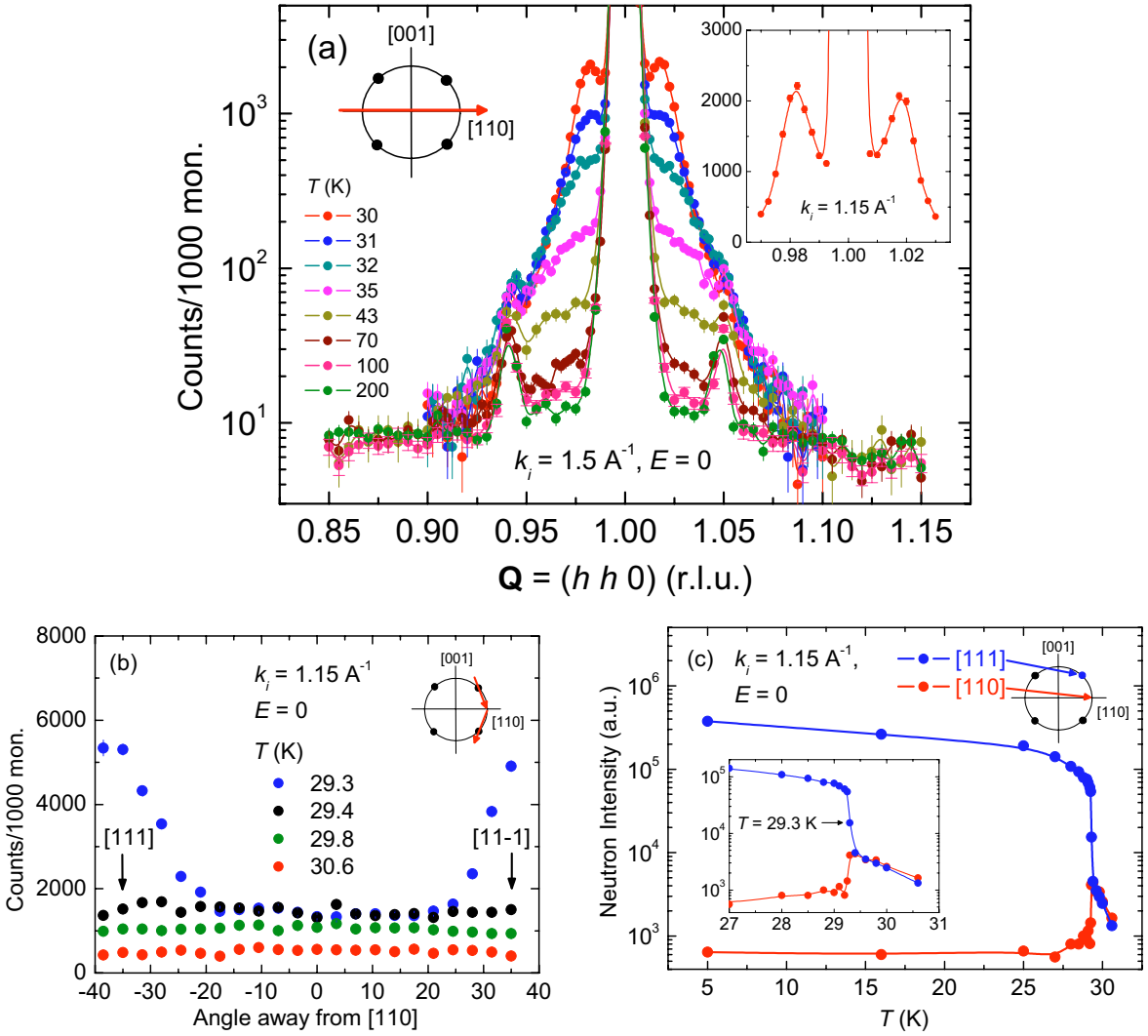

Figure 2.5: (a) Elastic **Q** scans in the longitudinal [1 1 0] direction at $T > T_C$. Lines are guides to the eye. Inset: High-resolution scan ($k_i = 1.15\,\text{Å}^{-1}$) revealing sharp magnetic satellite peaks on both sides around the nuclear (1 1 0) Bragg peak. Their position corresponds to the spiral pitch. Main panel: Relaxed E resolution ($k_i = 1.5\,\text{Å}^{-1}$) allows tracing the satellites towards 200 K over a wider range in **Q**. Note that the small peaks around 0.94 and 1.06 are nuclear artifacts equally present at all T and therefore without influence on the magnetic signal. (b) Elastic **Q** scans in transverse direction on the magnetic sphere covering the range from [1 1 1] to [1 1 −1] measured with high E-resolution. Just below T_C (data shown in blue) magnetic Bragg peaks show up at ⟨1 1 1⟩. (c) Temperature dependence of neutron intensity at [1 1 1] and [1 1 0] positions on the sphere. The inset shows the range around T_C on a larger scale.

T_C show that magnetic intensity is uniformly distributed and there is no trace of the $\langle 1\ 1\ 1\rangle$ peaks that appear below T_C.[4]

These scans reproduce the circle of intensity observed in SANS measurements (compare Fig. 2.4 and [4]) and can be related to the signature of partial order: Although the signal in the longitudinal direction is sharper at high pressure (Fig. 2 (a, c) in [3]) than at ambient pressure, the latter it is still very narrow corresponding to very long correlation lengths. Since thermal fluctuations are much stronger above 29.5 K one might expect an intrinsically broader magnetic signal than below 6 K where the high pressure phase was investigated. On the other hand, transverse scans at ambient pressure reveal no maximum along [1 1 0] that is observed in corresponding scans at high pressure (Fig. 2 (b, d) in [3]). This issue will be addressed in Sec. 2.4 on page 49.

Fig. 2.5 (c) illustrates the abrupt phase transition at T_C, which is well known yet poorly understood. It shows the temperature dependence of respective neutron intensity at [1 1 1] and [1 1 0] positions on the sphere. Cooling down towards T_C induces a gradual increase of intensity which is equally present at both positions. T_C is characterized by an extremely abrupt increase of intensity at the [1 1 1] satellite position: [1 1 1] satellites appear at 29.3 K and reach 25% of their low-temperature intensity at 29.2 K whereas the scattering intensity at [1 1 0] indicating partial order decreases rapidly to a much lower value. This behavior is similar to that reported in [29].

2.2.2 E scans revealing dynamics above T_C

Initially, partial order appeared to be static, i.e., resolution-limited in neutron energy scans with 50 μeV resolution [3], but in fact it is dynamic according to muon spin relaxation (μSR) measurements: Its dynamic character at a timescale of 10^{-10} to 10^{-11} s was revealed in [35]. However, the temperature-dependent energy width of partial order has not been investigated so far. Having found its signature in the $\mathbf{Q}$ scans at ambient pressure as well presented some advantages to actually measure the energy width: Without being confined to the small sample space provided by pressure cells, samples with volumes of 1 and 4 cm^3 could be used, resulting in a much better signal-to-background ratio. A detailed study of the spin dynamics above T_C and at ambient pressure is presented in the following.

Fig. 2.6 shows energy scans through one of the maxima of magnetic intensity obtained in longitudinal scans such as shown in Fig. 2.5 (a). A temperature-dependent spectrum is revealed consisting of up to three components: incoherent nuclear scattering, magnetic scattering of interest in our study and the resolution dependent tail of the (1 1 0) Bragg peak due to imperfect wavevector resolution[5]. Nuclear incoherent

[4] Here, $T_C \approx 29.3$ K deviates about 0.2 degrees from the generally approved value of 29.5 K. This offset in temperature is probably due to a different calibration of the thermometers or a temperature gradient between the sample and temperature sensor in the neutron measurement.

[5] See Fig. 1.5 (a) for explanation.

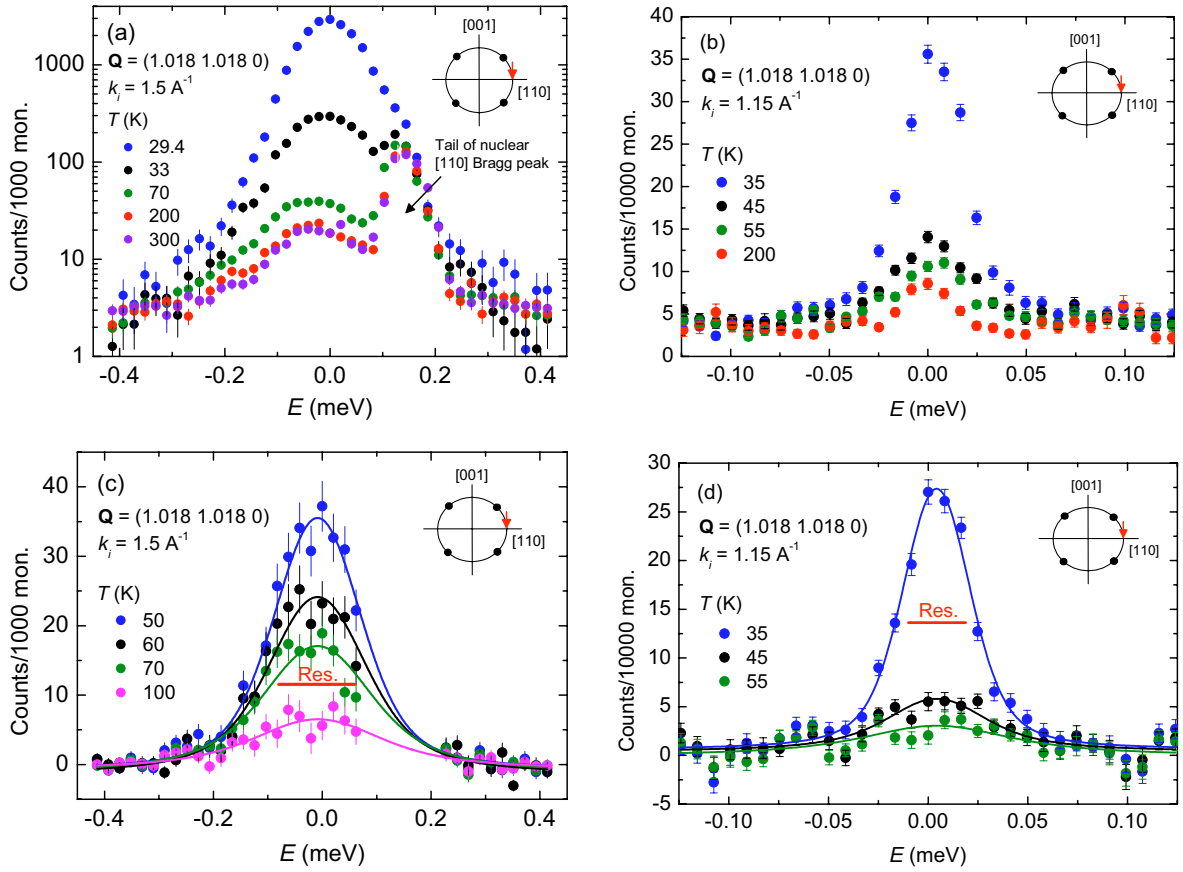

Figure 2.6: Energy scans at $\mathbf{Q} = (1.018\ 1.018\ 0)$, the maximum of the magnetic intensity in Fig. 2.5 (a) above T_C (see red arrow in insets for clarity). (a) Raw data measured with low energy resolution ($k_i = 1.5\,\text{Å}^{-1}$), which include both nuclear and magnetic scattering. The sharp peak near 0.13 meV is the tail of the nuclear Bragg peak and is temperature independent. Since there is no difference between 200 K and 300 K we assume that the magnetic component at 200 K is very small and the scan at 200 K can be used as background. Thus, the magnetic signal at lower temperatures can be obtained by subtracting the 200 K spectra. (b) Raw data measured with high energy resolution ($k_i = 1.15\,\text{Å}^{-1}$). Note that due to the smaller size of the resolution ellipsoid, the contamination by the nuclear Bragg peak vanishes completely. (c, d) Magnetic signal obtained by subtracting 200 K data measured with low (high) energy resolution Γ_{exp} that is shown as red bar, respectively. Note that points contaminated by the Bragg tail are omitted. Solid lines are fits to the data according to Eq. (2.4).

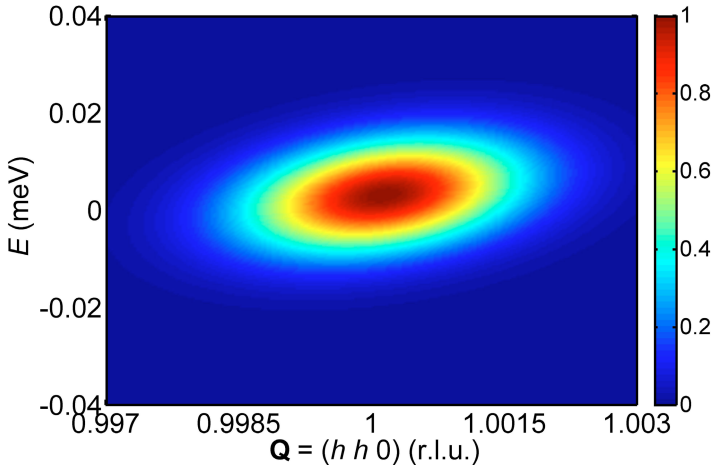

Figure 2.7: 2D cut through the resolution ellipsoid $G(h-h_0, l-l_0, E-E_0; \mathbf{G})$ corresponding to the high resolution condition ($k_i = 1.15\,\text{Å}^{-1}$). Contours of constant amplitude are shown in the plane spanned by $\mathbf{Q} = (h\ h\ 0)$ and E at $l = l_0$.

scattering should be nearly temperature-independent but the magnetic signal is supposed to decrease with increasing temperature as magnetic correlations are suppressed. In fact, the scattering intensity decreases with increasing temperature up to 200 K with no observable change between 200 K and 300 K. Hence, we assign the 200 K and 300 K spectra to nuclear scattering. Subtracting 200 K spectra from the data at lower T, respectively, yields magnetic intensity. It appears as a narrow peak centered at zero energy, which gradually broadens with increasing temperature (Fig. 2.6 (c, d)).

In order to quantitatively extract the temperature dependence of the intrinsic linewidth, spectra are fitted with the convolution of the measured resolution and the appropriate scattering function describing critical scattering according to Eqs. (1.47) and (1.49). Regarding the narrow energy range around zero (i.e., $k_\text{B}T \gg \hbar\omega$), the scattering function $S(E)$ at respective temperature is expected to exhibit a Lorentzian lineshape as described in Sec. 1.2.2.2. As to the determination of the instrumental resolution, it is important to note that data were obtained in close vicinity to the (1 1 0) Bragg peak. Since the resolution ellipsoid does not change significantly between $\mathbf{Q} = (1\ 1\ 0)$ and $\mathbf{Q} = (1.018\ 1.018\ 0)$ (where E scans were performed) we could actually measure it by scanning the Bragg tail (compare Fig. 1.5 (a)) closely around (1 1 0) on a dense grid in the 3D space spanned by the $(h\ h\ 0)/(0\ 0\ l)$ scattering plane and E. Resulting 2530 data points are fitted with a 3D Gaussian $G(h-h_0, l-l_0, E-E_0; \mathbf{G})$[6] which is depicted in Fig. 2.7. After integration in $\mathbf{Q}$ space, the energy-dependent and normalized

[6] $\mathbf{G}$ is 3×3 matrix according to Eq. (1.51).

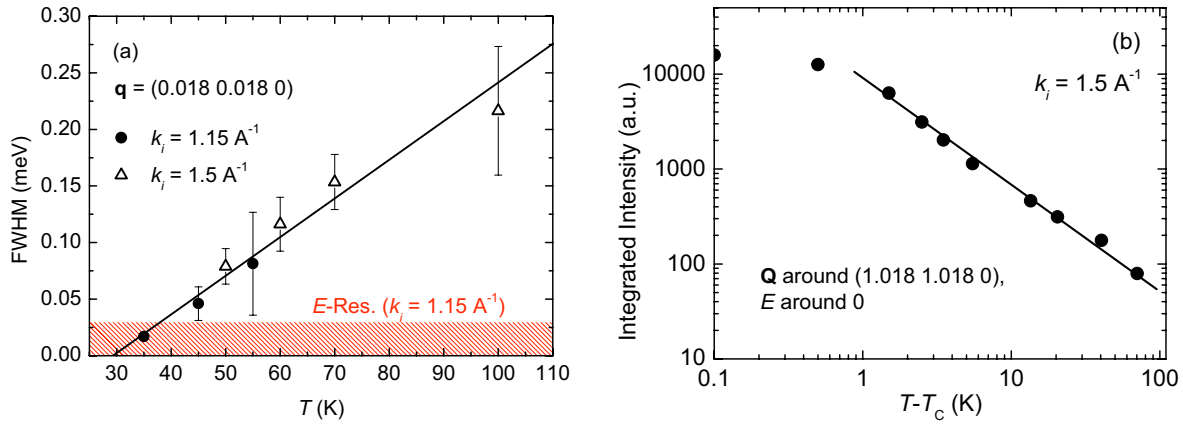

Figure 2.8: (a) Extracted intrinsic linewidth (FWHM) Γ_{int} of the magnetic signal such as shown in Fig. 2.6 (c, d) at different temperatures with a linear fit. (b) Temperature dependence of the integrated intensity of the magnetic signal. The line is a guide to the eye. The integrated intensity was obtained by 'the back of the envelope' method of adding up all the points with nonzero intensity in the background-subtracted E and $\mathbf{Q}$ scans such as shown in Figs. 2.5 (a) and 2.6 (c), and then multiplying respective sums.

Gaussian

$$G_0(E - E_0; \Gamma_{exp}) := \frac{1}{N} \int dh\, dl\; G(h - h_0, l - l_0, E - E_0; \mathbf{G}) \tag{2.3}$$

is convoluted with a Lorentzian $L(E; \Gamma_{int})$ accounting for the *intrinsic* linewidth (FWHM) Γ_{int} to fit the measured intensity $I(E_0)$:

$$I(E_0) \stackrel{!}{=} \int dE\; G_0(E - E_0; \Gamma_{exp}) \cdot L(E; \Gamma_{int})\ . \tag{2.4}$$

Γ_{exp} denotes the instrumental resolution (FWHM) and is shown as red bar in Fig. 2.6.

Finally, the temperature dependence of Γ_{int} is depicted in Fig. 2.8 (a). The high-resolution condition (shown as hatched area) enabled us to observe line widths as small as 17 μeV at 35 K. The low-resolution condition resulted in an order of magnitude higher scattering intensity, which allowed picking up the magnetic signal at temperatures up to 100 K, where the linewidth was larger, but the signal was weak. Aside from much higher sensitivity of the presented measurements, they are entirely consistent with the phenomenology of the high pressure partial order phase: Because of the lower resolution (50 μeV) of the high-pressure experiments, extremely small linewidths close to T_C could not have been detected. At higher T where the magnetic signal becomes significantly

broader, lower intensity and corresponding higher statistical error have hampered a reliable analysis.

Furthermore, the transition from partial order at high pressure to the purely paramagnetic phase is neither second nor first order, but is rather a crossover with the intensity of the partial order decreasing asymptotically to zero upon increasing T. Analogously, the reduction of the magnetic intensity at ambient pressure follows a $1/(T - T_C)$ relation with increasing temperature as depicted in Fig. 2.8 (b). The saturation of the signal one degree above the phase transition to the helically ordered phase is discussed in [29].

The observation of partial order above 14 kbar as well as at ambient pressure indicates that it also should exist at intermediate pressures. In fact, the magnetic signal along [1 1 0] in the unpublished measurements at < 14 kbar [32] performed as a part of the high pressure investigation [3] revealed an energy-resolution-limited signal gradually decaying with increasing temperature. Thus, we have proved that partial order is present not just at pressures above 14.6 kbar, but persists down to ambient pressure where it extends at least up to 100 K.

In order to compare our results with previous measurements at ambient pressure, we reproduced the temperature dependence of the energy linewidth off the magnetic sphere at $\mathbf{Q} = (0.95\ 0.95\ 0)$ as reported in [28]. This study was performed on a thermal TAS. Again, two different resolution conditions (corresponding to $k_f = 2.662\,\text{Å}^{-1}$ and $k_f = 1.97\,\text{Å}^{-1}$) were used to cover the temperature range from 45 K to 200 K. Fig. 2.9 (a, b) shows the magnetic signal obtained after subtraction of a Gaussian fit to the nuclear incoherent background. With the bigger resolution ellipsoid picking up magnetic intensity even at 300 K, the nuclear background could not be measured at $\mathbf{Q} = (0.95\ 0.95\ 0)$ but further away from the partial order sphere at $\mathbf{Q} = (0.6\ 0.6\ 0)$. This is the same position where nuclear incoherent background was determined in [28] and found to be temperature independent. We checked that, indeed, the FWHM of energy scans at $\mathbf{Q} = (0.6\ 0.6\ 0)$ equals the FWHM of energy scans on vanadium measured with the same spectrometer setting. In the following, this linewidth is referred to as the instrumental resolution Γ_{exp}. Measured intensity at E_0 was fitted according to

$$I(E_0) \stackrel{!}{=} \int dE\ G_0(E - E_0; \Gamma_{exp}) \cdot S(E; \Gamma_{int})\ , \tag{2.5}$$

were G_0 is the normalized Gaussian spectrometer resolution and $S(E)$ corresponds to Eq. (1.47). Extracted intrinsic linewidths Γ_{int} at several temperatures are depicted in Fig. 2.9 (c). They are in agreement with previous data. Obviously, at a given temperature above T_C critical fluctuations slow down substantially (i.e., the linewidth decreases) upon approaching the partial order sphere at $\mathbf{q} = (0.018\ 0.018\ 0)$. This behavior is discussed in detail in Sec. 2.4 on page 45.

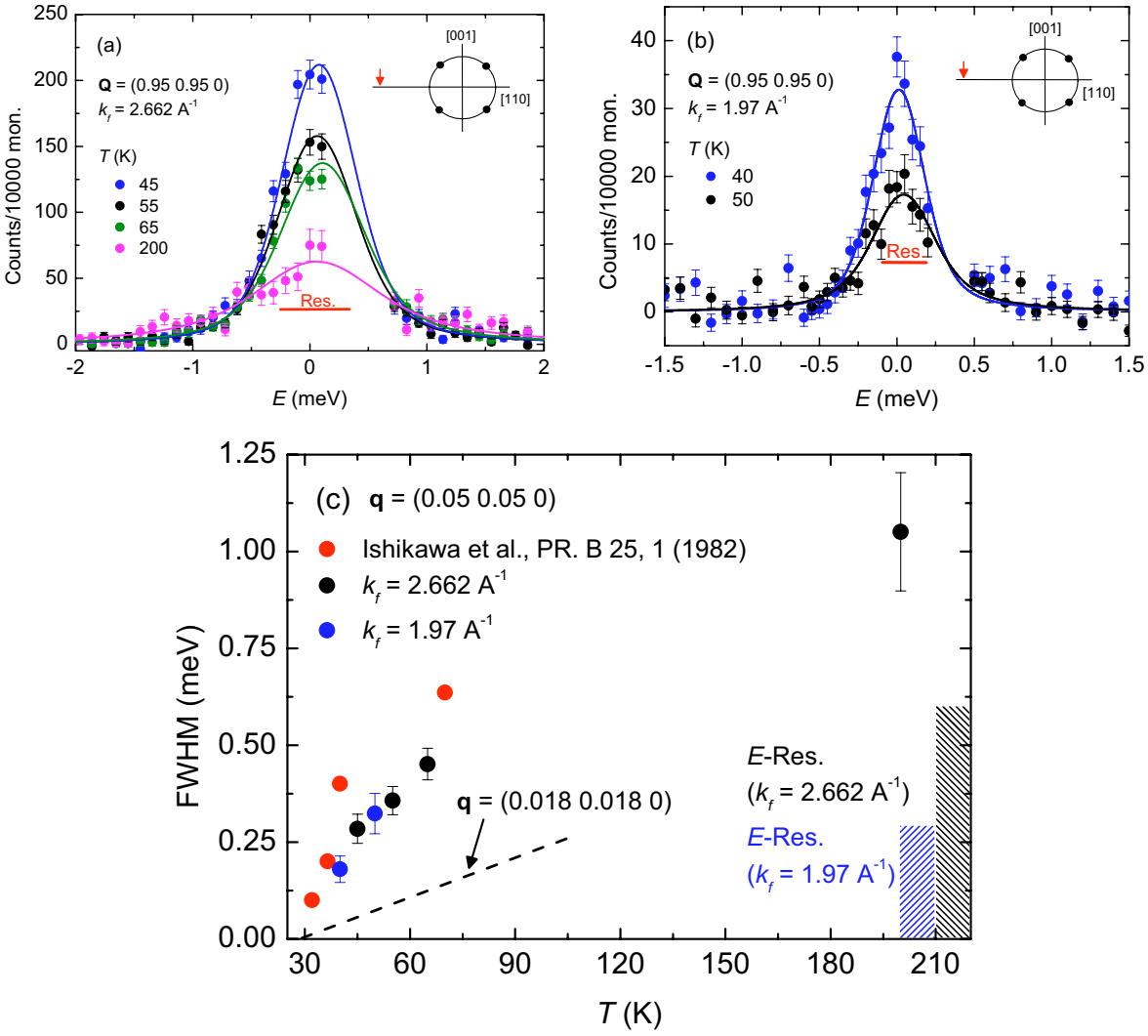

Figure 2.9: Energy scans off the magnetic sphere at $\mathbf{Q}$ = (0.95 0.95 0) (see red arrow in insets for clarity). To obtain reasonable neutron intensity, these scans were performed on a thermal TAS with higher neutron energies (k_f = 2.662 Å^{-1} (a) and k_f = 1.97 Å^{-1} (b)), resulting in a relaxed E-resolution Γ_{exp} (shown as red bar or hatched area, respectively). Solid lines show fits to the data according to Eq. (2.5). Data points affected by the temperature-independent tail of the nuclear Bragg peak are omitted. (c) Extracted intrinsic linewidth Γ_{int} as function of temperature (black, blue) is in qualitative agreement with previous results of Ishikawa et. al. (red). The dashed line depicts the extracted FWHM measured at $\mathbf{Q}$ = (1.018 1.018 0) as shown in Fig. 2.8 (a).

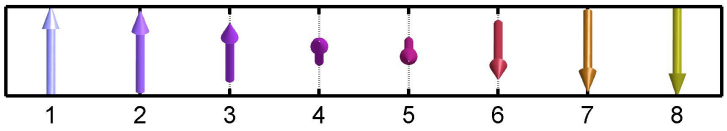

Figure 2.10: Pattern of helical ground state of Eq. 2.6 for spins in a 1D chain. The color code indicates the spin direction: spins pointing into the same direction are colored the same.

2.3 Spin cluster calculations

In order to interpret the unusual properties of MnSi, especially the temperature dependent signature of partial order, we performed calculations on finite-size spin clusters modeling MnSi. We considered the simplest case where each spin interacts with only its nearest neighbors by the ferromagnetic exchange (Eq. (2.1)) and the DM interaction (Eq. (2.2)). Since the crystal potential provides the weakest energy scale, it is initially neglected but later taken into account. The Hamiltonian finally reads:

$$\begin{aligned} \mathcal{H} &= -\frac{1}{2N}\sum_{i=1}^{N}\left(\sum_{j(i)}\left(J\mathbf{s}_i\cdot\mathbf{s}_j+\mathbf{D}_{i,j}\cdot(\mathbf{s}_i\times\mathbf{s}_j)\right)\right), \\ &\text{with } J=1,\ |\mathbf{D}_{i,j}|=D \text{ and } \mathbf{D}_{i,j}=-\mathbf{D}_{j,i}\ . \end{aligned} \tag{2.6}$$

N is the total number of sites and $j(i)$ indexes nearest neighbors of site i. The vector $\mathbf{D}_{i,j}$ points from site i to site j. In our model, Si atoms are henceforth neglected and spins of the same size are placed either on a simple cubic lattice or at Mn sites in the B20 MnSi structure. In both cases, each spin has six nearest neighbors at a distance of 2.796 Å. Orientation optimization was performed for individual spins one-by-one in random order keeping their magnitudes constant. The calculation terminated when the total energy defined by Eq. (2.6) converged. (A more detailed description of the algorithm developed to optimize the spin clusters is given in Appendix A.1.) Limited by the available computer power, the biggest clusters consist of about 9000 sites. In order to ensure that the size of these clusters comfortably exceeds the period of the helix, the relative strength of the two interactions (given by the ratio D/J) was chosen larger than in real MnSi. Thus, all results presented in the following are to be interpreted on a qualitative basis. However, we checked our model for consistency by performing the same calculations with different ratios D/J and obtained the same results.

2.3.1 The triple-helix structure

The ground state of our Hamiltonian (Eq. 2.6) in one dimension (1D) is helical order with the pitch determined by D/J as illustrated in Fig. 2.10. In 3D, helical order

is highly degenerate because the propagation vector $\mathbf{k}_\mathrm{h}$ could point in any direction (remember that the crystal potential lifting the degeneracy by locking the helix along $\langle 1\ 1\ 1\rangle$ is neglected here). Furthermore, magnetic moments along $\mathbf{k}_\mathrm{h}$ have optimized spin orientations with respect to Eq. (2.6), whereas moments in the layers perpendicular to $\mathbf{k}_\mathrm{h}$ align ferromagnetically (see Fig. 2.11 (b)), i.e., their relative orientations are far from optimized. Thus, a helix is an unlikely ground state of Eq. (2.6) in 3D.

In fact, our calculations predict optimized spin arrangements that are distinct from the helix structure and characterized by complex topologies (Fig. 2.11 (c)): In the vicinity of most sites the optimized configuration reveals helical correlations, but with the propagation vector gradually changing its direction. Topological defects appear where different propagation vectors collide. We checked the final structures for a possible dependence on the initial configuration: Regardless of whether optimizations are started with ferromagnetic, helical or random configurations, the final spin arrangements are similar, although not identical. Thus they represent not a unique ground state but local minima whose energies are close to each other for each cluster size and shape but significantly lower relative to ferromagnetic and helical order. The comparison of respective energies turned out to be most significant when normalizing to the number of bonds N_b (i.e., the number of nearest neighbor pairs) according to

$$\mathcal{H} = \underbrace{-\frac{1}{2N_b}\sum_{i=1}^{N}\left(\sum_{j(i)}\left(J\mathbf{s}_i\cdot\mathbf{s}_j+\mathbf{D}_{i,j}\cdot(\mathbf{s}_i\times\mathbf{s}_j)\right)\right)}_{\mathcal{H}_0} - E_\mathrm{1D}(J,D)\ . \tag{2.7}$$

$E_\mathrm{1D}(J,D)$ denotes the (negative) energy calculated via $\mathcal{H}_0$ for a pair of spins (one bond) in a fully optimized and unfrustrated 1D chain as shown in Fig. 2.10. Corresponding cluster size dependent energies for ferromagnetic, helical and optimized structures are depicted in Fig. 2.11 (d). (The energy spread of the majority of the optimized configurations for a given number of sites is of the order of the size of the data points.)

Note that the energy per bond of the ferromagnetic order is independent of the number of sites. In the case of a single cubic unit cell with $N = 4$ sites (smallest N shown) the energy of the helix equals the energy of the ferromagnetic cluster. The reason for this is simply structural: If only a single unit cell is considered, the Mn atom (blue) in the lower left corner of Fig. 2.1 (a) does not have any nearest neighbor. Consequently it does not contribute to the total energy and can never be optimized. (For that reason the corresponding spin is not shown in the real space pictures of any cluster.) The other three Mn atoms are in the same plane perpendicular to [1 1 1] and therefore parallel to each other in the ferromagnetic arrangement as well as in the helical structure. Accordingly, the cross product in Eq. (2.7) cancels resulting in the same energy for both configurations. As the number of sites is increased, E_helix decreases considerably below E_FM but is larger than E_opt for all cluster sizes that we investigated.

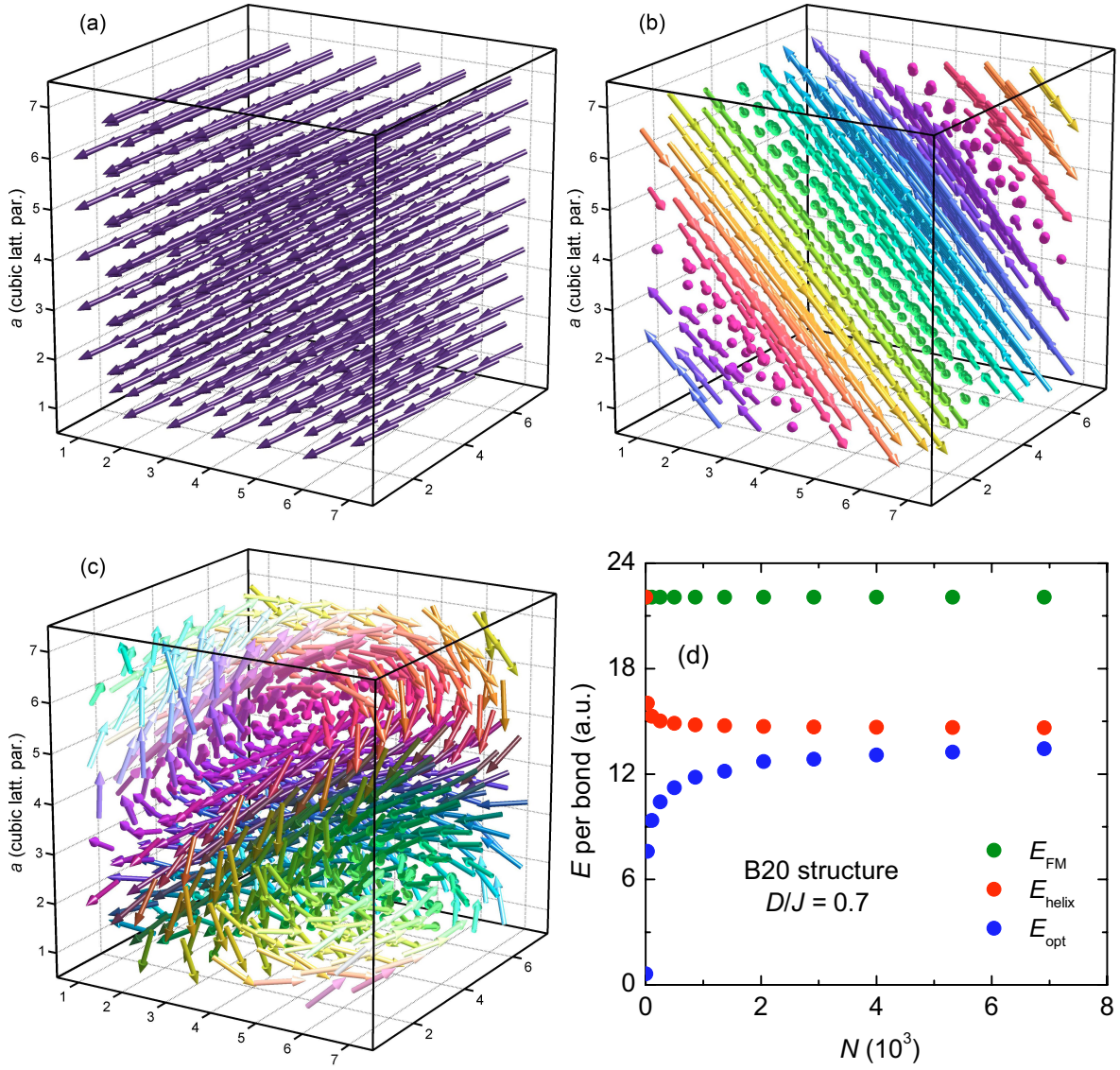

Figure 2.11: Results of model calculations for cubic clusters of spins with nearest neighbors interacting via Eq. (2.6) with $D/J = 0.7$, corresponding to a helix period of about 27.3 Å. The spins are localized at Mn sites in the B20 MnSi structure, neglecting Si atoms. (a, b, c) Real-space pictures of $6 \times 6 \times 6$ cubic unit cells: ferromagnetic order (a), helical order along [1 1 1] (b) and the optimized structure (c). The spin orientation is visualized by a color code, same color indicates parallel moments. (d) Average energies (in arbitrary units) per pair of nearest neighbor spins calculated according to Eq. (2.7) for ferromagnetic order (green), helical order along [1 1 1] (red) and optimized spin configurations (blue) as a function of the number of sites N. (Note that E_{FM} does not depend on the arbitrary direction that the spins point into.)

The smaller the number of sites, the closer does the energy of the optimized structure approach zero but, interestingly, it never actually reaches zero. In line with the above argument, the fact that $E_{\mathrm{opt}}(N = 4) \approx 0.63 > 0$ reveals that only three spins on an equilaterally triangular lattice interacting via Eq. (2.7) are still frustrated: It is not possible to minimize all three pairs of nearest neighbor spins simultaneously.

The biggest clusters that could yet be optimized in a reasonable amount of time (about ten weeks each) are shown in Fig. 2.12 (B20 structure) and Fig. 2.13 (a) (simple cubic structure). Analogous to Fig. 2.11 (d), cluster size dependent energies of respective spin arrangements implemented in the simple cubic lattice are exhibited in Fig. 2.13 (b). As opposed to the B20 structure, the energy per bond of the helix is now independent of the cluster size. Again, the optimized configuration minimizes $\mathcal{H}$ for all N. Since the smallest simple cubic cluster consists of eight spins and is truly 3D, its degree of frustration exceeds the smallest B20 cluster (three interacting spins, effectively 2D) resulting in an energy that is farther from zero.

In order to analyze the pattern of spin arrangements obtained in optimized clusters, a single layer cut from a large cluster is shown in Fig. 2.14 (c). Its structure resembles the packed double helices observed in the blue phases of chiral liquid crystals [36] as well as the skyrmion lattices recently proposed [30] and indeed observed in the so-called 'A-phase' of MnSi appearing in magnetic field [37]. As illustrated in Fig. 2.14 (a), the '*double*-helix' terminology refers to the fact that near the center (singularity), spins rotate along all directions in the plane perpendicular to z, i.e., in particular they rotate along *both* of a pair of orthogonal directions spanning this plane. This is in contrast to the helical structure where spins rotate exclusively along a single direction, the pitch axis, and are uniform along directions perpendicular to the pitch axis. In comparison to double helices, our spin arrangements often have an additional twist away from the singularity. Thus, we propose to call this order a '*triple*-helix', denoting the *three* independent twist directions. It allows to pack 1D singularities propagating in different directions in 3D. Its topology is indicative of the signature of partial order: local helical correlations are expected to produce a sharp neutron scattering signal in longitudinal scans whereas the meandering propagation vectors should make the signal broad in the transverse direction.

Simulation of SANS spectra from the model clusters

To actually relate our triple-helix structures to neutron measurements like the circle of scattering intensity observed with SANS (Fig. 2.4), we calculated the corresponding magnetic neutron intensity following Eq. (1.36). Assuming elastic scattering from only a single state $|\lambda_i\rangle = |\lambda_f\rangle$, this formula can be simplified to

$$\frac{d^2\sigma}{d\Omega_f dE_f} \propto \sum_{\alpha=1}^{3}\sum_{\beta=1}^{3}\left(\delta_{\alpha\beta} - \hat{Q}_\alpha\hat{Q}_\beta\right)\sum_{l=1}^{N}\sum_{l'=1}^{N}\left(e^{i\mathbf{Q}\cdot(\mathbf{r}_l-\mathbf{r}_{l'})}s_{l'}^{\alpha}\cdot s_l^{\beta}\right) , \tag{2.8}$$

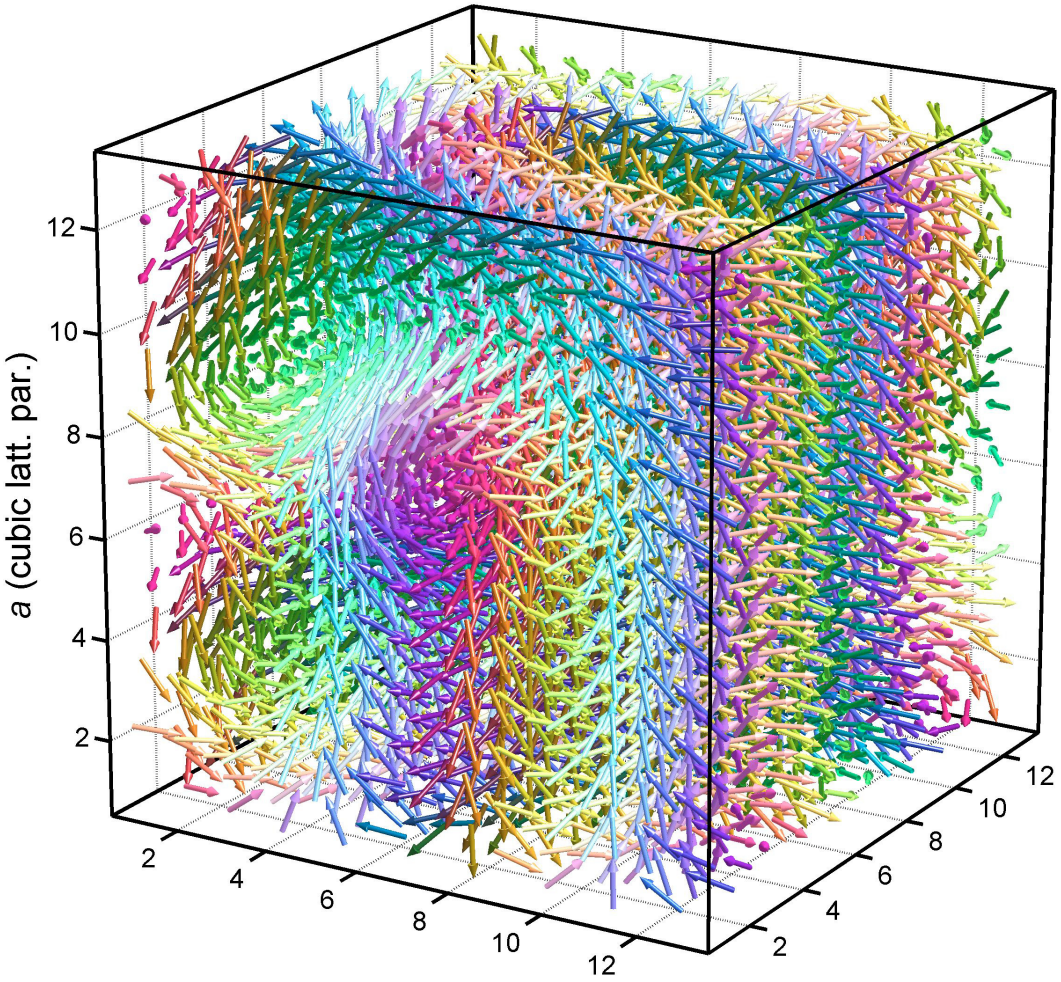

Figure 2.12: Real space pictures of biggest optimized cluster in the B20 structure with $D/J = 0.7$ (helix period $\sim 27.3\,\text{Å}$) consisting of $12 \times 12 \times 12$ cubic unit cells corresponding to about 7000 sites.

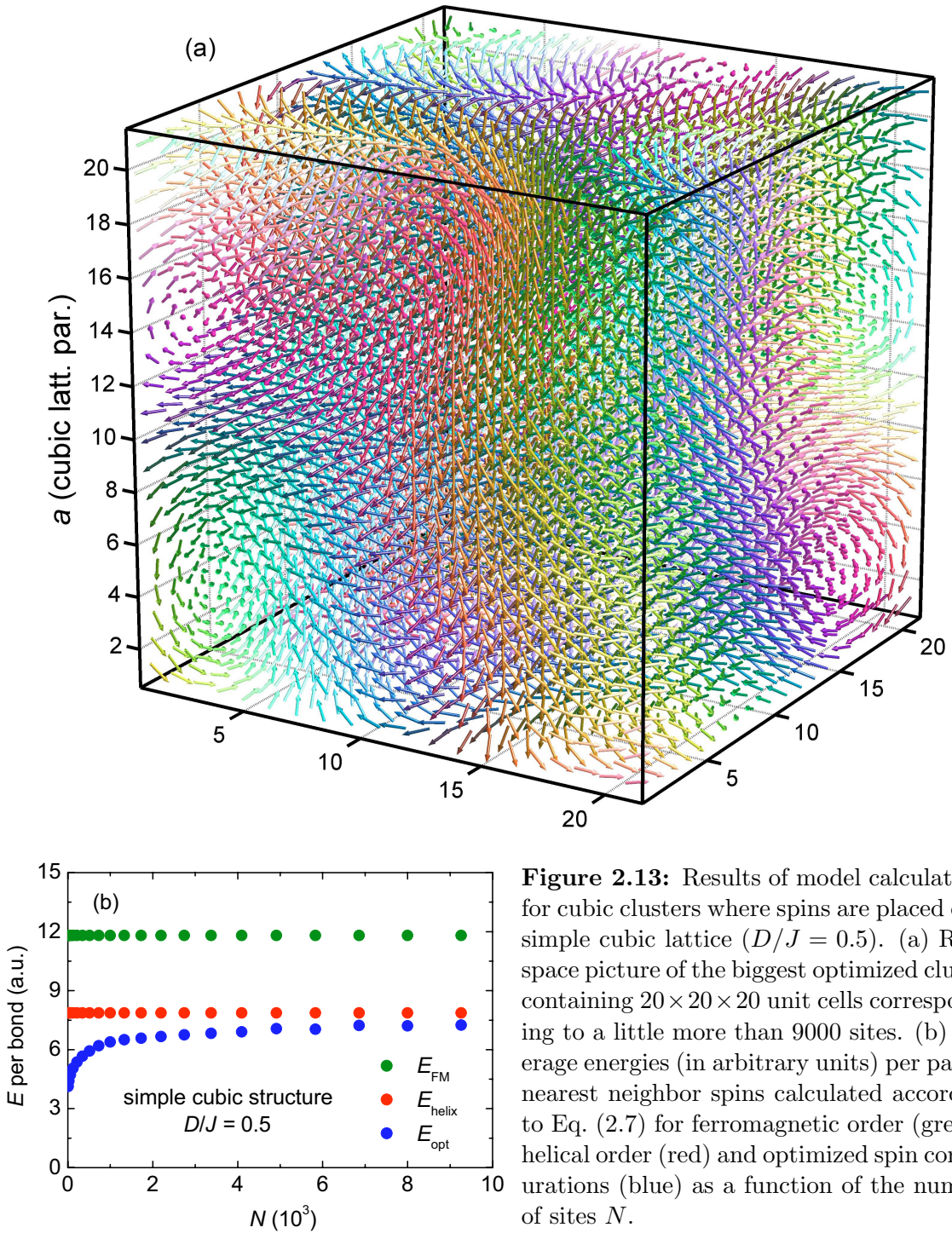

Figure 2.13: Results of model calculations for cubic clusters where spins are placed on a simple cubic lattice ($D/J = 0.5$). (a) Real-space picture of the biggest optimized cluster containing $20 \times 20 \times 20$ unit cells corresponding to a little more than 9000 sites. (b) Average energies (in arbitrary units) per pair of nearest neighbor spins calculated according to Eq. (2.7) for ferromagnetic order (green), helical order (red) and optimized spin configurations (blue) as a function of the number of sites N.

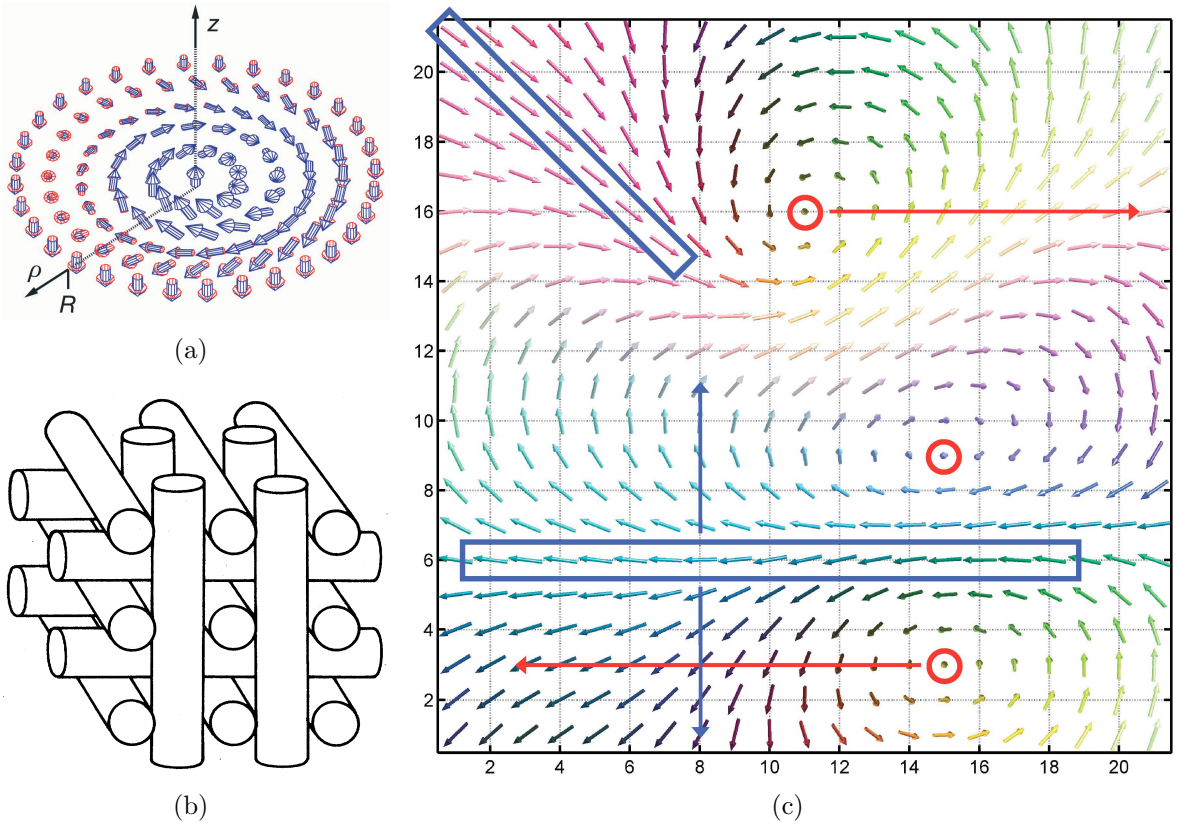

Figure 2.14: (a) 2D structure of the double-helix as illustrated in [30]. The helical spin modulation has propagation axes in all directions ρ in the plane perpendicular to z and is centered around a singularity (spin pointing along z in the middle). A double-helix can be uniformly extended in z direction forming a cylinder with a line singularity in its center (along z) and perfect double-twisting in all planes perpendicular to z. To fill 3D space, these 'double-twist cylinders' can be packed. In so-called blue phases I and II [36], the packing reveals an ordered structure that is related to the symmetry of the crystal to minimize the energy of domain boundaries (e.g., in the O^2 symmetry as shown in (b), picture is adopted from [36]). The blue phase III in turn is indicative of double-twist cylinders arranged in a disordered fashion [36]. (c) 2D layer cut from the simple cubic cluster shown in Fig. 2.13 (a) (layer no. 11 in vertical direction). Red circles mark line singularities propagating in out-of-plane direction with double-helix-like arrangements in the plane. Blue rectangles highlight line singularities running in-plane. Since these 1D singularities propagate into different directions, the optimized structure is most similar to blue phase III. Furthermore, in comparison to the double helix, our spin arrangements are often characterized by an additional twist away from the singularity around the third direction defined by the line singularity itself (along arrows).

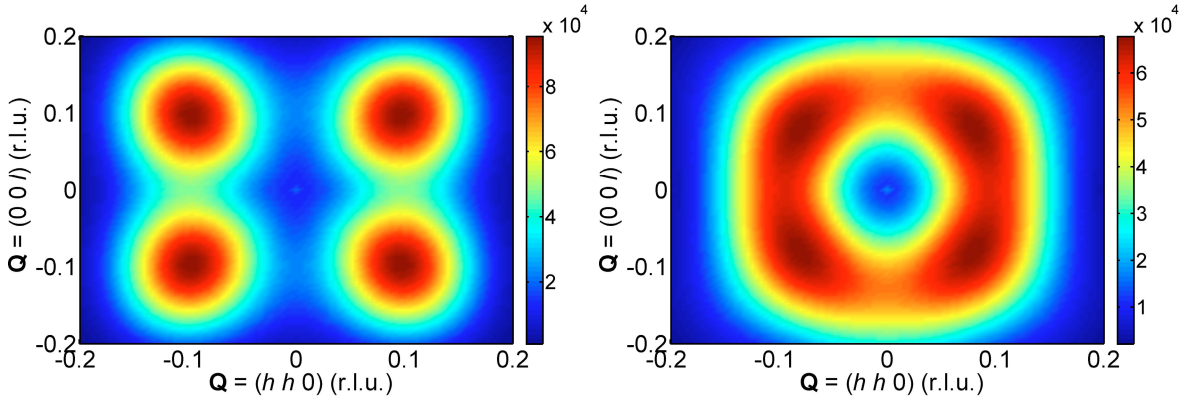

Figure 2.15: Simulation of SANS spectra from model clusters in the MnSi B20 structure with $D/J = 0.7$: Calculated neutron intensity in plane that is spanned by reciprocal [1 1 0]/[0 0 1] axes around (0 0 0). (Left panel) Helix along cubic $\langle 1\ 1\ 1\rangle$ directions (topology of low-T phase) such as shown in Fig. 2.11 (b). (Right panel) Triple-helix structure corresponding to Fig. 2.11 (c).

where α and β label x, y, z components of the normalized transfer of momentum $\hat{\mathbf{Q}}$ and of the spin $\mathbf{s}$ at sites l and l'. Basically, this formula corresponds to the Fourier transform (FT) of a spin arrangement in real space into reciprocal space. To mimic scattering from an infinite number of clusters, with a distribution of sizes, we summed the signal of several clusters of different sizes[7] in all $\langle 1\ 1\ 0\rangle/\langle 0\ 0\ 1\rangle$ scattering planes around (0 0 0) and averaged crystallographic equivalent $\mathbf{Q}$ points. The resulting intensity distributions for clusters consisting of around $6 \times 6 \times 6$ unit cells are depicted in Fig. 2.15. Our calculations are in perfect qualitative agreement with SANS (compare Fig. 2.4): The triple-helix structure produces the circle of magnetic intensity (right panel) that is observed just above T_C. The same calculation performed on the locked-helix structure of the low temperature phase results in sharp spots of high scattering intensity appearing in all $\langle 1\ 1\ 1\rangle$ directions (left panel).

2.3.2 Qualitative energy considerations

In addition to the two energy scales given by J and D in Eq. (2.7), the crystal anisotropy is the third (weakest) energy scale that is taken into account in the following discussion. If it is moderately large, then helical order with the wavevector aligned along the favored

[7] In the case of clusters with sizes 'around' $n \times n \times n$ B20 unit cells, 10 clusters are calculated in addition to $n \times n \times n$ with the following distribution of sizes (two clusters per size, optimized after initialization with different random configuration): $(n-1)\times(n-1)\times n$, $(n-1)\times n\times n$, $(n+1)\times n\times n$, $(n+1)\times(n+1)\times n$ and $(n-1)\times n\times(n+1)$.

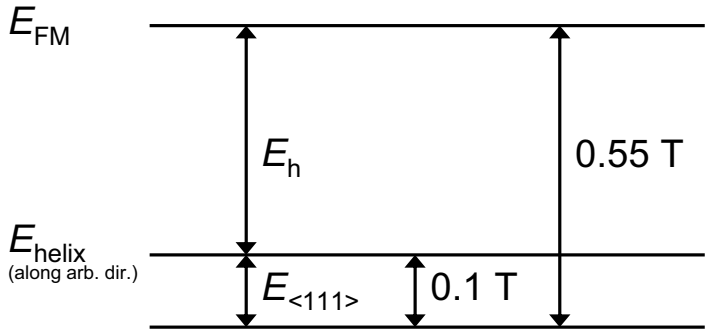

Figure 2.16: Energy scales related to magnetic field values as applied in SANS experiments [38] to MnSi well below T_C where the helix locked along $\langle 1\ 1\ 1\rangle$ is the ground state (lowest energy level in the plot). As described in the main text, a field of 0.1 T is sufficient to overcome the crystal potential (i.e., $E_{\langle 111\rangle}$) and align the helix along the arbitrary field direction **B**. Ferromagnetic alignment of the spins along **B** is achieved for a much higher field of 0.55 T. Thus, $E_{\langle 111\rangle} = 0.1/0.55 \cdot (E_h + E_{\langle 111\rangle})$, i.e., $E_{\langle 111\rangle} \approx 0.22 \cdot E_h$.

$\langle 1\ 1\ 1\rangle$ directions will always have a lower energy than the triple-helices, which lack a well defined direction of the propagation vector. On the other hand, in case of a weak crystal potential, a competition between the helical and the triple-helix-based phase with a transition possible between the two can be discussed on a qualitative basis within the framework of our spin clusters.

We define $E_{\langle 111\rangle}$ as the energy gained by aligning the helices along $\langle 1\ 1\ 1\rangle$ with respect to an arbitrary orientation of helical propagation directions ('unlocked helical order' with energy E_{helix}). Furthermore, E_h denotes the difference between E_{FM} (corresponding to ferromagnetic order) and E_{helix}. Regarding the Hamiltonian given in Eq. (2.7), E_{helix}, E_{FM} and E_h can be expressed in terms of D and J as is derived analytically in Appendix A.2.

More importantly, one can relate the relative strength of respective energy scales to the crystal potential by looking at previous SANS experiments in magnetic field **B** [38]. At ambient pressure and below T_C a small magnetic field of 0.1 T is sufficient to unpin the helical propagation vector from $\langle 1\ 1\ 1\rangle$ and align it along **B**. In addition, a small net ferromagnetic moment is induced in the helix resulting in the so-called 'conical' phase [39]. A much larger field of 0.55 T is necessary to also overcome D and completely (ferromagnetically) align the moments parallel to the field [38]. Based on these field values, an order-of-magnitude estimate (Fig. 2.16) yields

$$E_{\langle 111\rangle} \approx 0.22 \cdot E_h\ . \tag{2.9}$$

Now, let E_{th} denote the energy gained by forming the triple-helix clusters from the uniform helix as illustrated in the inset of Fig. 2.17. (Note that in this Figure, results

of calculations with $D/J = 0.35$ producing a helix period of about 52.1 Å, closer to real MnSi are shown.) Corresponding to Figs. 2.11 (d) and 2.17, respective largest clusters consisting of $N \sim 7000$ sites reveal

$$E_{\mathrm{th}} = x \cdot E_{\mathrm{h}} \,, \tag{2.10}$$

where $x = 0.16$ ($x = 0.33$) for $D/J = 0.7$ ($D/J = 0.35$). The comparison of Eqs. (2.9) and (2.10) indicates that in our model, E_{th} at largest N and $E_{\langle 111\rangle}$ can be considered the same order of magnitude.[8] Consequently, transitions between competing locked helical order and the triple-helix phase may indeed be induced by small changes of external parameters, notably temperature, hydrostatic pressure, and doping, as will be discussed below.

We now discuss qualitatively the effect of the temperature that is not explicitly considered in our model but governs the stability of triple-helix clusters vs. helical order. The cluster size N in our calculations naturally corresponds to the maximal size of correlated magnetic domains and, therefore, is related to the temperature via the temperature dependence of the correlation length ξ. This relationship between N and T provides the basis for the following discussion: Decreasing N, i.e., decreasing the correlation length can be interpreted as increasing the temperature in our model clusters. (Indeed, the average domain size decreases on heating both below and above T_{C}, reaching about half the helix period right below T_{C} at ambient pressure [29].)

$|E_{\mathrm{th}}|$ is a measure of the stability of the triple-helix phase against forming the low-T helix. It decreases significantly with the increasing cluster size as depicted in the main frame of Fig. 2.17. Correspondingly, the triple-helix structure becomes less favorable towards lower temperature. The temperature independent crystal potential is arbitrarily taken into account by the dashed line denoting $E_{\langle 111\rangle}$. Upon lowering the cluster size, the impact of the crystal potential weakens relative to $|E_{\mathrm{th}}|$ which results in a competition of the two ground states around the cluster size $N = N_c$ where $E_{\langle 111\rangle} = E_{\mathrm{th}}(N_c)$. This cluster size (and related correlation length) can be associated with T_{C}: Above T_{C}, i.e., below the corresponding correlation length, the triple-helix structure is the ground state whereas below T_{C}, the helical phase pinned by the crystal potential becomes more favorable. The transition should be of first order because the triple-helix arrangement is topologically distinct from the helical structure, meaning that both states are separated by a potential well which has to be overcome by the energy of thermal fluctuations at T_{C} and impedes a continuous crossover.

[8] For a smaller ratio D/J that would produce the 'real' helix period of 180 Å, a bigger cluster consisting of N_0 sites could be found where again $E_{\mathrm{th}}(N_0) \approx 0.22 \cdot E_{\mathrm{h}}(N_0)$. Due to the limited computing power, corresponding calculations were not possible. Our model is thus to be interpreted on a qualitative basis, where $E_{\mathrm{th}} \approx E_{\langle 111\rangle}$ holds at some smaller cluster size.

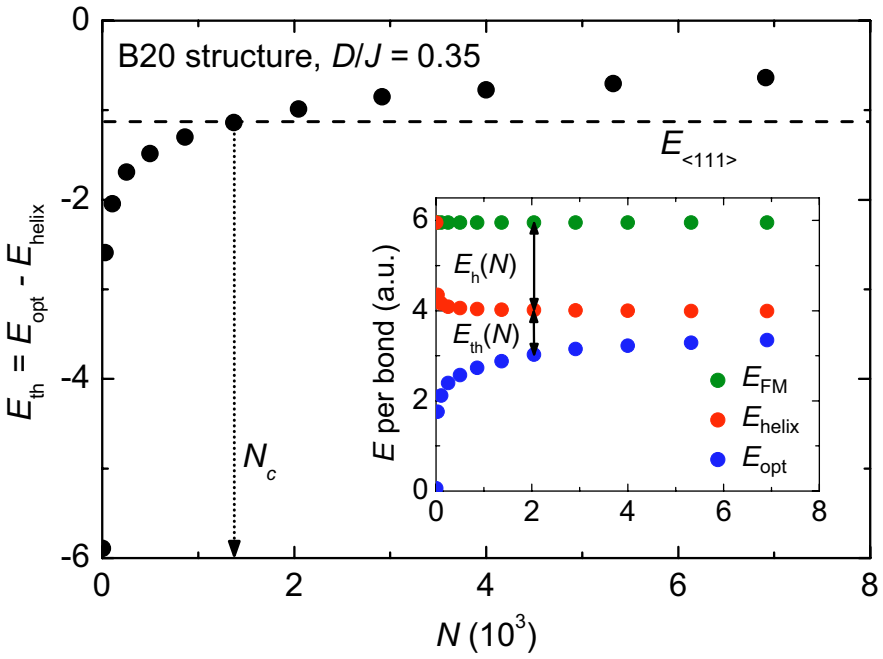

Figure 2.17: Energy considerations for clusters in the B20 structure with $D/J = 0.35$, corresponding to a helix period of about 52.1 Å. The inset shows energy per bond calculated according to Eq. (2.7) (where the crystal potential is neglected!) for ferromagnetic order (green), helical order along [1 1 1] (red) and the triple-helix structure (blue) as a function of the number of sites N. $E_{\rm h}(N)$ is defined as the difference of $E_{\rm helix}(N)$ and $E_{\rm FM}(N)$. $E_{\rm th}(N)$ denotes $E_{\rm opt}(N) - E_{\rm helix}(N)$ and is shown in the main panel in comparison to $E_{\langle 111\rangle}$, the energy gained by locking the helix along $\langle 1\ 1\ 1\rangle$ as favored by the crystal potential. The magnitude of $E_{\langle 111\rangle}$ was chosen somewhat larger than estimated from experimental data (Eq. (2.9)) to qualitatively illustrate the competition of the two ground states as discussed in the main text.

2.4 Interpretation

The above mechanism elucidates the nature of partial order which can now be explained by finite-size triple-helix clusters that form islands inside the paramagnetic phase above $T_{\rm C}$. They are clearly favored whenever thermal fluctuations appropriately reduce the magnetic correlation length. The average cluster size decreases towards higher temperature. This 'melting' of the clusters is not characterized by a specific temperature, but rather occurs in a gradual fashion with the bigger clusters melting first. That is the key mechanism behind the glassy crossover to the high-temperature paramagnetic phase instead of a well-defined phase transition. On lowering T, as clusters become larger, their diffusion slows down and when their boundaries start to touch, the helical phase

pinned by the crystal potential becomes more favorable. At that point a first-order phase transition to the topologically distinct helical phase occurs.

Comparison with experimental results

Indeed, neutron data depicted in Fig. 2.5 (c) point towards a first-order phase transition: Cooling below T_C induces a very sharp increase of intensity at the [1 1 1] satellite position which is accompanied by an abrupt drop of intensity at the [1 1 0] position indicating partial order. Fig. 2.18 shows the comparison of these data with the specific heat from [33] revealing a two-component lineshape that can now be explained: Coming from low T, we interpret the sharp peak as marking the reorientation of helical order below T_C into triple-helix-based clusters above T_C. The observed small thermodynamic weight of this first-order transition results from the small difference in the free energy between the helical phase and the triple-helix-based phase. Most of the weight appears at higher temperatures due to the gradual melting of the triple-helix clusters. In fact, it appears as if the sharp specific-heat anomaly "resides" on a broad background due to this gradual melting.

The decreasing size of the triple-helix clusters explains the broadening of the magnetic satellite peaks in the **Q** scans (Fig. 2.5 (a)) as this is consistent with a reduction of the correlation length. Furthermore, the smaller the number and size of the clusters towards increasing T, the faster should their diffusive motion become leading to the gradual increase of the energy linewidth and to the reduction of the magnetic intensity (Figs. 2.8 (a) and (b)). Due to their finite size, dynamics at $\mathbf{q} = (0.018\ 0.018\ 0)$ remain considerably slower at any temperature than paramagnetic (chiral) fluctuations at $\mathbf{q} = (0.05\ 0.05\ 0)$ (see Fig. 2.9 (c)).

Calculations on Fe-doped MnSi

Analogous to the temperature scale determining the magnetic correlation length ξ via thermal fluctuations, doping MnSi with impurities should have an impact on the the correlation length as well: At a given temperature, the substitution of a certain percentage x of Mn atoms with non-magnetic Fe atoms in $Mn_{1-x}Fe_xSi$ should reduce ξ and thereby stabilize the triple-helix structure. Thus T_C should decrease as previously reported [40]. Indeed, the SANS spectrum of $Mn_{0.85}Fe_{0.15}Si$ at ambient pressure is a ring characteristic of triple-helix order even at the lowest temperature of 1.5 K (see Fig. 2.19 (left panel)).

In corresponding calculations, non-magnetic impurities were modeled as zero moment sites that were randomly chosen among all N sites. Fig. 2.19 (right panel) reveals that, in fact, for a given cluster size $N = const.$ (i.e., $T = const.$) the energy of respective optimized triple-helix configurations is reduced upon increasing the number of

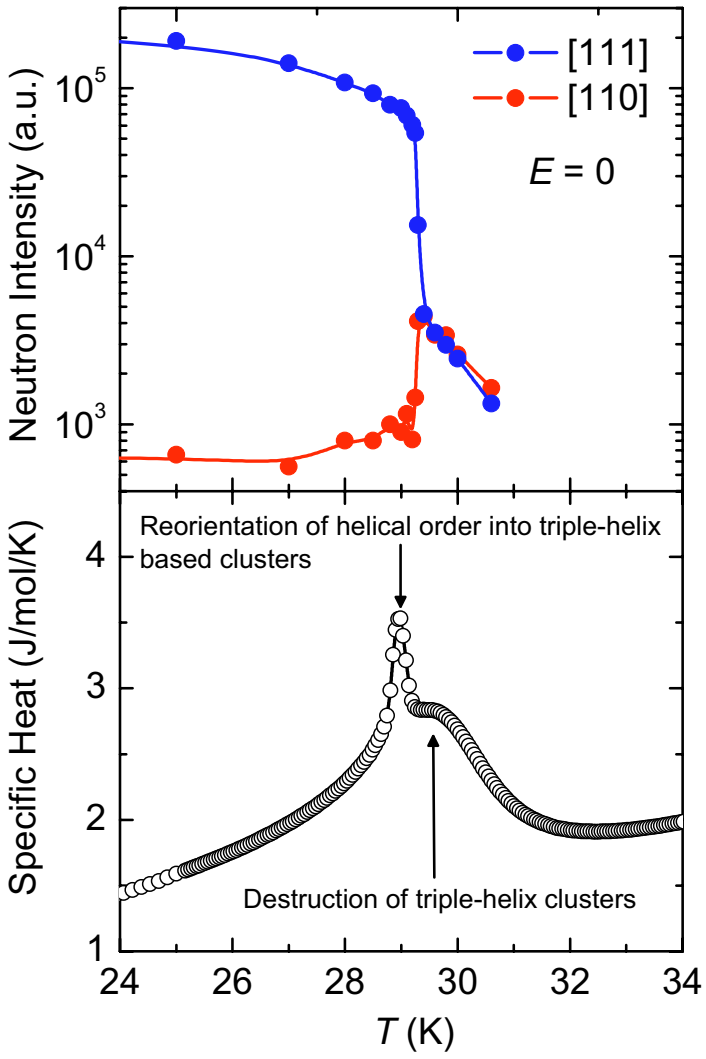

Figure 2.18: Specific heat data from [33] in comparison to the neutron intensity at [1 1 1] and [1 1 0] positions on the sphere (see Fig. 2.5 (c)). The offset in temperature of 0.3 degrees between the neutron and specific heat data is probably due to a different calibration of the thermometers or a temperature gradient between the sample and temperature sensor in the neutron measurement.

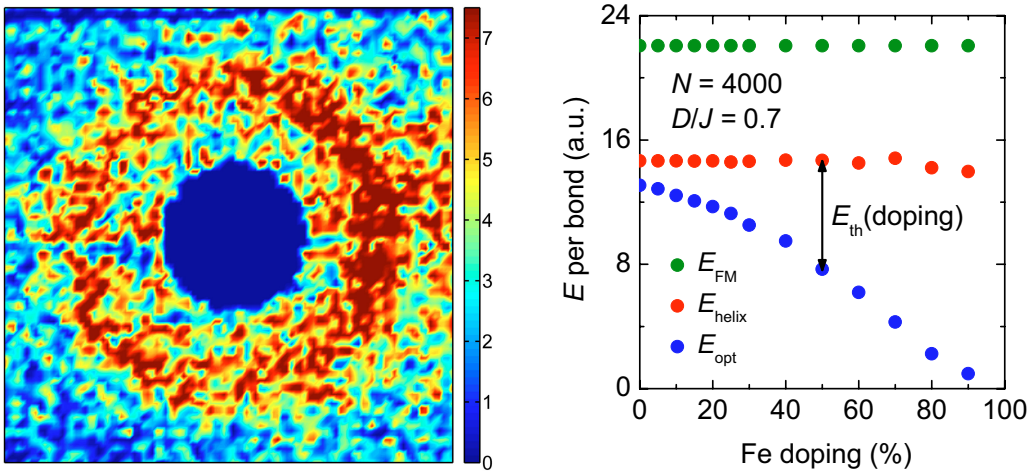

Figure 2.19: Effect of Fe doping in MnSi. (Left panel) SANS image of neutron scattering from $Mn_{0.85}Fe_{0.15}Si$ measured at 1.5 K. The ring of scattering is characteristic of partial order. The small asymmetry of the intensity from left to right results from a sloping background coming from the cryostat. The direct beam in the center was masked. (Right panel) Energy considerations for $10 \times 10 \times 10$ unit cell B20 clusters with $D/J = 0.7$ corresponding to a helix period of about 27.3 Å. Fe doping is modeled by randomly choosing a certain percentage of the $N = 4000$ sites to be empty. The energy per bond calculated according to Eq. (2.7) for ferromagnetic order (green), helical order along [1 1 1] (red) and the triple-helix structure (blue) is shown as a function of doping. (Note that at a given doping level, all three structures have the same (random) zero moment sites, respectively.). Data at zero doping correspond to $N = 4000$ in Fig. 2.11 (d).

impurities.[9] Regarding the competition of the crystal potential (i.e., $E_{\langle 111 \rangle}$) with the tendency to form triple-helix-based structures (i.e., E_{th}) as illustrated in Fig. 2.17, these results are indicative of increased triple-helix stability at a given temperature (i.e., N). As a consequence, the triple-helix-based phase persists to lower temperatures.

Exploring the $T - p$ phase diagram

According to the $T - p$ phase diagram (Fig. 2.2 (a)), hydrostatic pressure p lowers T_{C} and partial order seems to become the ground state beyond $p_c = 14.6$ kbar. There, it reveals a magnetic correlation length of several helix periods (inferred from the resolution limited FWHM in longitudinal direction [3]) as opposed to about half the helix period (~ 100 Å) just above T_{C} at ambient pressure [29]. Our calculations were

[9] Note that calculations were performed on clusters consisting of $8 \times 8 \times 8$ and $10 \times 10 \times 10$ B20 unit cells considering both cases $D/J = 0.35$ and $D/J = 0.7$. All gave the same result on a qualitative basis, therefore only the most significant case of $N = 4000$ and $D/J = 0.7$ is shown.

limited to clusters smaller than four helix periods, nevertheless, our investigation still offers a number of insights relevant to the high-pressure phase.

As illustrated in Fig. 2.17, reducing $|E_{\langle 111\rangle}|$ (e.g., by applying pressure) shifts the point of intersection with $E_{\rm th}$ towards bigger cluster sizes $N_c(p)$, corresponding to lower $T_{\rm C}(p)$. This explains the continuous decrease of $T_{\rm C}(p)$ with pressure – at least as long as the thermal energy of fluctuations at $N_c(p)$ is sufficient to overcome the potential well separating the two competing states. However, close to the critical pressure $p_c = 14.6\,\text{kbar}$ where the crystal potential is small but still finite, thermal fluctuations at the temperature T' corresponding to $N_c(p \gtrsim p_c)$ are too weak to actually drive the first-order transition to the locked helix being the ground state below T'. Consequently, finite-size triple-helix clusters continuously freeze into a glass-like meta-stable state that persists to lowest temperatures. This mechanism explains why the locked-helix phase is never found above $p_c = 14.6\,\text{kbar}$ (without the presence of a magnetic field $\mathbf{B}$) although previous experiments revealed that the crystal potential disappears not below $20\,\text{kbar}$[10] [31].

On the other hand, at $p \approx 21\,\text{kbar}$, where the crystal anisotropy vanishes completely, applying a field of $0.4\,\text{T}$ to zero-field-cooled MnSi at $T = 0.35\,\text{K}$ induces helical order with the helical propagation vector aligned along the field (regardless of its direction with respect to the crystal axes) [31]. Interestingly, even if the field is switched off again, helical order aligned with the former field direction remains although no crystal potential is present. (Corresponding satellite peaks observed with SANS [31] broaden in transverse direction and weaken but still reveal intensity considerably above the background.) In line with the above argumentation, two scenarios might explain why there is no transition to the triple-helix phase: (1) Assuming the triple-helix-based arrangement is the ground state (without crystal potential), thermal fluctuations might be too weak to drive the first-order transition to this ground state and hence the system remains in the meta-stable locked-helix state. (2) Alternatively, at very low temperatures (where the correlation length is large) the single-helix state might be the ground state even without the presence of a crystal potential. This could be due to the fact that, as opposed to the single-helix, the triple-helix-based clusters can never assume infinitely long correlation lengths because topological defects occur above a certain cluster size.

Of course, large clusters as well as the infinite systems will have to be theoretically investigated to corroborate the above interpretation.

The tendency to form topological defects

As mentioned in Sec. 2.1, below $T_{\rm C}$ the helical propagation vector $\mathbf{k}_{\rm h}$ is locked along $\langle 1\ 1\ 1\rangle$ within about 3.35° (magnetic mosaic spread as observed in [31]). This is in

[10] Also, the somewhat abrupt drop of $T_{\rm C}(p)$ above $p^* = 12\,\text{kbar}$ as reported in [3] might be related to this scenario.

pronounced contrast to the crystal mosaic spread being an order of magnitude smaller (0.2°). The magnetic mosaic spread can be significantly reduced at all pressures upon applying a field along $\mathbf{k}_\mathrm{h}$ but is fully recovered once the field is switched off again [31]. Seemingly, some mechanism actively drives the system away from helical order.

We think that this mechanism originates from the inherently frustrated nature of the Hamiltonian (Eq. (2.6)): In 3D, it is energetically favorable to form topological defects to partially overcome frustration. This results in a tendency towards distributed helical propagation directions that competes with the crystal potential tending to align $\mathbf{k}_\mathrm{h}$ along a favored direction. At low pressure and below T_C, this tendency is masked by the strong crystal potential but still enhances the magnetic mosaic spread. At high pressure (or above T_C), where the crystal anisotropy is negligible, it accounts for the disordered helix directions characteristic of the triple-helix-based arrangement.

Weak locking of partial order at high pressure

The fact the PO is weakly locked in $\langle 1\ 1\ 0\rangle$ directions at high pressure only (see Fig. 2.2 (a)) remains a puzzling issue. It could be related to pressure-induced changes of the crystal potential weakly favoring $\langle 1\ 1\ 0\rangle$ above p^*. On the other hand, at a given pressure p between p^* and p_c the single-helix below T_C is still locked along $\langle 1\ 1\ 1\rangle$. In this pressure range, the crystal anisotropy would also have to be temperature dependent to account for this behavior.

Another possible explanation is suggested by our calculations: The weak locking of PO might have nothing to do with the crystal potential but instead could be related to the B20 structure itself. At low pressure, where the correlation length in the PO phase above $T_\mathrm{C} = 29.5\,\mathrm{K}$ is relatively small, neutron intensity is found to be uniform on the sphere. At high pressure above p^*, where the correlation length in the PO phase is substantially increased because T_C is low, intensity is weakly peaked in $\langle 1\ 1\ 0\rangle$ directions. Hence, the magnetic correlation length ξ might be the crucial parameter deciding about whether or not $\langle 1\ 1\ 0\rangle$ is structurally favored in the PO phase.

In order to test this hypothesis by virtue of our cluster calculations, an examination of large cluster sizes would be needed to properly model the high-pressure PO phase where the correlation length is long. Unfortunately, simulations of SANS spectra from B20 clusters bigger than around $8 \times 8 \times 8$ unit cells were not possible (limited by the computer power[11]). Nevertheless, preliminary results could be obtained owing to the following assumption: We model the magnetic correlation length ξ by means of a dimensionless 'effective' magnetic correlation length ξ_{eff} representing the number of helix periods accommodated in a cluster. More specifically,

$$\xi_{eff} = \frac{\bar{a}_N}{\lambda_\mathrm{h}}\,, \tag{2.11}$$

[11]Note that the signal of 11 clusters of different shapes is used to calculate only one of the spectra such as shown in Fig. 2.20 (a-c) (see footnote on page 41).

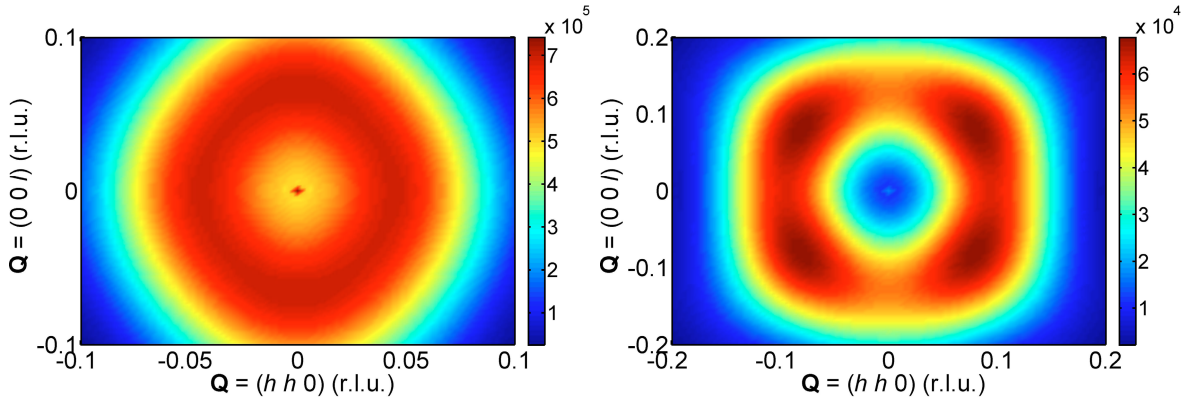

(a) $\xi_{eff} \sim 0.70$ ($N \sim 2048$, $D/J = 0.35$)

(b) $\xi_{eff} \sim 1.00$ ($N \sim 864$, $D/J = 0.7$)

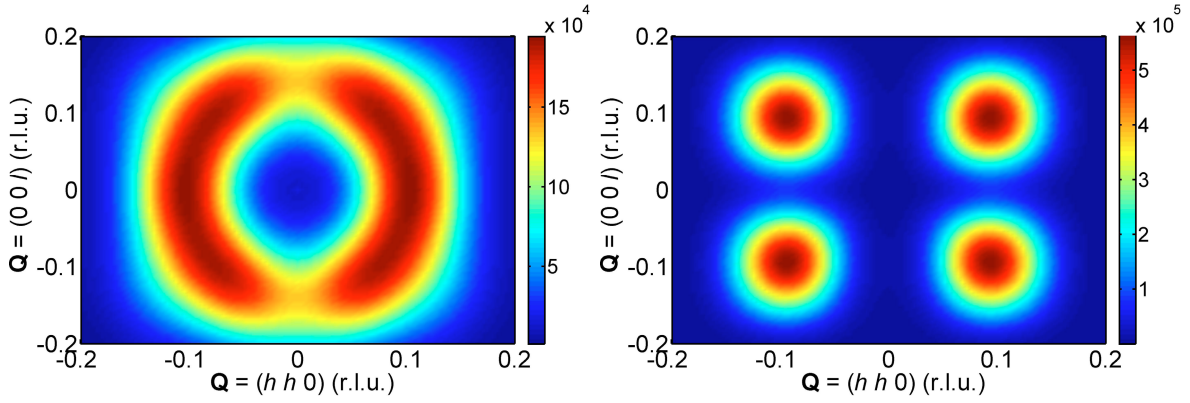

(c) $\xi_{eff} \sim 1.34$ ($N \sim 2048$, $D/J = 0.7$)

(d) $\xi_{eff} \sim 1.34$ ($N \sim 2048$, $D/J = 0.7$)

Figure 2.20: Neutron intensity calculated from model clusters in the MnSi B20 structure in plane that is spanned by reciprocal [1 1 0]/[0 0 1] axes around (0 0 0). Different cluster sizes and ratios D/J were considered to simulate PO with various effective magnetic correlation lengths ξ_{eff} as defined in Eq. (2.11). Panels (a-c) show the triple-helix structure for cluster sizes of around $6 \times 6 \times 6$ unit cells ($N \sim 864$ sites) and around $8 \times 8 \times 8$ unit cells ($N \sim 2048$ sites) with $D/J = 0.7$ (helix period of ~ 27.3 Å) and $D/J = 0.35$ (helix period of ~ 52.1 Å). (d) Locked-helix structure for $N = 2048$ sites and $D/J = 0.7$ corresponding to (c).

where λ_{h} is the wavelength of the helix and $\bar{a}_N$ denotes the average edge length of clusters consisting of about N sites. Thereby, clusters of different sizes optimized for different ratios D/J (producing different helix periods) can be compared at least on a qualitative basis.

Simulated SANS spectra corresponding to ξ_{eff} between 0.70 and 1.34 are depicted in Fig. 2.20. A relatively short correlation length $\xi_{eff} \sim 0.70$ (a) results in uniform intensity on the sphere, notably no difference between $\langle 1\ 1\ 1 \rangle$ and $\langle 1\ 1\ 0 \rangle$. This resembles the signature of PO at ambient pressure[12]. On the other hand, increasing the simulated ξ_{eff} to 1.00 (b) and 1.34 (c) reveals a pronounced tendency towards enhanced intensity at $\langle 1\ 1\ 0 \rangle$ mimicking the signature of PO at elevated pressure where ξ is longer because T_c is low.

In order to check that this preference for $\langle 1\ 1\ 0 \rangle$ is intrinsic, various possibilities for artifacts causing the same signature would have to be ruled out. For instance, the rectangular cluster shape combined with the finite size of the clusters might be responsible for a preferred direction of the helix propagation vectors. Due to time reasons however, calculations on much larger clusters of different shapes have not yet been possible but should certainly be considered for the future.

The extended NFL phase

Our experiments may also shed light upon the long-standing issue of the NFL resistivity $\rho \sim T^{3/2}$ observed in a significantly larger part of the $T-p$ phase diagram than partial order [26]. The neutron scattering measurements at high pressure [3] were two orders of magnitude less sensitive than at ambient pressure because of much smaller samples and a large background caused by the pressure cell. Since in the present work we found the disappearance of PO with increasing temperatures to be gradual, the triple-helix clusters likely persist to much higher T and p than detectable with the sample in the pressure cell. Thus, the gradual change of the scattering rate of conduction electrons due to the breaking of the triple-helix clusters with increasing temperature may be responsible for the NFL behavior at high pressures. It is interesting to note that scattering by 'helimagnons', i.e., spin waves of a helically ordered magnet, yields a $T^{5/2}$ dependence of ρ [41], although the effect of dynamical disorder in the PO phase has not been investigated theoretically.

On the other hand, the resistivity of $Mn_{1-x}Fe_xSi$ assumes a NFL form as well [42], providing evidence that triple-helix order induces NFL behavior. However, the functional form of $\rho(T)$ in $Mn_{1-x}Fe_xSi$ is different from the $T^{3/2}$ dependence in pure MnSi at high pressures, possibly related to the pinning of the triple-helices by the impurities.

[12] Relating $\bar{a}_N$ to the correlation length of ~ 100 Å measured just above T_c at ambient pressure [29] and taking into account the real helix period of about 180 Å yields $\xi_{eff} \sim 0.55$. This value is indeed very close to $\xi_{eff} \sim 0.70$ corresponding to the simulation.

Boundary conditions

Regarding the spin cluster calculations, we chose to impose open boundary conditions because we think that this models the physics appropriately: Whenever the magnetic correlation length has been considerably reduced by temperature or doping with Fe-impurities, the triple-helix clusters form isolated islands separated by domain boundaries with the domain boundary density increasing with T. Open boundary conditions are equivalent to the clusters being surrounded by randomly oriented moments for the purposes of calculating E_{th}, whereas periodic boundary conditions would correspond to an attempt to understand the infinite system, which is outside the scope of this work.

2.5 Conclusion

To summarize, our measurements and calculations showed that partial magnetic order in MnSi is most likely a collection of slowly diffusing topologically complex chiral-ordered spin clusters that form spontaneously in the paramagnetic phase up to fairly high temperatures. Their presence can naturally explain most of the unusual bulk properties of MnSi in a qualitative manner. With the physics of chiral systems being an extremely interesting present subject in condensed matter, more detailed calculations including transport properties would be highly desirable in order to establish a closer link between the existence of topological chiral excitations, which we suggest to be triple-helix clusters, and non-Fermi-liquid behavior.

Chapter 3

Pressure dependence of magnetic order in $CeCu_{5.5}Au_{0.5}$

3.1 Introduction

$CeCu_6$ is a prototype heavy-fermion (HF) system. It crystallizes in the orthorhombic *Pnma* structure (lattice constants $a = 8.112\,\text{Å}$, $b = 5.102\,\text{Å}$ and $c = 10.162\,\text{Å}$) with a small monoclinic distortion of about 1.5° below 230 K. In order to avoid confusion, the orthorhombic notation is used in the following. The unit cell contains four Ce atoms each of which is surrounded by 19 Cu atoms with a Ce-Ce distance of 4.83 Å (Fig. 3.1 (a)).

Ce $4f$ moments in $CeCu_6$ form a regular sublattice within the metallic Cu matrix. Due to their strong localization, they interact only weakly with conduction electrons at high temperature[1]. However, a crossover of the magnetic behavior occurs towards decreasing temperature where the $4f$ moments are screened by conduction electrons owing to the Kondo effect. The associated energy gain sets the (Kondo) temperature scale T_K that strongly depends on the hybridization strength of the $4f$ electrons with the conduction band[2]. Experimentally, T_K is usually related to the pronounced increase of the electrical resistivity $\rho(T)$ towards lower T resulting from strong fluctuations of the Fermi surface in the crossover temperature region. (The high-field specific heat of $CeCu_{6-x}Au_x$ is properly described within a single-ion Kondo model, i.e., the resonance-level model, yielding an estimate of $T_K \approx 6.2\,\text{K}$ for $CeCu_6$ [46].) A maximum of $\rho(T)$ at even lower temperature T_{coh} signals the onset of a coherent state leading to a behavior at very low T that is rather well described by Fermi-liquid (FL) theory:

[1] Effects due to the crystal field and spin-orbit interaction are not considered here.

[2] Frequently, the symbol T^* is used for the characteristic temperature of a Kondo lattice, instead of T_K denoting the energy gain associated with the formation of a collective spin singlet state by virtue of the single-ion Kondo effect (see [45] for a detailed discussion). Within the scope of this brief introduction, this discrimination is neglected in the following.

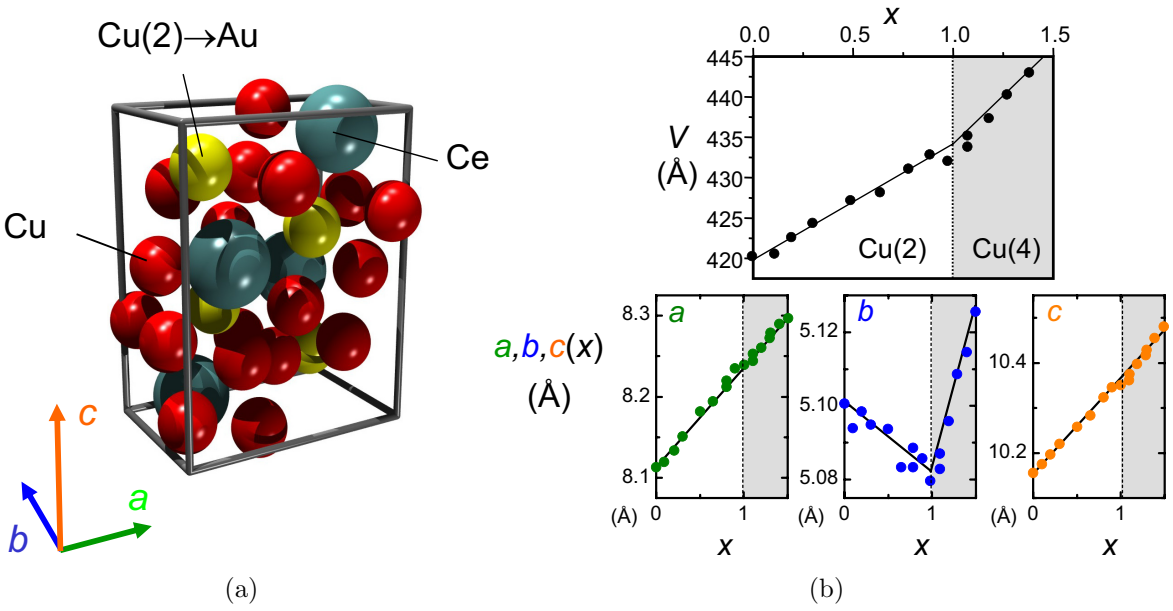

Figure 3.1: (a) Orthorhombic unit cell of $CeCu_{6-x}Au_x$ containing four Ce atoms (blue). For $x \leq 1$, Au atoms exclusively occupy the Cu(2) positions (yellow) in the $CeCu_6$ structure. Other Cu atoms are shown in red. (b) Upper panel: The volume of the unit cell increases as $V(x) = (419.9 + 14.29\,x)\,\text{Å}^3$ up to $x = 1$ above which Cu(4) positions are occupied changing the slope of $V(x)$. Lower panels: Interestingly, not all lattice parameters increase with growing Au content: b decreases until all Cu(2) positions are occupied ($x = 1$) and increases upon further doping. Figures are adopted from [43], data correspond to those presented in [44].

One such hallmark is the T^2 dependence of the resistivity of $CeCu_6$ between 40 and 200 mK [47] that is characteristic of dominant quasiparticle-quasiparticle scattering. The huge linear specific heat coefficient $\gamma = 1.6\,\text{J/mol K}^2$ and the strongly enhanced magnetic susceptibility χ [47, 48, 49], both only weakly temperature dependent, point to a very large effective mass m^* of the quasiparticles. $CeCu_6$ exhibits a pronounced magnetic anisotropy at temperatures below 1.1 K with the magnetization ratios along the three axes $M_c : M_a : M_b \approx 10 : 2 : 1$ [47]. Usually, magnetic fields are therefore applied along the easy c direction. Long-range antiferromagnetic order with preferred spin-alignment along the crystallographic a direction is only observed for temperatures $T < 2 - 3\,\text{mK}$ [50] whereas short-range antiferromagnetic fluctuations also appear at higher temperatures [51].

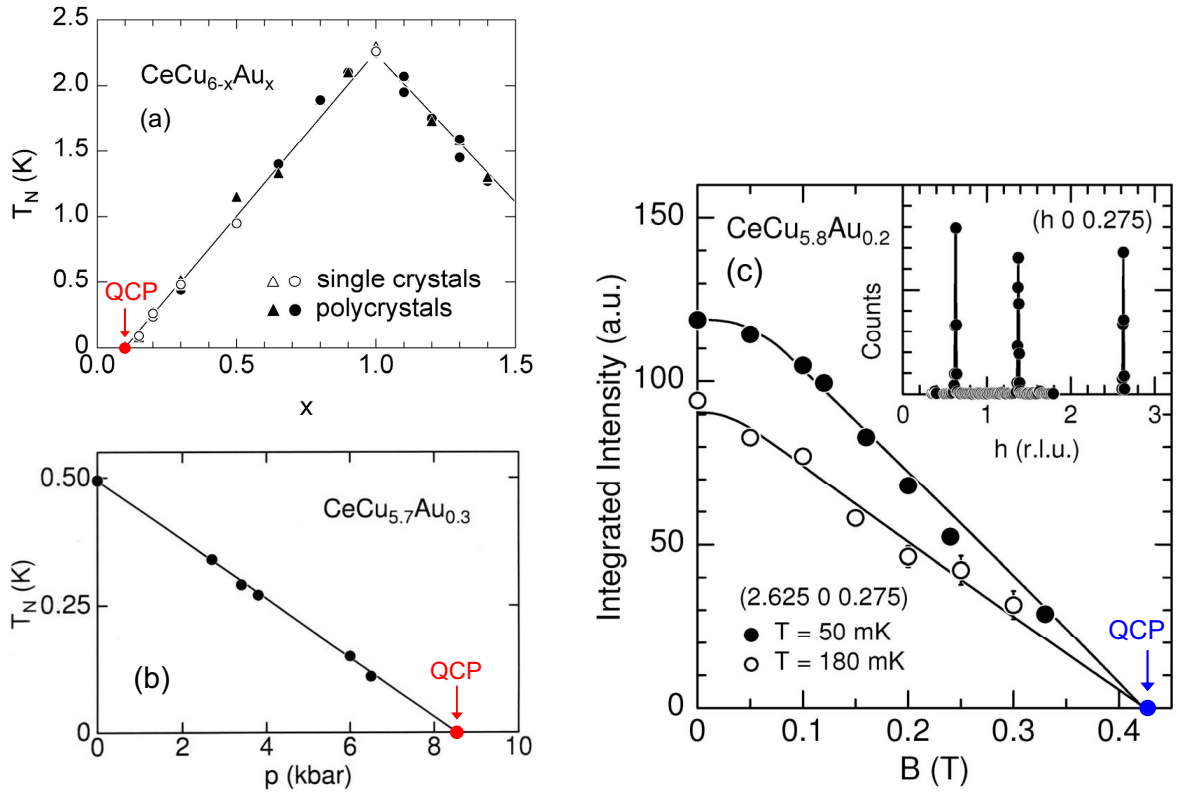

Figure 3.2: $CeCu_{6-x}Au_x$ can be tuned into quantum criticality by Au concentration x (a), by applying hydrostatic pressure p (b) or by applying a magnetic field B (c). (a) The Néel temperature T_N of $CeCu_{6-x}Au_x$ vs. Au concentration x as determined from specific heat (triangles) and magnetic susceptibility (circles) [44]. For $0.1 \leq x \leq 1$ where Au exclusively occupies the Cu(2) positions in the $CeCu_6$ structure (see Fig. 3.1), T_N varies linearly with x. The sharp kink at $x = 1$ is associated with the occupancy of all Cu(2) positions. (b) Pressure dependence of T_N of magnetically ordering $CeCu_{5.7}Au_{0.3}$ with a linear fit [52]. The sample is tuned quantum critical at $p \approx 8.2$ kbar. (c) Neutron scattering results obtained on $CeCu_{5.8}Au_{0.2}$ at temperatures below $T_N \approx 250$ mK as adopted from [53]. Inset: Elastic $\mathbf{Q}$ scan at $l = 0.275$ along $(h\ 0\ 0)$ at $T = 50$ mK through the positions of three equivalent magnetic Bragg peaks around nuclear (0 0 0) and (2 0 0) Bragg peaks (corresponding to a magnetic ordering wave vector $\mathbf{q}_m = (0.625\ 0\ 0.275)$). Main frame: Integrated neutron intensity of the magnetic Bragg peak at $\mathbf{Q} = (2.625\ 0\ 0.275)$ as a function of the magnetic field B applied along the crystallographic c direction at $T = 50$ mK and 180 mK. Magnetic order is suppressed by a field $B_c \sim 0.42$ T as estimated from the linear extrapolation to zero. As explained in the main text, experiments are indicative of equivalent microscopic mechanisms driving respective x- or p-tuned quantum phase transitions (red) that are in marked contrast to field-tuned quantum criticality (blue).

3.1.1 Tuning to quantum criticality

Substituting Cu with isoelectric Au leads to a lattice expansion that is due to the larger Au radius (see Fig. 3.1 (b)). Thus, the hybridization of the Ce $4f$ electrons with the conduction electrons and hence the exchange integral J decreases leading to a stabilization of the local $4f$ moments that can now order via the indirect Ruderman-Kittel-Kasuya-Yosida (RKKY) interaction. As a result, long-range incommensurate antiferromagnetism (AF) is introduced in the alloy series $CeCu_{6-x}Au_x$ for $x > x_c \approx 0.1$ below the respective Néel temperature T_N (Fig. 3.2 (a)). In the vicinity of the quantum critical point (QCP) at $x = x_c$, i.e., at the magnetic instability where $T_N = 0$, significant deviations from FL behavior have been observed in thermodynamic and transport data, nicknamed non-FL (NFL) behavior [5, 6]. As an example, the specific heat and the electrical resistivity are found to follow unusual temperature dependencies:

$$\begin{aligned} &\text{Specific heat} && \frac{C(T)}{T} = a \ln \frac{T}{T_0} \,, \\ &\text{Electrical resistivity} && \varrho(T) = \varrho_0 + A'T \,. \end{aligned} \tag{3.1}$$

The Néel temperature of magnetically ordering $CeCu_{6-x}Au_x$ with $x > 0.1$ can be continuously reduced by applying hydrostatic pressure p as shown for the case of $x = 0.3$ in Fig. 3.2 (b). Since the volume of the unit cell and with it the hybridization of the Ce $4f$ electrons with the conduction band is decreased, pressure reverses the effect of doping with Au. But it is important to note that pressure contracts all lattice parameters simultaneously as opposed to the substitution of Cu with Au which affects the lattice parameters in an anisotropic fashion (see Fig. 3.1 (b)). Consequently, the variation of T_N with the relative volume change[3] ΔV is more pronounced if ΔV is due to x instead of p as described in detail in [44]. Nevertheless, the same quantum critical behavior of $CeCu_{5.9}Au_{0.1}$ as given in Eq. (3.1) with the same constants a and T_0 is recovered by applying appropriate pressure to magnetically ordering $CeCu_{6-x}Au_x$ with $x > 0.1$. This fact is particularly interesting, since it suggests that disorder (introduced by a certain amount of Au $0 < x < 1$) does not have decisive influence on the NFL behavior at the respective QCP.

The QCP can be tuned continuously not only by x or p but also by magnetic field B as demonstrated in Fig. 3.2 (c). The temperature dependence of the specific heat and the electrical resistivity at the field-tuned QCP is in pronounced contrast to Eq. (3.1):

$$\begin{aligned} &\text{Specific heat} && \frac{C(T)}{T} = \gamma_0 - a'\sqrt{T} \quad \text{for } T \to 0 \,, \\ &\text{Electrical resistivity} && \varrho(T) = \varrho_0 + A''T^{3/2} \,. \end{aligned} \tag{3.2}$$

The different behavior is illustrated in Fig. 3.3, where data of the specific heat obtained

[3] $\Delta V := (V - V_0)/V_0$ where for any concentration x, V_0 is the respective volume of the unit cell at ambient pressure.

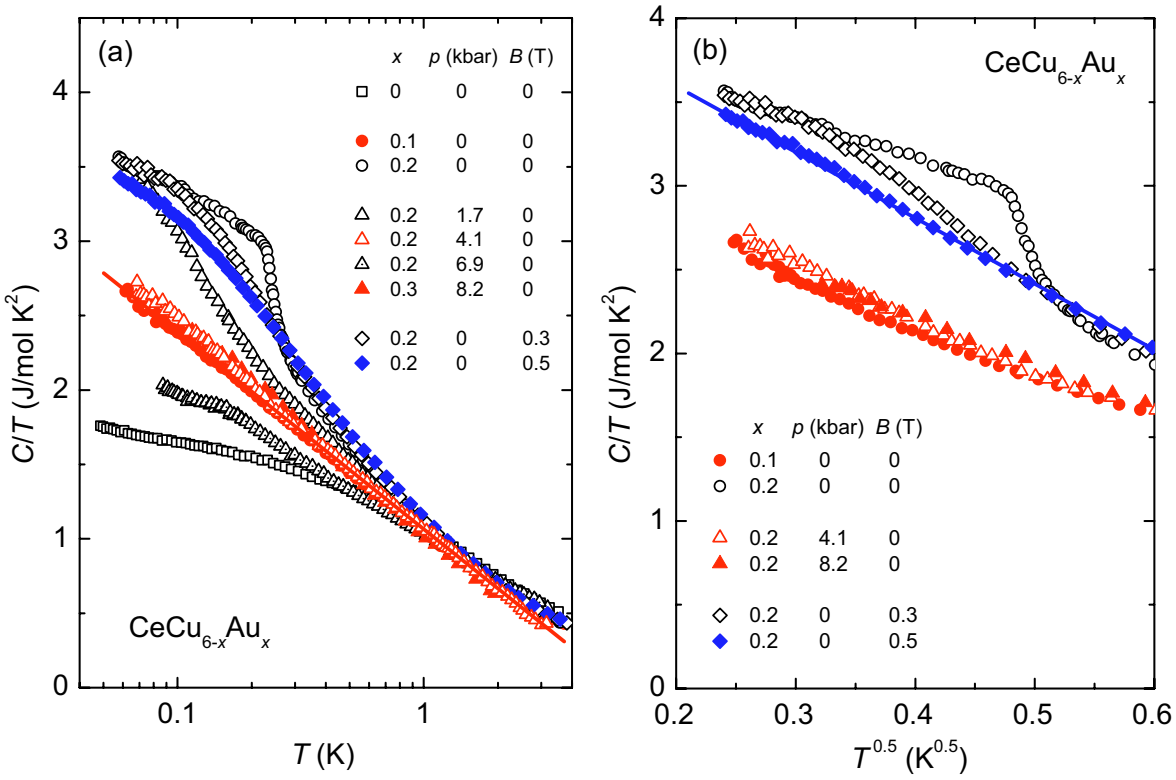

Figure 3.3: Specific heat C of $CeCu_{6-x}Au_x$ plotted as C/T vs. T on a logarithmic scale (a) and vs. $T^{0.5}$ (b) for various hydrostatic pressures p at magnetic field $B = 0$ (triangles) and different B at $p = 0$ (diamonds). Data at $p = 0$ and $B = 0$ are shown as circles ($x > 0$) and squares ($x = 0$). Data shown in red (blue) correspond to respective x- or p-tuned (B-tuned) quantum critical systems (compare color-coding in Fig. 3.2). All data are adopted from [5, 54]. (a) The slight increase of C/T for $CeCu_6$ (squares), instead of $C/T \sim const.$ as expected for a FL, might be a precursor of magnetic order below $2 - 3\,\mathrm{mK}$. For $x = 0.2$ (black circles), the kink at $\sim 250\,\mathrm{mK}$ signals the onset of AF order that is shifted towards lower T upon applying $p = 1.7\,\mathrm{kbar}$ (black open triangles). Data at the critical pressure $p_{c,x=0.2} = 4.1\,\mathrm{kbar}$ (red open triangles) coincide with data obtained on $CeCu_{5.7}Au_{0.3}$ at $p_{c,x=0.3} = 8.2\,\mathrm{kbar}$ (red filled triangles) and $CeCu_{5.9}Au_{0.1}$ at $p = 0$ (red filled circles). All three data sets follow the same $T \to 0$ NFL behavior that is expected in the 2D-HMM scenario (see Eq. (3.1) as indicated by the straight line). The system with $x = 0.2$ can even be tuned towards the FL-like behavior of $CeCu_6$ upon applying $p > p_c$ (black dotted triangles). The appreciable curvature of data shown in blue marks the different NFL behavior at the field-tuned QCP that in turn can be described within the 3D-HMM scenario (straight line in (b) illustrating Eq. (3.2)).

from samples with various Au concentrations x at several pressures p and magnetic fields B are shown.

The field-tuned NFL behavior (Eq. (3.2)) is in agreement with the standard Hertz-Millis-Moriya (HMM) model of three-dimensional (3D) itinerant quantum criticality for antiferromagnets [55, 56, 57, 58]. In this picture, heavy quasiparticles with 3D dynamics undergo singular scattering by incipient 3D spin fluctuations. On the other hand, the NFL behavior that is observed when approaching x- or p-tuned QCP (Eq. (3.1)) can be explained invoking a quasi-2D fluctuation spectrum coupled to quasiparticles with 3D dynamics. This was demonstrated by Rosch et al. [59] in an analysis similar in spirit to that of HMM. At the critical concentration $x_c = 0.1$, dynamic correlations appear revealing a rod-like structure in q space (see Fig. 3.4 (a)) that can be related to 2D correlations between Ce atoms in real space [7]. Quantum critical fluctuations exhibiting quasi-2D correlations corroborate the 2D-HMM scenario. However, Schröder et al. [60, 61] discovered an unusual form of the dynamical susceptibility at the concentration-tuned QCP ($x = 0.1$):

$$\chi^{-1}(q, E, T) = c^{-1} \left[(\theta(q))^{\alpha} + (T - iE)^{\alpha} \right] \tag{3.3}$$

with an anomalous exponent $\alpha = 0.75$ ($\alpha = 1$ would be expected in a Lorentzian response). Here, the q dependence of the fluctuations is exclusively governed by an energy-independent generalized Curie-Weiss temperature $\theta(q)$ and, surprisingly, the critical slowing down of the fluctuations is independent of q, suggesting local quantum criticality and prompting alternative scenarios [62, 63]. The dimensionality of the microscopic mechanisms driving the quantum phase transition is thus of key interest.

3.1.2 Magnetic ordering

Previous neutron scattering experiments on $CeCu_{6-x}Au_x$ at ambient pressure revealed the positions of the magnetic Bragg peaks for $x > 0.1$ in the reciprocal (h 0 l) plane [7]: Fig. 3.4 (a) shows several symmetry-equivalent magnetic peaks corresponding to nuclear (0 0 0) and (2 0 0) Bragg peaks. (The (1 0 0) nuclear peak has zero structure factor because of the selection rule ($h + k + l$ even) in the $Pnma$ crystal structure.) The 2D fluctuations for $x = 0.1$ (associated with shaded rods) can be regarded as a precursor of the 3D AF ordering at higher Au concentration as the magnetic Bragg peaks for samples not too far from the magnetic instability, i.e., $x \leq 0.3$, are located on these rods at $\mathbf{q}_m \approx (0.62\ 0\ 0.27)$. For $x = 0.2$, peaks indicating short-range order appear at $\mathbf{q}_{m,sr} = (0.79\ 0\ 0)$ in addition to the Bragg peaks at $\mathbf{q}_m$. A substantial modification of the magnetic order occurs above a certain doping ratio (Fig. 3.4 (b)): Upon increasing x, the l component of $\mathbf{q}_m(x)$ first decreases slowly and then abruptly drops to zero between $x = 0.4$ and $x = 0.5$, resulting in $\mathbf{q}_m(x = 0.5) \approx (0.59\ 0\ 0)$ [64], while $T_N(x)$ varies linearly (Fig. 3.2 (a)). This apparent contrasting behavior needs clarification.

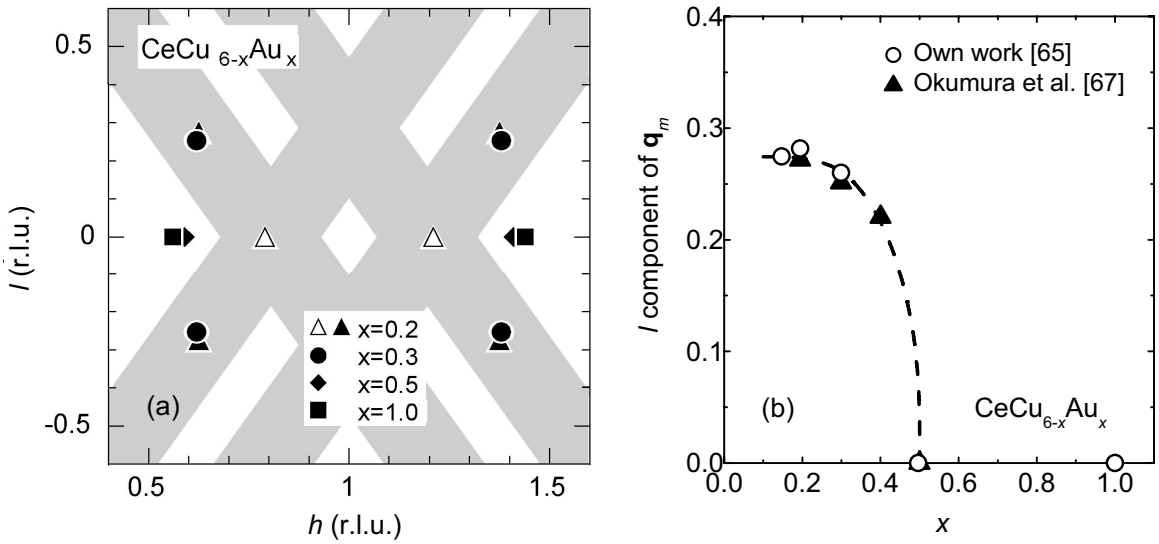

Figure 3.4: Neutron scattering results revealing the position of the magnetic ordering wave vector $\mathbf{q}_m$ of $CeCu_{6-x}Au_x$ at ambient pressure. (a) Doping dependence of several magnetic peaks in reciprocal (h 0 l) plane as adopted from [65]. Note that $\mathbf{Q} = \mathbf{q}_m + \mathbf{G}$ is shown where $\mathbf{G}$ = (0 0 0) and (2 0 0). Filled symbols correspond to Bragg peaks indicating long-range order, open symbols represent short-range ordering peaks. Shaded rods indicate dynamic correlations observed at the critical concentration $x = 0.1$. These rods are related by the orthorhombic $Pnma$ lattice symmetry and their width in h or l corresponds to the FWHM extracted from $\mathbf{Q}$ scans along (h 0 0) or (0 0 l) at $T < 100\,\mathrm{mK}$ and $\hbar\omega = 0.1\,\mathrm{meV}$ [7]. (b) Doping dependence of the l component of $\mathbf{q}_m$. The dashed line is a guide to the eye.

We therefore investigated the pressure dependence of the magnetic ordering of $CeCu_{5.5}Au_{0.5}$ using elastic neutron scattering. We primarily focused on the question of whether the same finite l component of $\mathbf{q}_m(x \leq 0.4)$ could be recovered upon applying pressure to a sample that orders along h at ambient pressure. Regarding macroscopic quantities such as thermodynamic and transport properties, the equivalence of the tuning behavior with x or p has been striking. However, it remains to be shown that this equivalence holds on a microscopic level, e.g., by virtue of the magnetic ordering wave vector $\mathbf{q}_m$. Probing its pressure dependence in comparison to the known variation with x also elucidates the microscopic role of disorder in $CeCu_{6-x}Au_x$.

3.2 Experimental results

Our experiment was performed on the cold triple-axis spectrometer PANDA operated at the FRM II reactor in Munich. Our single-crystalline sample[4] of $CeCu_{5.5}Au_{0.5}$ with a mass of 1.7 g was mounted in a Cu:Be clamped pressure cell together with a Pb sample as pressure gauge, using fluorinert FC 72 as pressure medium. In order to reduce the background generated by scattering from the pressure cell, a Cd shielding was wrapped around it leaving open the sample space. The use of a dilution refrigerator enabled cooling the sample to below 100 mK (with beam on). The scattering plane was spanned by reciprocal [1 0 0] and [0 0 1] axes. We focused on elastic scans over the magnetic Bragg peak in the (2 0 0) Brillouin zone due to the large structure factor there[5]. The instrument was operated in the elastic condition with $k_i = k_f = 1.5\,\text{Å}^{-1}$ with a Be-filter in the incident beam and open collimation.

3.2.1 Position of magnetic ordering peaks at different pressures

Fig. 3.5 shows the pressure dependence of the neutron intensity of $CeCu_{5.5}Au_{0.5}$ on a grid in the reciprocal (h 0 l) plane. Note that in comparison to Fig. 3.4 (a), only a small range covering the positions of the two upper right magnetic Bragg peaks is displayed in this figure. Fig. 3.5 (a) reveals that at ambient pressure[6] a strong magnetic Bragg peak is found at the incommensurate position $\mathbf{Q} = (1.420\ 0\ -0.005)$ in excellent agreement with previous results [64]. The small deviation of the l component from zero can be attributed to slight misalignments of the spectrometer and the sample orientation. The comparatively small background ($< 6\%$ of peak intensity) varies quadratically along (h 0 0) and linearly along (0 0 l) and is taken into account in any fit presented in the following. The weak feature around $\mathbf{Q} = (1.48\ 0\ l)$ can be clearly attributed to an Al-powder line[7] that exhibits no temperature dependence and is without effect on the magnetic signal. Upon applying $p = 3.6\,\text{kbar}$ (Fig. 3.5 (b)), the position of the Bragg peak significantly changes to $\mathbf{Q} = (1.402\ 0\ 0.194)$ assuming almost the same l component that has been found for $CeCu_{5.6}Au_{0.4}$ at ambient pressure (Fig. 3.4 (b)). This indicates that by pressure tuning the sample towards the QCP, not only the thermodynamic and transport data (as described in Sec. 3.1.1) but also the magnetic

[4]The sample was grown by V. Fritsch (Physikalisches Institut, Karlsruhe Institute of Technology (KIT), Germany).

[5]The Ce spins point along the crystal c axis [64]. Since only the component of the spin perpendicular to $\mathbf{Q}$ contributes to the measured intensity (Eq. (1.33) in Seq. 1.2.2), the magnetic signal would be very weak, e.g., in the (0 0 2) Brillouin zone although structurally allowed by the selection rule ($h + k + l$ even).

[6]Investigations at ambient pressure were performed with the sample in the pressure cell, too.

[7]Large parts of the dilution refrigerator that are partly in the beam are made of Aluminum.

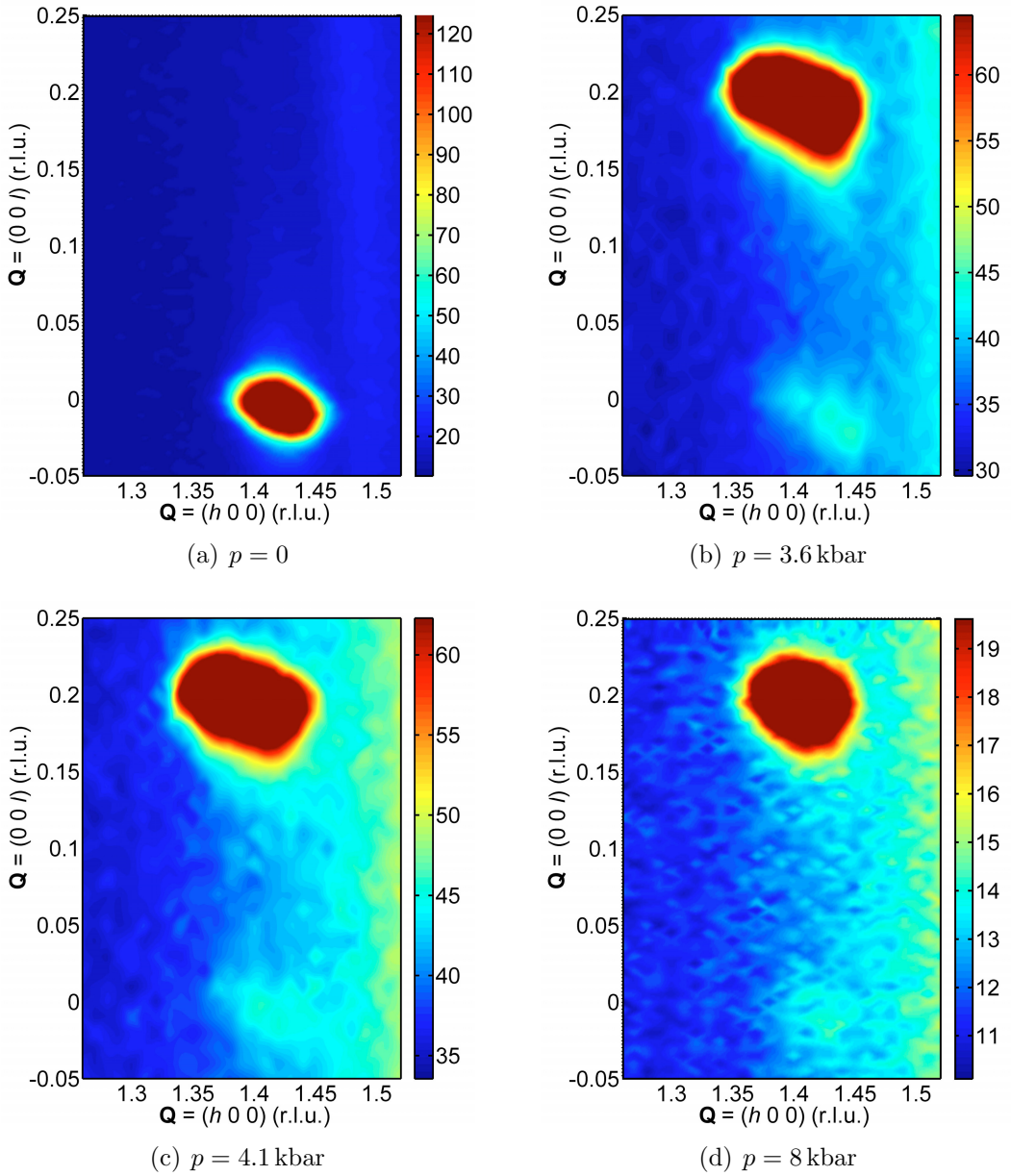

(a) $p = 0$ (b) $p = 3.6\,\mathrm{kbar}$

(c) $p = 4.1\,\mathrm{kbar}$ (d) $p = 8\,\mathrm{kbar}$

Figure 3.5: Pressure dependence of the neutron intensity (counts/500 mon., see color bar) revealing the position of the magnetic Bragg peak of $CeCu_{5.5}Au_{0.5}$ in the reciprocal (h 0 l) plane. Note that the correct aspect ratio $\frac{2\pi}{a} : \frac{2\pi}{c}$ has been taken into account. All scans were taken at the respective constant base temperature between 73 and 107 mK covering a pressure-range from zero (a) up to 8 kbar (d). The color scale was adapted to reveal weak features such as the Al-powder line in (a) and the remnant peak around $l \approx 0$ in (b, c, d) (explained in main text): Dark red color corresponds to intensity $I > I_{max}/2.1$ and dark blue color corresponds to I_{min} where $I_{max/min}$ refer to the maximal / minimal neutron intensities in the hl range shown. Therefore, strong peaks look less well defined than they actually are (compare Fig. 3.6).

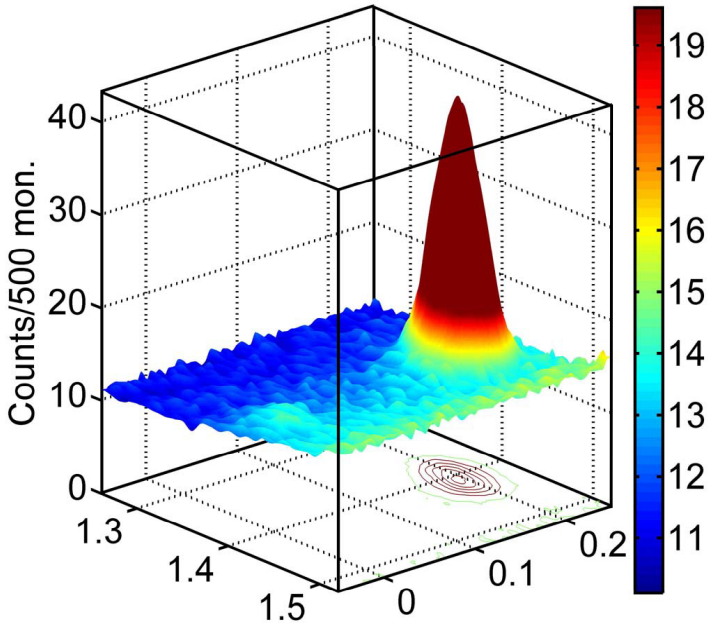

Figure 3.6: 3D plot of Fig. 3.5 (d) (neutron intensity in reciprocal (h 0 l) plane at $p = 8$ kbar) revealing a well defined Gaussian shape of the strong Bragg peak at $\mathbf{Q} = (1.405\ 0\ 0.195)$.

ordering wave vector of lower doping x are recovered. On the other hand, increasing the pressure to 4.1 kbar (c) and even 8 kbar (d) does not significantly change the Bragg position ($\mathbf{Q} = (1.405\ 0\ 0.195)$ at $p = 8$ kbar). Judging from Fig. 3.2 (b), a pressure of ~ 8 kbar should have the same effect as decreasing the Au content by about $\Delta x = 0.2$. Consequently, a small but significant increase of the l component upon increasing the pressure from $p = 3.6$ to 8 kbar would be expected, in analogy to corresponding data towards lower doping, as depicted in Fig. 3.4 (b). Moreover, a small remnant peak at the position corresponding to ambient pressure ($l \approx 0$) is present at all $p > 0$ shown. We checked the magnetic origin of this feature by heating the sample above $T_N(p)$ where it disappears completely just as the strong magnetic Bragg peak does (see Fig. 3.7). This behavior is indicative of a first-order phase transition and a separation of the sample into different domains most of which reveal magnetic order within the (h 0 l) plane ($l \neq 0$) but some along (h 0 0), too. This issue is discussed in more detail in the following.

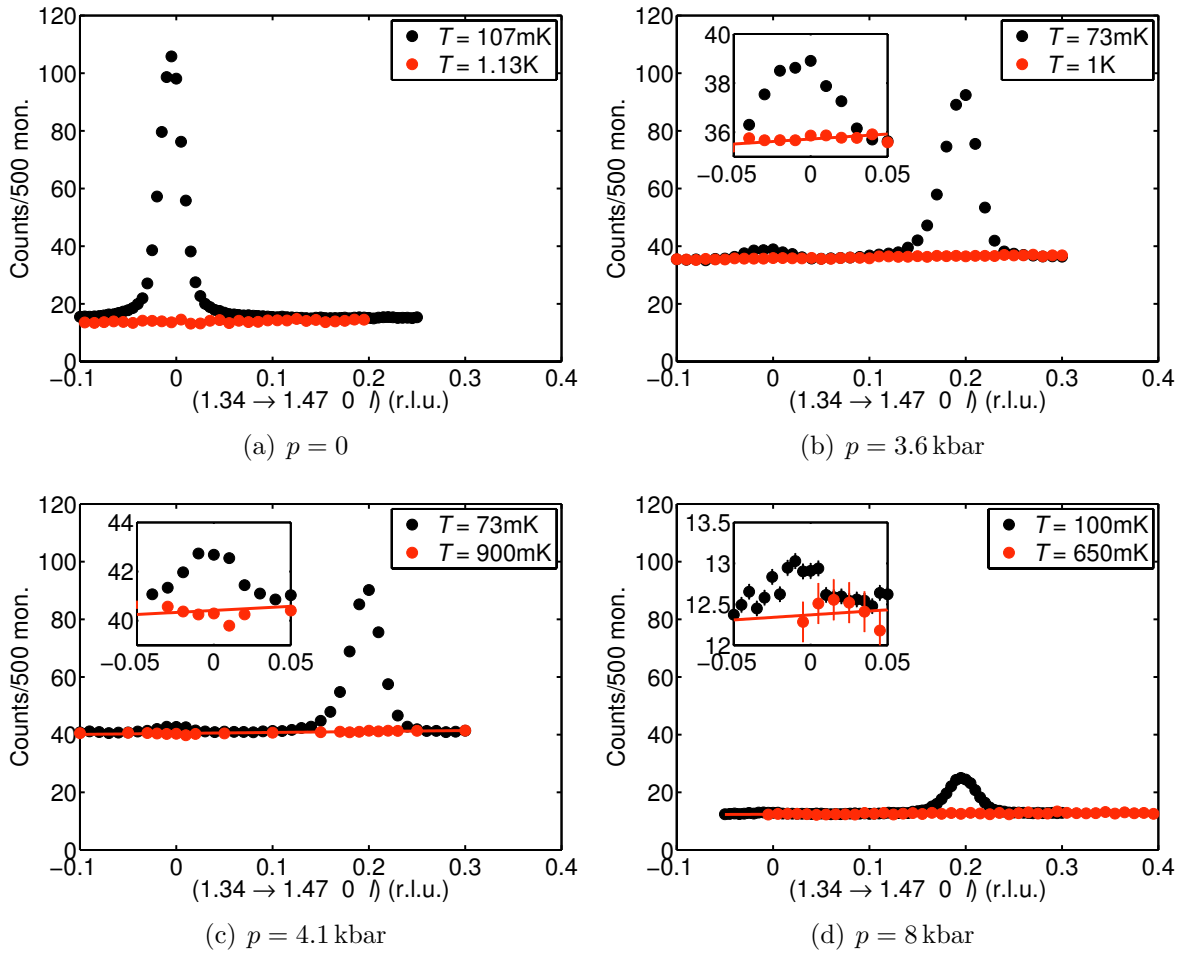

(a) $p = 0$ (b) $p = 3.6\,\mathrm{kbar}$

(c) $p = 4.1\,\mathrm{kbar}$ (d) $p = 8\,\mathrm{kbar}$

Figure 3.7: Pressure dependence of neutron intensity along $(0\ 0\ l)$ at temperatures well below (black) and considerably above (red) the respective Néel temperature $T_\mathrm{N}(p)$. Each data point corresponds to the intensity (Fig. 3.5) summed along $(h\ 0\ 0)$ for $1.34 \leq h \leq 1.47$. The solid lines are a fit to the data obtained above $T_\mathrm{N}(p)$. Insets show the range $-0.05 \leq l \leq 0.05$ on a larger scale. Note that data presented in panels (a) and (d) reveal a lower background than those shown in (b) and (c). This is most likely due to a slightly different positioning of the Cd shielding in (a, d) and (b, c), respectively: After the first experiment ($p = 0$ and 8 kbar) the Cd shielding was dismantled and mounted again at the beginning of the next run ($p = 3.6$ and 4.1 kbar).

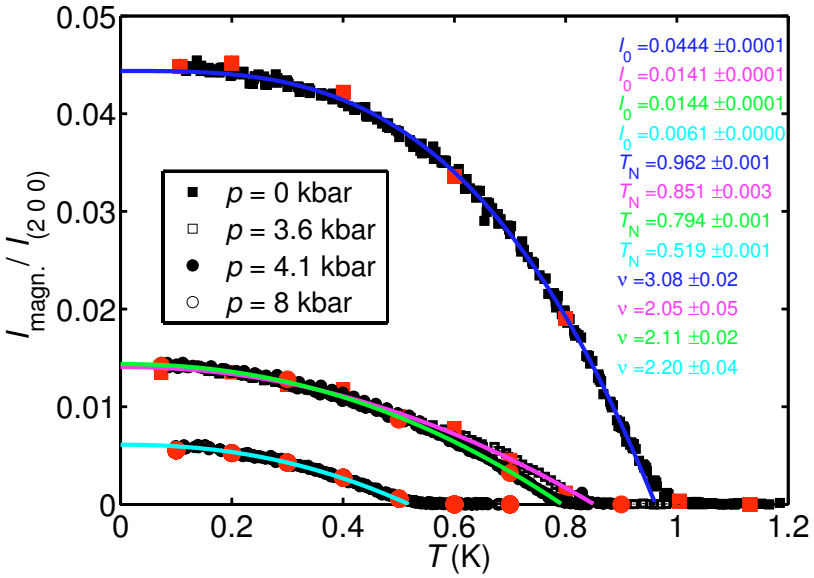

Figure 3.8: Temperature dependence of the magnetic Bragg peak intensity normalized to the nuclear (2 0 0) Bragg peak. Data shown in black were measured at the peak position extracted from a 2D Gaussian fit to data shown in Fig. 3.5. Red symbols reveal the amplitude extracted from 2D fitting several scans over the Bragg peak in (h 0 0) and (0 0 l) direction, performed at each T, and are in agreement with black symbols. Lines depict fits of the mean-field behavior given in Eq. (3.4) to the data. The parameters I_0, T_N and ν obtained from the fits are listed on the right and are colored according to the curve they refer to.

3.2.2 Temperature dependence of magnetic order at different pressures

The detailed temperature dependence of the intensity of the strong magnetic Bragg peak at all pressures is depicted in Fig. 3.8. Surprisingly, data at $p = 3.6\,\mathrm{kbar}$ and 4.1 kbar coincide at low temperatures whereas zero intensity is reached at significantly different Néel temperatures, proving the actual difference in p. This effect may be due to an intensity shift from the weak remnant peak at $l \approx 0$ to the strong peak at $l \approx 0.2$ towards increasing pressure. As a result, the intensity for $T \to 0$ happens to be the same at both pressures. In fact, Fig. 3.7 is indicative of such behavior. Additional data at even higher pressures, eventually showing that the small remnant peak disappears before the strong one does, would be needed to support this scenario. However, fitting the T dependence of the normalized magnetic intensity $I_\mathrm{magn.}/I_{(200)}$ with the mean-field behavior

$$I(T) = I_0 \cdot \left(1 - \left(\frac{T}{T_\mathrm{N}}\right)^{\nu}\right) \tag{3.4}$$

$CeCu_{5.5}Au_{0.5}$			$CeCu_{6-x}Au_x$ at $p = 0$		
p (kbar)	T_N (mK)	$\mathbf{q}_m$ (r.l.u.)	x	T_N (mK)	$\mathbf{q}_m$ (r.l.u.)
0	962	(0.588 0 − 0.003)	0.5	1022	(0.59 0 0)
3.6	851	(0.607 0 0.201)	—	—	—
4.1	794	(0.607 0 0.207)	0.4	767	(0.605 0 0.22)
8	519	(0.609 0 0.202)	0.3	511	(0.62 0 0.25)

Table 3.1: Comparison of the magnetic ordering wavevector $\mathbf{q}_m$ of $CeCu_{5.5}Au_{0.5}$ at different p (left half, values averaged over several Brillouin zones) with corresponding systems $CeCu_{6-x}Au_x$ at ambient p (right half, previous work [7, 64, 67]). Values of T_N given in the left half were extracted from fits such as described in Fig. 3.8 whereas values extracted from the linear fit in Fig. 3.2 (a) at respective x are presented in the right half. To our best knowledge, no data measured at ambient p are available matching $T_N \approx 851\,\mathrm{mK}$. Note that the uncertainty of T_N is $< 0.35\,\%$ (given exactly in Fig. 3.8) and the uncertainty of $\mathbf{q}_m$ is negligible.

yields the respective Néel temperatures $T_N(p)$ and intensities $I_0(p)$ extrapolated to $T = 0$ (uncertainties of the fit are given in Fig. 3.8). Data obtained at ambient pressure are properly described with an exponent $\nu = 3.08$ which is slightly bigger than previously found ($\nu = 2.5$) in [64]. The extraction of $T_N = 962\,\mathrm{mK}$ at $p = 0$ indicates that the actual Au content of our sample is indeed very close to $x = 0.5$, where $T_N = 1.022\,\mathrm{K}$ is expected according to the linear fit shown in Fig. 3.2 (a).

Furthermore, the reduction of $T_N(p)$ to 794 mK and 519 mK at pressures of 4.1 kbar and 8 kbar corroborates that the sample was tuned very close to $x = 0.4$ and $x = 0.3$ behavior, where the linear fit gives $T_N = 767\,\mathrm{mK}$ and $T_N = 511\,\mathrm{mK}$. In fact, the exponent $\nu = 2.20$ for $p = 8\,\mathrm{bar}$ is in good agreement with $\nu = 2$ as found for $x = 0.3$ in [16]. A comparison of $T_N(p)$ measured in this work with previous results is shown in Fig. 3.9. While previous data clearly point to a linear variation of T_N with p at all Au concentrations shown, the small number of data points obtained in this work impedes a reliable interpretation in terms of a functional form. However, assuming a linear pressure dependence extrapolating to $T_N = 0$ yields an estimate of the critical pressure $p_c \approx 20.5\,\mathrm{kbar}$ that might drive $CeCu_{5.5}Au_{0.5}$ to quantum criticality (see inset of Fig. 3.9).

3.3 Discussion

In order to determine the magnetic ordering wave vector $\mathbf{q}_m$ of $CeCu_{5.5}Au_{0.5}$ most reliably, we pinpointed the positions of related Bragg peaks not only in the vicinity of the nuclear (2 0 0) Bragg peak (Fig. 3.5) but in several other Brillouin zones, too

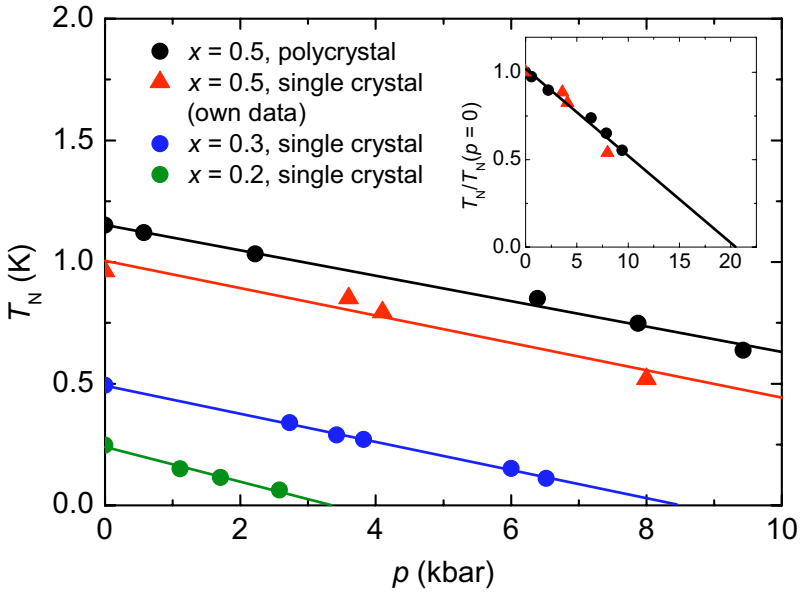

Figure 3.9: Pressure dependence of T_N for several Au concentrations x. Outer frame: Data obtained on single crystals of $CeCu_{6-x}Au_x$ with $x = 0.2, 0.3$ and polycrystalline $CeCu_{5.5}Au_{0.5}$ are adopted from [66, 52, 44]. Lines show a linear fit to the data. Note the pronounced offset between polycrystalline (black) and single crystalline (red) $CeCu_{5.5}Au_{0.5}$ that may be due to slightly higher doping of the polycrystal (its $T_N(p = 0) \approx 1.15\,K$ is shown in Fig. 3.2 (a) as black triangle to considerably exceed the linear fit). A comparison of both $x = 0.5$ systems is achieved by normalizing to the respective Néel temperature at $p = 0$ as depicted in the inset with a linear fit.

(some of which are depicted in Fig. 3.10 (a)). Resulting average values of $\mathbf{q}_m$ at different pressures are given in Tab. 3.1 in comparison to corresponding $CeCu_{6-x}Au_x$ alloys with comparable T_N at ambient pressure. Here, the accordance of our experiment at ambient pressure with previous results obtained on another single crystal of $CeCu_{5.5}Au_{0.5}$ without the pressure cell becomes even more convincing. Moreover, Fig. 3.10 (b) demonstrates that, indeed, applying $p = 3.6$ and $4.1\,kbar$ recovers the same l component of corresponding x at $p = 0$, corroborating the assumed x - p equivalence. However, no significant difference in $\mathbf{q}_m$ is revealed between $p = 3.6$ and $8\,kbar$ as opposed to a significant increase in h and l towards smaller x (see Tab. 3.1), where at $x = 0.2$ $\mathbf{q}_m = (0.625\ 0\ 0.275)$ was found in [7]. Despite the lack of data towards even higher pressures, this behavior is indicative of an intrinsic discrepancy between tuning with x and p at least on a quantitative basis. On the other hand, subtle differences are somewhat expected from the different impact of the respective tuning parameter x or p on the shape of the unit cell [44] (as explained in Sec. 3.1.1). Therefore, instead of the volume of the unit cell, the Néel-temperature being the most direct measure

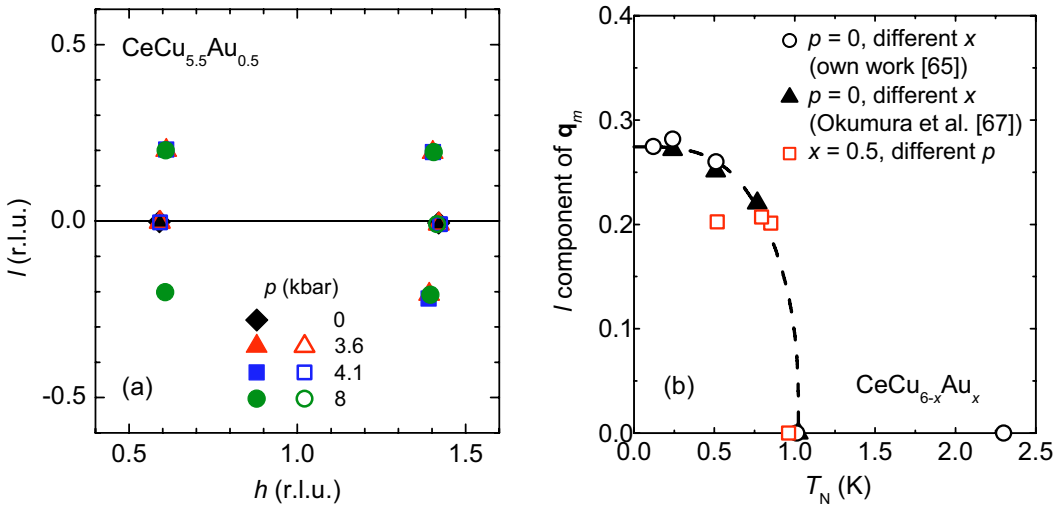

Figure 3.10: (a) Magnetic ordering peaks of $CeCu_{5.5}Au_{0.5}$ at different p in reciprocal $(h\ 0\ l)$ plane covering the same range as shown in Fig. 3.4 (a). Filled symbols refer to the strong Bragg peak, open symbols represent the weak remnant peak appearing at $p > 0$ in addition to the strong peak such as shown in Figs. 3.5 and 3.7. Note that $\mathbf{Q} = \mathbf{q}_m + \mathbf{G}$ is shown where $\mathbf{G} = (0\ 0\ 0)$ and $(2\ 0\ 0)$. (b) The l component of $\mathbf{q}_m$ vs. the Néel-temperature of several systems $CeCu_{6-x}Au_x$. The pressure dependence at $x = 0.5$ (red, values from Tab. 3.1) is shown in comparison to the concentration dependence at $p = 0$ (black, previous work). The latter were originally plotted vs. x (compare Fig. 3.4 (b)) which is mapped onto $T_N(x)$ by virtue of the linear fit shown in Fig. 3.2 (a). The dashed line is a guide to the eye.

of competing energy scales was chosen as the parameter allowing the most reasonable comparison between systems with different x at different p (Fig. 3.10 (b)).

The abrupt change of $\mathbf{q}_m$ around $T_N \approx 1\,\mathrm{K}$ being universal in respective x- or p-tuned systems $CeCu_{6-x}Au_x$ points towards a phase transition of first order. This scenario is supported by the double-peak structure that is revealed in $CeCu_{5.5}Au_{0.5}$ at $p \geq 3.6\,\mathrm{kbar}$ (i.e., $T_N \leq 851\,\mathrm{mK}$) as indicated by filled and open symbols in Fig. 3.10 (a). It might be due to a Fermi surface providing two nesting vectors at $p \geq 3.6\,\mathrm{kbar}$ of which the corresponding energy levels are populated very differently with a clear preference of $l \approx 0.2$. Another feature depicted in Fig. 3.4 (a) hints at the first-order fashion of the transition, as well: The dynamical correlations for $x = x_c = 0.1$ (as illustrated by rod-like structures) can be regarded as a precursor of incipient ordering at higher $x \leq 0.5$ because corresponding Bragg peaks are located *on* these rods. In contrast, magnetic ordering peaks for $x \geq 0.5$ are located *next* to them, ruling out any relation of the quantum critical fluctuations with magnetic order above $x = 0.5$. Finally, the behavior of the order parameter itself, i.e., the staggered moment M per Ce ion, is

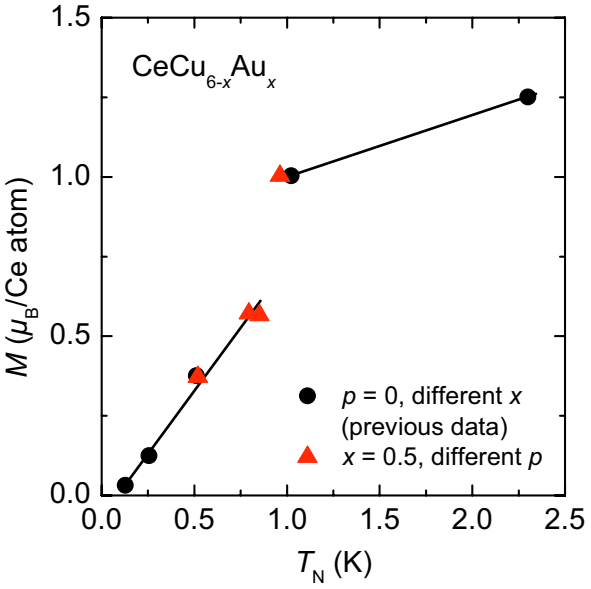

Figure 3.11: The staggered moment M per Ce ion for various systems $CeCu_{6-x}Au_x$ as a function of the respective Néel temperature T_N. Previous data (black) were adopted from [65, 6, 68], mapping $x \mapsto T_N(x)$ by virtue of the linear fit shown in Fig. 3.2 (a). Lines are a fit to data below and above T_N, respectively. Note that data shown in red reveal the relative variation of M scaled accordingly to match previous data.

indicative of a first-order transition around $T_N \approx 1\,K$. The relative variation of M with T_N can be inferred from Fig. 3.8, as $M^2 \propto I_0$. In fact, Fig. 3.11 reveals that the relative variation of M can be scaled accordingly to match absolute values found for $x = 0.3$ and $x = 0.5$ [65, 6, 68]: the staggered moment M per Ce ion increases linearly from $0.03\,\mu_B$ at $T_N = 128\,mK$ to $0.57\,\mu_B$ at $T_N = 851\,mK$ and abruptly jumps to $1\,\mu_B$ at $T_N = 962\,mK$. Clearly, the anticipated linear variation above 1 K is very preliminary and needs validation by interim data points.

3.4 Conclusion

To conclude, by applying hydrostatic pressure to $CeCu_{6-x}Au_x$ not only macroscopic properties such as the specific heat, magnetic susceptibility or electrical resistivity of correspondingly lower doping x are recovered. We succeeded in showing that a microscopic quantity, i.e., the magnetic ordering wave vector $\mathbf{q}_m$, can be tuned accordingly. Hence, the equivalence of the tuning behavior with x and p is confirmed on a microscopic level and holds even far away from the QCP at $x = 0.5$. The transition from systems ordering along $(h\ 0\ 0)$ to those where $\mathbf{q}_m$ assumes a finite l component seems to happen in a first order fashion. However, subtle differences on a quantitative basis between both tuning behaviors need further attention and should be addressed in future investigations. Ultimately, the goal must be to tune $CeCu_{5.5}Au_{0.5}$ into quantum criticality to investigate the fluctuations there. Comparing with previous neutron scattering results on $CeCu_{5.9}Au_{0.1}$ could help to gain more insight into the mechanisms that drive the quantum phase transition.

Chapter 4

Phonon anomalies in the cuprate superconductors $La_{2-x}Sr_xCuO_4$ and $HgBa_2CuO_{4+\delta}$

4.1 Introduction

In 1986, Bednorz and Müller discovered that $La_{1.85}Ba_{0.15}CuO_4$ becomes superconducting below the critical temperature $T_c = 38\,\mathrm{K}$. Only a few months later, the related compound $YBa_2Cu_3O_{7-\delta}$ was found to have an even higher T_c of 93 K, ushering in the era of 'high temperature superconductivity' (HTSC). Since these cuprate superconductors operate at temperatures easily reachable by cooling with liquid nitrogen (LN_2, boiling point 77 K), emerging consequences for technological applications were quickly recognized and led to the awarding of the Nobel Prize in 1987 to Bednorz and Müller. In 2008, another class of HTSC, so-called Fe-based pnictides, was discovered. However, the highest $T_c \approx 135\,\mathrm{K}$ (at ambient pressure) known to date has been demonstrated for the members of the Hg-based family of the cuprates ($HgBa_2Ca_2Cu_3O_{8+\delta}$). Therefore, further investigation of the cuprates is of key interest since it might help to elucidate the still unknown mechanism leading to superconductivity at elevated temperatures. A proper understanding of this mechanism might possibly enable one to influence specific parameters leading to even higher T_c values.

Cuprate HTSC crystallize in the perovskite structure revealing weakly coupled copper-oxide (CuO_2) layers. Neighboring layers typically containing ions such as La, Ba or Sr stabilize the structure and act as a charge reservoir doping electrons or holes into the copper-oxide planes. In the following, only hole-doped cuprates are considered of which the generic phase diagram is shown in Fig. 4.1. Undoped parent compounds are Mott-Hubbard insulators with half-filled (one electron per state) Cu orbitals resulting in long-range antiferromagnetism below the Néel temperature T_N. Low doping quickly

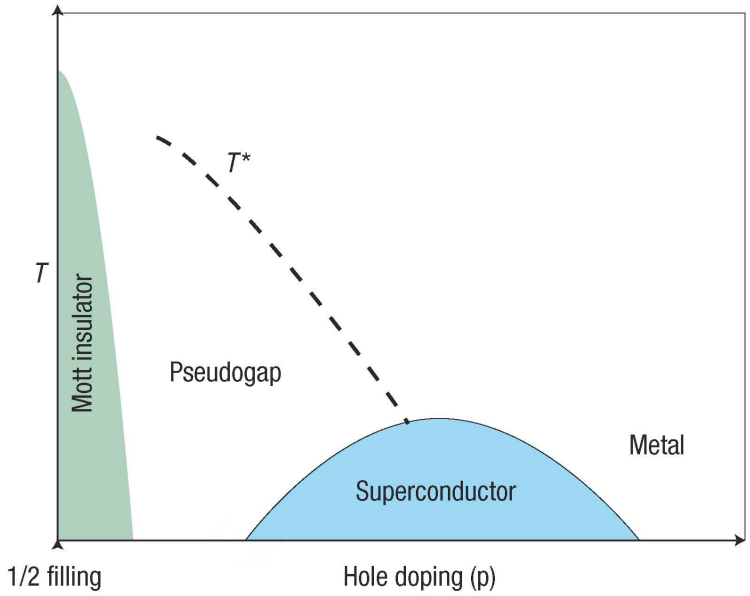

Figure 4.1: Generic phase diagram of hole-doped cuprate superconductors as adopted from [69].

decreases T_N and leads to a metallic state with very unusual properties, in particular a pseudogap in the electronic density of states persisting up to T^* and mimicking the true gap in the superconducting state at higher doping [69]. Finally, a metallic phase is found in the overdoped regime. Since conventional superconductivity is mediated by phonons, their role in the mechanism of HTSC has been considered very early on. However, one could not think of electron-phonon coupling with a strength leading to transition temperatures near 100 K. Therefore, phonons were discarded and the main focus of research was on magnetic mechanisms. The discovery of anomalous behavior of certain Cu-O bond-stretching vibrations, somehow related to superconductivity, led to a renewed interest in phonon-mediated coupling and triggered a systematic study of phonons in many cuprate compounds such as $La_{2-x}Sr_xCuO_4$ (LSCO), $YBa_2Cu_3O_{7-\delta}$ (YBCO), $HgBa_2CuO_{4+\delta}$ (Hg1201) and electron-doped $Nd_{2-x}Ce_xCuO_4$ (NCCO) [9, 10]. In this chapter, measurements on LSCO and Hg1201 focusing on this phonon anomaly are presented.

4.2 $La_{2-x}Sr_xCuO_4$

The unit cell of LSCO in the high-temperature tetragonal (HTT) phase is depicted in Fig. 4.2 (a). It contains two CuO_2 layers that are stacked in a body-centered fashion. Below the structural phase transition temperature $T_s = 550$ K each CuO_6 octahedron

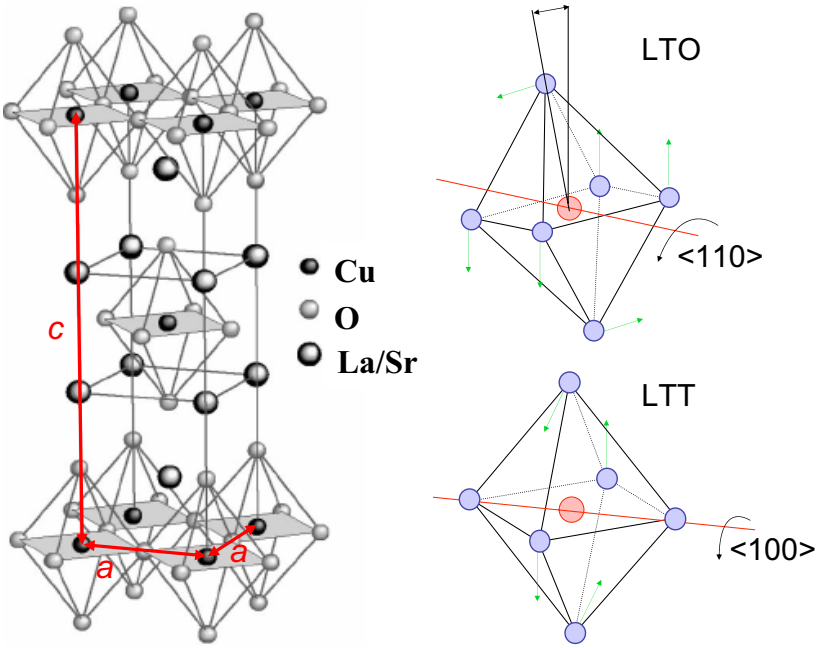

Figure 4.2: (a) Unit cell of LSCO in the HTT phase with the lattice constants $a = 3.8$ Å and $c = 13.1$ Å containing 14 atoms (two Cu, eight O and four La/Sr). (b) Upper panel: Tilt of the CuO_6-octahedra around the crystallographic $\langle 1\ 1\ 0 \rangle$ axis leading to the LTO phase. Lower panel: A tilt around $\langle 1\ 0\ 0 \rangle$ results in the LTT phase that is discussed later in this section.

rotates about a $\langle 1\ 1\ 0 \rangle$ axis (see upper panel of Fig. 4.2 (b)), where neighboring octahedra within a plane rotate in opposite directions. This results in a doubling of the unit-cell volume and a change of the crystal symmetry to the low-temperature orthorhombic (LTO) phase. In order to avoid confusion, the notation of the HTT phase is used in the following. In the undoped system La_2CuO_4 (LCO), Cu spins order antiferromagnically below $T_N \approx 325$ K [70] by virtue of superexchange mediated by O atoms. Upon hole-doping with Sr, T_N is quickly suppressed and vanishes at $x = 0.02$ [71]. Superconductivity is found for $0.06 \leq x < 0.3$, where optimal doping of $x = 0.15$ results in $T_c = 35$ K [72].

Anomalous phonon behavior

Previous experiments revealed an anomalous behavior of the longitudinal plane-polarized Cu-O bond-stretching vibration in the $\langle 1\ 0\ 0 \rangle$ direction. Among all phonon branches of Δ_1-symmetry in LSCO, it is the one with the highest energy. Since only high energy

branches are considered in the following discussion, this special vibration will simply be referred to as the 'Δ_1-branch'. The displacement pattern of its corresponding zone boundary[1] mode is shown in Fig. 4.3 (b). It is usually called the 'half-breathing' mode in comparison to the 'breathing' mode that is illustrated in (c). The latter is associated with another high energy longitudinal vibration propagating along $\langle 1\ 1\ 0\rangle$ (Σ_1-symmetry).

The dispersion and linewidth (FWHM) of the Δ_1-branch as extracted from E scans around (5 0 0) at different Sr-doping levels x [73] are exhibited in Fig. 4.3 (a), that is indicative of four features:

(1) The softening towards the zone boundary that is enhanced with increasing doping and results is a cosine-like downward dispersion.

(2) The gradual broadening of the phonon linewidth towards the zone boundary.

(3) The deviation from a simple cosine dispersion in the optimally doped system.

(4) The pronounced maximum of the phonon linewidth around $\mathbf{q} = (0.3\ 0\ 0)$ in the optimally doped system.

Phenomenological models developed for ionic insulators, in particular the shell model[2], give a decent description of nearly all phonon branches in LCO [74]. Implementing a special term accounting for the screening by free charge carriers (holes) even yields a proper description of most of the phonon branches in underdoped LSCO. However, these models predict a rather flat dispersion of the Δ_1-branch that is in contrast to the pronounced frequency renormalization (1) observed in the measurements. Fig. 4.3 (d) demonstrates that the softening at the zone center cannot be related to superconductivity since it continuously increases with doping through the superconducting regime and becomes most pronounced for overdoped, non-superconducting $La_{1.7}Sr_{0.3}CuO_4$. (The same behavior is found for the breathing mode as indicated by open symbols.) Consequently, the cosine dispersion (1) is considered the 'normal' behavior of that phonon branch accompanied by a gradual broadening of the linewidth towards the zone boundary (2) that is equally present for $x = 0.15$ and $x = 0.3$.

On the other hand, (3) and (4) are only present for optimally doped LSCO but here also above T_c [72]. This is what makes (3) and (4) the true 'anomalous' behavior strongly suggesting a relation to superconductivity.

[1] Due to the body-centered symmetry of the unit cell, group theoretical Γ-points in reciprocal space are characterized by $\mathbf{G} = (h\ k\ l)$ where $h + k + l$ be even. As an example, (5 0 1) is a Γ-point as opposed to (5 0 0) being a Z-point. However, when measuring the dispersion of high-energy Cu-O plane-polarized vibrations *any* $\mathbf{G} = (h\ k\ l)$ (with $h, k, l \in \mathbb{Z}$) can be considered a true 'zone center' in the sense that all atoms move in phase. Correspondingly, the 'zone boundary' is found at $\pm\langle 0.5\ 0\ 0\rangle$ away from the respective zone center. This is a consequence of the weak interaction between neighboring CuO_2 layers and cannot be generalized.

[2] A detailed description of such a model is given in Sec. 4.2.1.1.

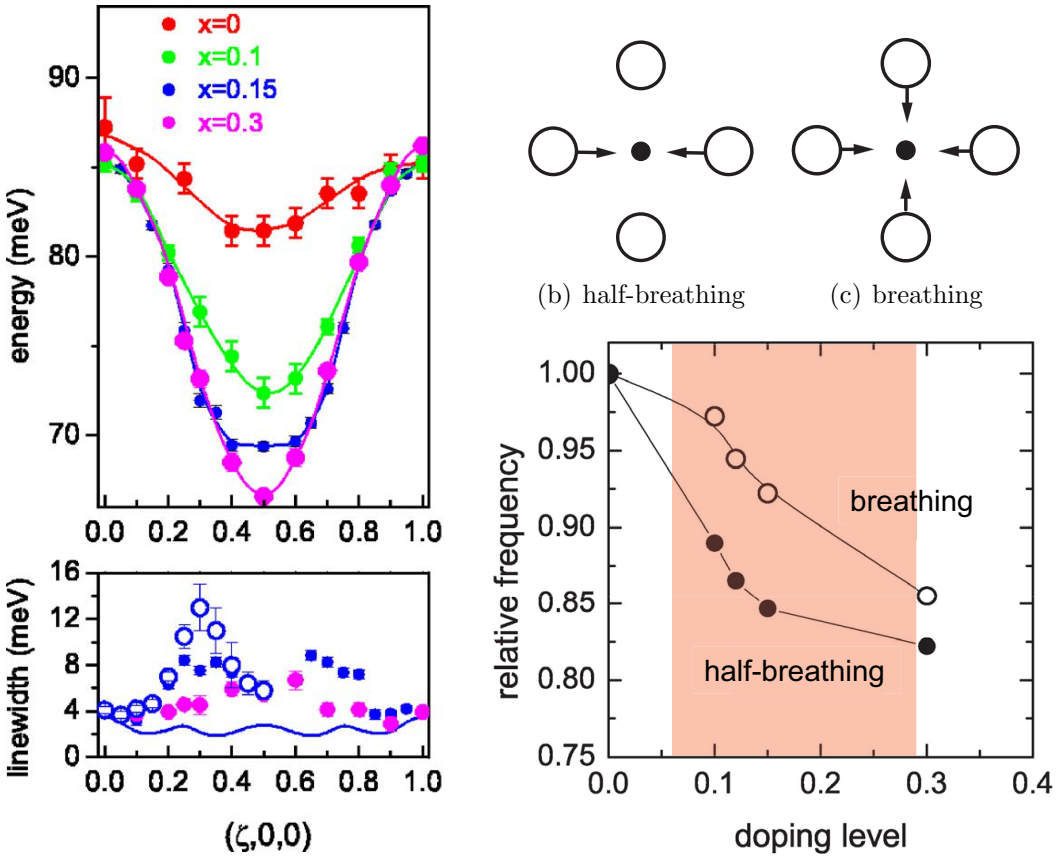

(a) Dispersion / FWHM of Δ_1-branch.

(b) half-breathing

(c) breathing

(d) Softening at zone boundary.

Figure 4.3: Anomalous behavior of longitudinal phonon branches at a temperature of 10 K as adopted from [73]. (a) Upper panel: Measured dispersion of the Δ_1-branch for various doping levels x in $La_{2-x}Sr_xCuO_4$. Lines are a guide to the eye. Lower panel: Data points depict the linewidth (FWHM) of phonon peaks, the line shows the experimental resolution. Open and closed symbols shown in blue correspond to two different data sets obtained on $La_{1.85}Sr_{0.15}CuO_4$. (b, c) Displacement patterns of zone-boundary bond-stretching modes in [1 0 0] (b) and [1 1 0] (c) direction. Circles and solid points represent oxygen and copper atoms, respectively. Only the displacements in the Cu-O layers are shown, other displacements are small for these modes. (d) Relative frequency renormalization of the breathing and half-breathing mode towards increasing Sr-doping in LSCO. The superconducting regime is marked by the red area.

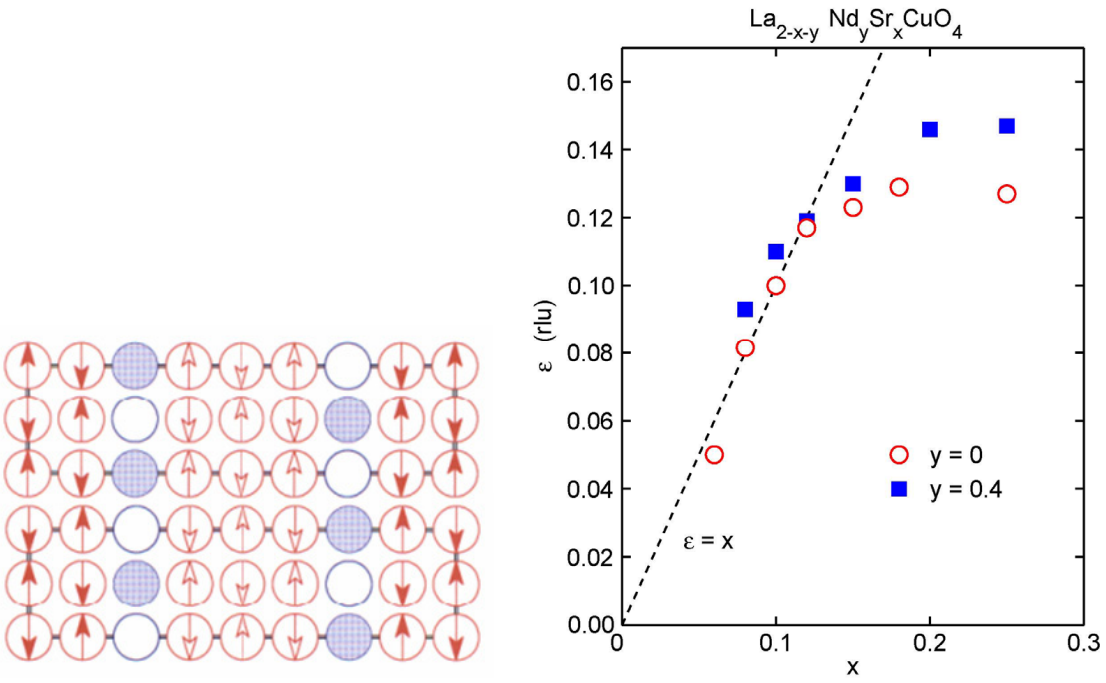

Figure 4.4: (Left panel) Schematic plot of two magnetic unit cells illustrating spin-charge segregation in the form of stripes within the CuO_2 planes for the case of $\frac{1}{8}$ doping. Only Cu sites are represented. Magnetic moments are indicated by arrows, different shading distinguishes antiphase domains. Blue filled circles correspond to holes. Note that the charge order indicated within the charged stripes has never been observed and simply illustrates the hole per Cu ratio of $\frac{1}{2}$. The plot was adopted from [75]. (Right panel) Variation of the magnetic incommensurability ε with x in $La_{2-x-y}Nd_ySr_xCuO_4$ as adopted from [76]. Data shown as open red circles correspond to $y = 0$ and are extracted from measurements at $E \approx 3\,\text{meV}$ and $T \approx T_c$ [77]. Filled blue squares correspond to $y = 0.4$ from [78].

Relation of phonon anomaly to 'stripes'

A similar effect was found in related compounds with doping levels about $\frac{1}{8}$ such as $La_{1.6-x}Nd_{0.4}Sr_xCuO_4$ (LNSCO) with $x = 0.12$ [79] and $La_{2-x}Ba_xCuO_4$ (LBCO) with $x = 0.125$ [80] where superconductivity is destroyed by emerging static stripe order that is illustrated in Fig. 4.4 (left panel): Within the Cu-O planes, antiferromagnetic 'stripes' of copper spins are separated by periodically spaced domain walls to which the holes segregate[3]. In these compounds, the structural phase transition to the low-

[3]It has been argued that charge segregation may result from a competition between the kinetic energy of charge carriers and the antiferromagnetic superexchange between magnetic moments on neighboring Cu atoms [81, 82, 83].

temperature tetragonal (LTT) phase (see Fig. 4.2) provides a corrugation potential pinning the stripes and thereby destroying superconductivity. Neutron scattering from static stripe order results in four incommensurate elastic magnetic peaks at the spin ordering wave vector $\mathbf{q}_{so} = \mathbf{G}_{\mathrm{AF}} + \langle \varepsilon\ 0\ 0 \rangle$ where $\mathbf{G}_{\mathrm{AF}} = (\frac{1}{2}\ \frac{1}{2}\ 0)$ characterizes the commensurate long-range antiferromagnetic order [75]. ε increases with increasing doping x and seems to saturate around $\varepsilon \approx 0.145$ as shown for LNSCO by filled blue squares in Fig. 4.4 (right panel). Charge inhomogeneity with a periodic modulation is expected to affect interatomic Coulomb forces which in turn can have decisive influence on the behavior of particular lattice vibrations: The polarization pattern of the Δ_1-branch matches the lattice deformation induced by the charge inhomogeneity and, consequently, a softening and strong broadening in close vicinity to the corresponding charge ordering wave vector $\mathbf{q}_{co} = \langle 2\varepsilon\ 0\ 0 \rangle$ is expected according to [84]. Indeed, a pronounced dip in the dispersion and a concurrent maximum of the phonon linewidth are observed in $La_{1.48}Nd_{0.4}Sr_{0.12}CuO_4$ at around $\mathbf{q} = (0.275\ 0\ 0)$ [9, 85]. This is clear evidence of a strong coupling of this phonon mode to charge carriers substantially reducing the phonon lifetime.

In LSCO, incommensurate spin-density-wave order along $\langle 1\ 1\ 0 \rangle$ is found in the spin-glass phase for $0.02 < x < 0.06$ [86]. However, corresponding charge-density-wave order has not been observed [87]. In the superconducting regime above $x = 0.06$, peaks indicating dynamic magnetic correlations are found along $\langle 1\ 0\ 0 \rangle$ at $\mathbf{q}_{so}$ with ε increasing towards increasing doping and saturating around $\varepsilon \approx \frac{1}{8}$ as shown by open red circles in Fig. 4.4 (right panel). These dynamic correlations are interpreted as a precursor effect of static stripe order where the remaining dynamic (fluctuating) stripes possibly compete with superconductivity. The comparison of both systems with $y = 0$ and $y = 0.4$ in Fig. 4.4 reveals differences in ε for any given x that may be associated with a changing hole density of the charge stripes as they are pinned by the anisotropic lattice potential of the LTT phase in LNSCO [76].

Finally, the phonon anomalies (3) and (4) observed in optimally doped LSCO may be regarded as the signature of dynamic stripes manifesting themselves in the charge channel. However, a systematic study of this effect towards lower doping x is needed to truly establish a correspondence between the magnetic and the charge channel. In this chapter, neutron scattering results obtained on non-superconducting $La_{1.95}Sr_{0.05}CuO_4$ are presented along with an improved analysis of previous data revealing the role of resolution-based contributions.

4.2.1 Experimental results

The experiments were performed on the triple-axis spectrometer 1T operated at the 'Laboratoire Léon Brillouin' of the CEA, Saclay (France), using doubly focusing monochromator (Cu220) and analyzer (PG002) crystals. Cu220 was used to achieve high

resolution[4]. A closed cycle ^{4}He refrigerator provided access to temperatures between 3.5 K and 600 K. Single crystals[5] of $La_{1.95}Sr_{0.05}CuO_4$ with a volume of about 1 cm^3 and a respective mosaic spread of 1° and 2° were measured with the experimental scattering plane spanned by reciprocal [1 0 0] and [0 1 0] axes. In addition, a finite l component could be accessed by tilting the goniometer at the sample table for a few degrees. We focused on scans around (5 0 l) with $l = 0, -1, -2, -3$ to maximize the inelastic structure factor (Eq. (1.27)) of the Δ_1-branch and to avoid spurious contamination. The instrument was operated with fixed $k_f = 2.662\,\text{Å}^{-1}$ and a PG filter[6] placed between the sample and the analyzer to suppress higher order contamination.

4.2.1.1 Simulating lattice dynamics using a shell model

The derivation of atomic force constants from first principles is not yet possible for weakly doped cuprate superconductors such as $La_{1.95}Sr_{0.05}CuO_4$.[7] Instead, phenomenological models like the shell model [88] can be used to describe the lattice dynamical properties of these complex systems.

The shell model originates from the rigid-ion model for ionic insulators in which short-range repulsive forces and the Coulomb interaction between the ions are taken into account. In the shell model, atomic polarizability is introduced by isotropically coupling a spherical electronic shell to its rigid ion core by a spring (intra-atomic coupling). Neighboring electronic shells are coupled to each other by another spring (inter-atomic coupling). Metallicity arising by doping the parent compound with holes is implemented by 'screening-parameters' that account for the reduced range of the Coulomb force due to the screening effect of conduction electrons. Finally, the resulting set of parameters is adapted to properly describe experimentally determined phonon dispersions in all major crystallographic directions.

However, at finite doping the model predicts a rather flat dispersion of the Δ_1-branch that is not in agreement with the experimental observation. An additional term has to be accommodated in the model in order to describe the 'normal' cosine-like dispersion of that phonon branch ('normal' in the sense of not being related to superconductivity). It should be noted that this term has not been derived in a proper way and hence is entirely phenomenological. Yet, its influence on other branches is extremely small. Furthermore, it is important to note the harmonic limit of the shell model where higher-order effects such as phonon-phonon or electron-phonon coupling

[4]The actual calculated resolution is included in the shell model predictions as presented in the following.

[5]Samples were provided by the 'Institute for Material Research' of the Tohoku University, Sendai (Japan).

[6]See Fig. 1.7 in chapter 1.3 for explanation.

[7]To some extent, the density-functional theory (DFT) is appropriate for describing stoichiometric and metallic cuprates such as $YBa_2Cu_3O_7$. However, calculations for weakly doped LSCO yield results expected for optimally or overdoped LSCO.

are neglected. Consequently, it does not account for the finite lifetime of phonons that would result in a non-vanishing *intrinsic* linewidth of phonon peaks.

In this work, the program package '`genax`' as developed by W. Reichardt and S. L. Chaplot [74] is used to simulate E scans tracing the Δ_1-branch through the Brillouin zone. A special advantage of `genax` is its capability of considering the experimental resolution: Parameters such as the final neutron energy, the monochromator and analyzer setting, horizontal and vertical collimation and the mosaic spread of the sample, the monochromator and the analyzer crystal are taken into account to calculate the resolution-based line shape of phonon peaks. More specifically, `genax` calculates the 4D convolution of the modeled scattering function S and the resolution function R as shown in Eq. (1.49) where $S(\mathbf{Q},\omega)$ is given by Eq. (1.29).

As described in Sec. 1.2.1.2, the scalar product $(\mathbf{Q}\cdot\xi)$ in the dynamic structure factor $\mathcal{F}(\mathbf{Q})$ (Eq. (1.27)) in principal allows to distinguish between longitudinal and transverse phonon modes which is often referred to as the 'selection rule'. Due to the high symmetry of the plane-polarized Cu-O vibrations one can focus on the Δ_1-branch by choosing $\mathbf{Q}$ along [1 0 0]: All oxygen atoms vibrate along [1 0 0] (compare Fig. 4.3 (b)) and hence $\mathbf{Q}\cdot\xi_{\Delta_1}\neq 0$ as opposed to the corresponding transverse branch in the [1 0 0] direction (Δ_3-symmetry) where $\mathbf{Q}\cdot\xi_{\Delta_3}\approx 0$. Assuming the hypothetical case of perfect instrumental resolution (i.e., a vanishingly small resolution ellipsoid), solely the Δ_1-branch would contribute to E scans at $\mathbf{q}=(h\ 0\ 0)$ where the signal from the Δ_3-branch would be negligible.

However, the situation becomes more complicated in a real experiment. The final resolution of the instrument does not only affect the line shape of the phonon under investigation but gives rise to sometimes unexpected features like additional peaks, too. As it turned out, it is crucial to consider the evolution of phonon branches away from the high-symmetry [1 0 0] direction as illustrated in Fig. 4.5. The branch shown in red is purely transverse along $(h\ 0\ 0)$, i.e., for $k=0$, only. In the off-symmetry direction at $(h\ k\ 0)$ with $|k|>0$ it assumes a small but significant longitudinal component, hence a non-negligible dynamic structure factor and the selection rule does not strictly apply any more. Scanning the energy, the resolution ellipsoid sweeps through the dispersion of both branches: Centered at $(h\ 0\ 0)$ the ellipsoid picks up intensity not only from the interesting Δ_1-branch (blue) but also from the non-negligible longitudinal component of the red branch in the transverse direction at finite k. As a result, the shell model calculations predict a two-peak structure around the energy range of the Δ_1-branch that is depicted in Fig. 4.6 (note the color code: peaks are colored according to the respective phonon branch (Fig. 4.5) they are related to). All peaks reveal a Gaussian line shape.

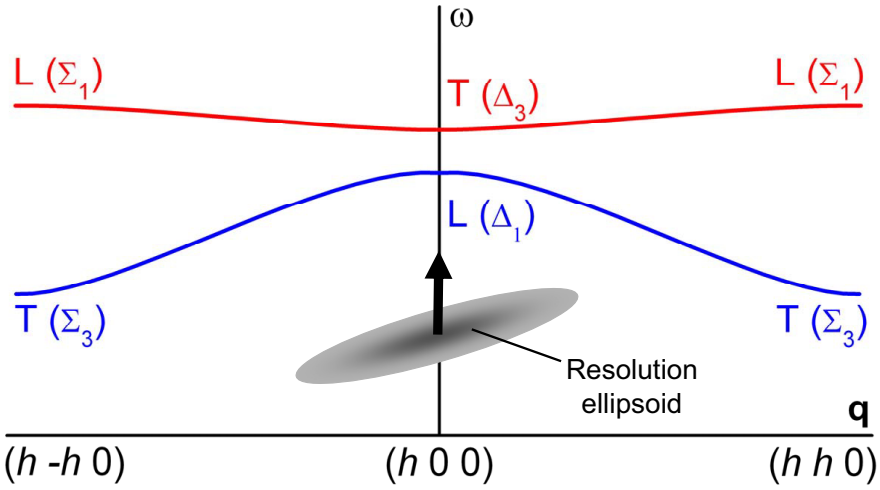

Figure 4.5: Schematic illustration of two phonon branches in lightly-doped LSCO in the energy range of interest, connecting the high-symmetry [1 0 0] direction at finite h along an off-symmetry direction with another high-symmetry [1 1 0] direction. (Note that only plane polarized Cu-O bond-stretching vibrations are considered.)
Along (h 0 0) (out of paper plane) the longitudinal (L) Δ_1-branch disperses downwards as shown in Fig. 4.3 (a). Since the Lyddane-Sachs-Teller splitting can be neglected already at small doping, the Δ_1-branch coincides with the corresponding transverse (T) branch (Δ_3-symmetry) towards $h \rightarrow 0$. The latter reveals a flat dispersion along (h 0 0) as demonstrated in Fig. 6 of [9]. Here, the situation at some finite h is shown where the Δ_1-branch lies considerably below the Δ_3-branch. Their connection to other phonon branches along (0 k 0) is illustrated by the red and blue line: The Δ_3-branch connects to a longitudinal vibration in the [1 1 0] direction (Σ_1-symmetry) of which the corresponding zone boundary mode is referred to as 'breathing mode' (compare Fig. 4.3 (c)). The Δ_1-branch in turn connects to a transverse vibration in the [1 1 0] direction (Σ_3-symmetry) the zone boundary mode of which is called 'quadrupolar mode' (see Fig. 4 of [73]). The slight upturn (downturn) of the red (blue) dispersion away from (h 0 0) illustrates the relative behavior of the connecting branches, respectively, that are discussed in detail in [73]. At a given h, the branches are purely transverse or longitudinal for $k = 0$ and $k = h$, i.e., (h 0 0) or (h h 0), only. At (h k 0) with $0 < |k| < h$ the modes mix.

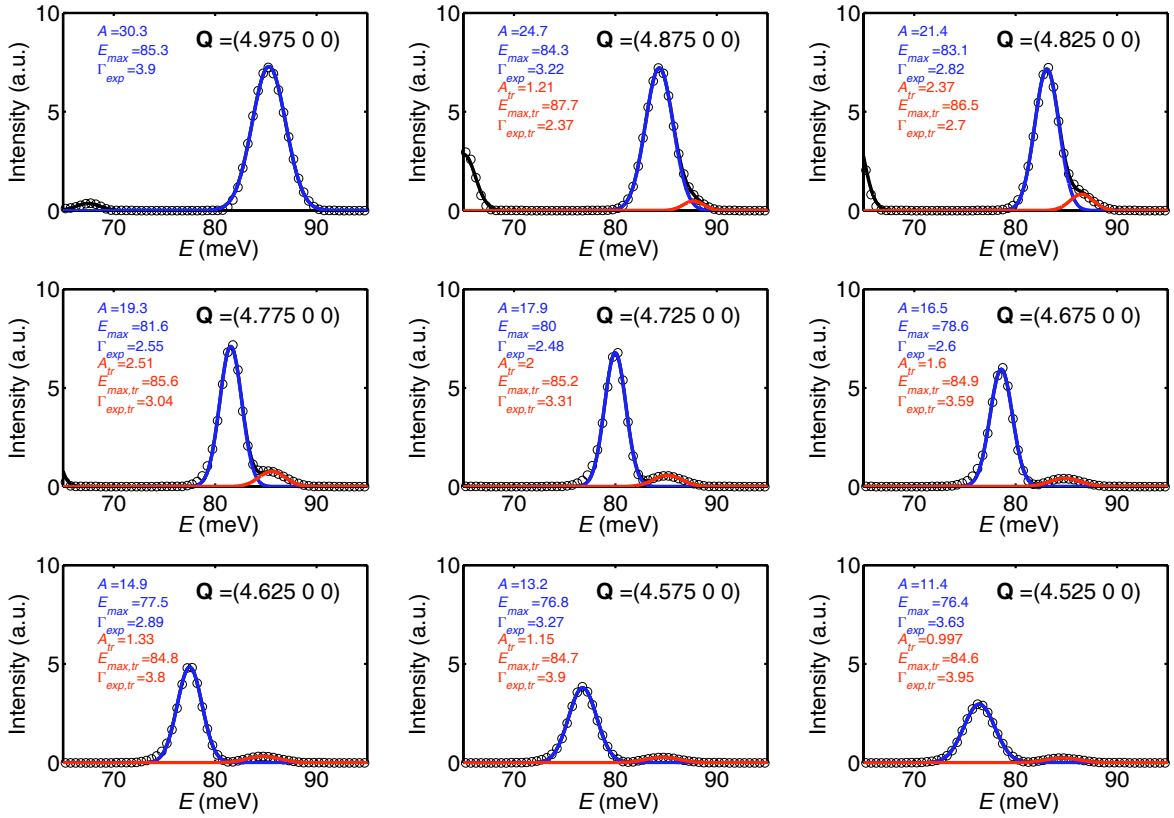

Figure 4.6: Calculations using `genax` on non-superconducting $La_{1.95}Sr_{0.05}CuO_4$ with a mosaic spread of 2° at $T = 12\,\mathrm{K}$. Simulated E scans are depicted covering the range from 65 to 95 meV at several $\mathbf{Q} = (5-q\ 0\ 0)$ from close to the zone center (upper left panel) towards the zone boundary (lower right panel). Lines show Gaussian fits to the data: The resolution-based transverse contribution appears as subtle high-energy peak (red) in addition to the peak that is related to the bond-stretching Δ_1-branch (blue). Another phonon of Δ_1-symmetry (the longitudinal bond-bending mode) shows up in some panels at considerably lower energies and is therefore without influence on the bond-stretching Δ_1-branch. The sum of all contributions is depicted as black line.

4.2.1.2 Fit of data obtained on $La_{1.95}Sr_{0.05}CuO_4$

The E scans measured at (q 0 0) corresponding to the simulations are exhibited in Fig. 4.7. A finite l component of $\mathbf{Q}$ was chosen to maximize the inelastic structure factor and to avoid spurious contamination. The vertical (out of scattering plane) resolution of a TAS is usually much worse than the horizontal (in plane) resolution. Consequently, we chose the reciprocal [1 0 0] and [0 1 0] axes to span the experimental scattering plane to minimize the effect of the resolution-based transverse contribution. Having [0 1 0] in the vertical direction instead would enlarge the resolution ellipsoid along [0 1 0] and thereby enhance the transverse contribution (see Fig. 4.5). Unfortunately, `genax` does not allow calculations out of the scattering plane at some finite l (which we achieved experimentally by tilting the goniometer angle). Hence, the simulation had to be performed in the "wrong" Brillouin zone with $l = 0$ which has minor influence on the dynamic structure factor: Although the ratio between the areas of the blue and the red peak in Fig. 4.6 is correct, the $\mathbf{Q}$ dependence of the sum of both areas is not quite correct. In order to allow for a quantitative comparison of the simulations with the experiment, we calculated the dynamic structure factor corresponding to the experimental Brillouin zone and scaled the Gaussian fits accordingly[8].

Let $G_{\Delta_1}(E - E_{max}; A, \Gamma_{exp})$ denote the simulated Gaussian peak associated with the bond-stretching Δ_1-branch (blue) that is centered around E_{max} with the area A and the resolution-based calculated linewidth (FWHM) Γ_{exp}. G_{tr} denotes the simulated Gaussian peak related to the transverse contribution (red). Both Gaussians are convoluted with normalized Lorentzians $L_{\Delta_1}(E; \Gamma_{int})$ and $L_{tr}(E; \Gamma_{int,tr})$, respectively, accounting for the intrinsic linewidths Γ_{int} and $\Gamma_{int,tr}$ to fit the measured intensity $I(E_0)$:

$$\begin{aligned} I(E_0) \stackrel{!}{=} & f \cdot \int dE\, G_{\Delta_1}(E - E_{max}; A, \Gamma_{exp}) \cdot L_{\Delta_1}(E - E_0; \Gamma_{int}) + \\ + & f \cdot \int dE\, G_{tr}(E - E_{max,tr}; A_{tr}, \Gamma_{exp,tr}) \cdot L_{tr}(E - E_0; \Gamma_{int,tr}) + \\ + & s \cdot E_0 + o\,, \end{aligned} \tag{4.1}$$

where the slope (s) and the offset (o) characterize the linear background due to multi-phonon and incoherent scattering. An overall factor f scales the simulated spectra to match the measured intensity. This factor as well as the linear slope and $\Gamma_{int,tr}$ are fitted across all $\mathbf{Q}$ simultaneously (note that they are the same at every $\mathbf{Q}$). The offset, Γ_{int} and E_{max} are varied at every $\mathbf{Q}$, respectively, while fixing $E_{max,tr}$ to the initial (calculated) value. The area A of the Δ_1-peak is allowed to deviate about 25 % from the calculated value (given as dev_A in each panel) in order to compensate for imperfections of the model, A_{tr} is fixed.

The analysis clearly reveals the role of the transverse contribution, most prominently

[8] The $\mathbf{Q}$ dependence of the Debeye-Waller factor was taken into account.

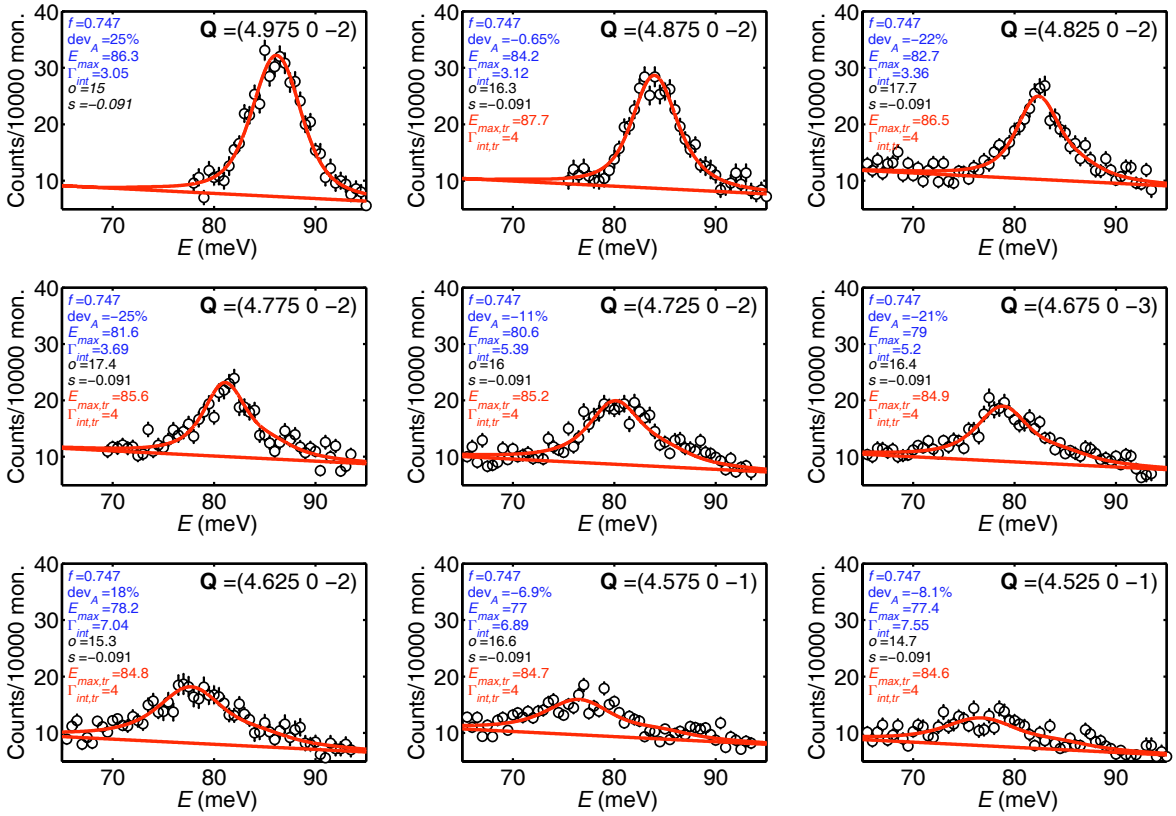

Figure 4.7: E scans on $La_{1.95}Sr_{0.05}CuO_4$ with a mosaic spread of 2° at $T = 12\,K$ tracing the Δ_1-branch from close to the zone center (upper left panel) towards close to the zone boundary (lower right panel). Solid lines show fits to data according to Eq. (4.1).

as the small high-energy shoulder of the Δ_1-peak. This contribution could have easily been misinterpreted as an exotic but intrinsic effect or as originating from some misoriented domain or pure statistics, thus corrupting the analysis.

The same analysis was performed on other sets of scans obtained on another sample of $La_{1.95}Sr_{0.05}CuO_4$ at $T = 3\,K$ and 500 K. Also, previous data taken on $La_{1.93}Sr_{0.07}CuO_4$ at about 12 K [89] were analyzed in the same fashion. These samples had a smaller mosaic spread of only 1° which somewhat improves the resolution and hence reduces the resolution-based transverse contribution (not shown). Respective extracted dispersions and intrinsic linewidths are presented in the following.

4.2.2 Discussion

The dispersion and concurrent intrinsic linewidth of the Δ_1-branch in LSCO for several Sr-doping ratios x are depicted in Fig. 4.8 in comparison to $La_{1.48}Nd_{0.4}Sr_{0.12}CuO_4$. The

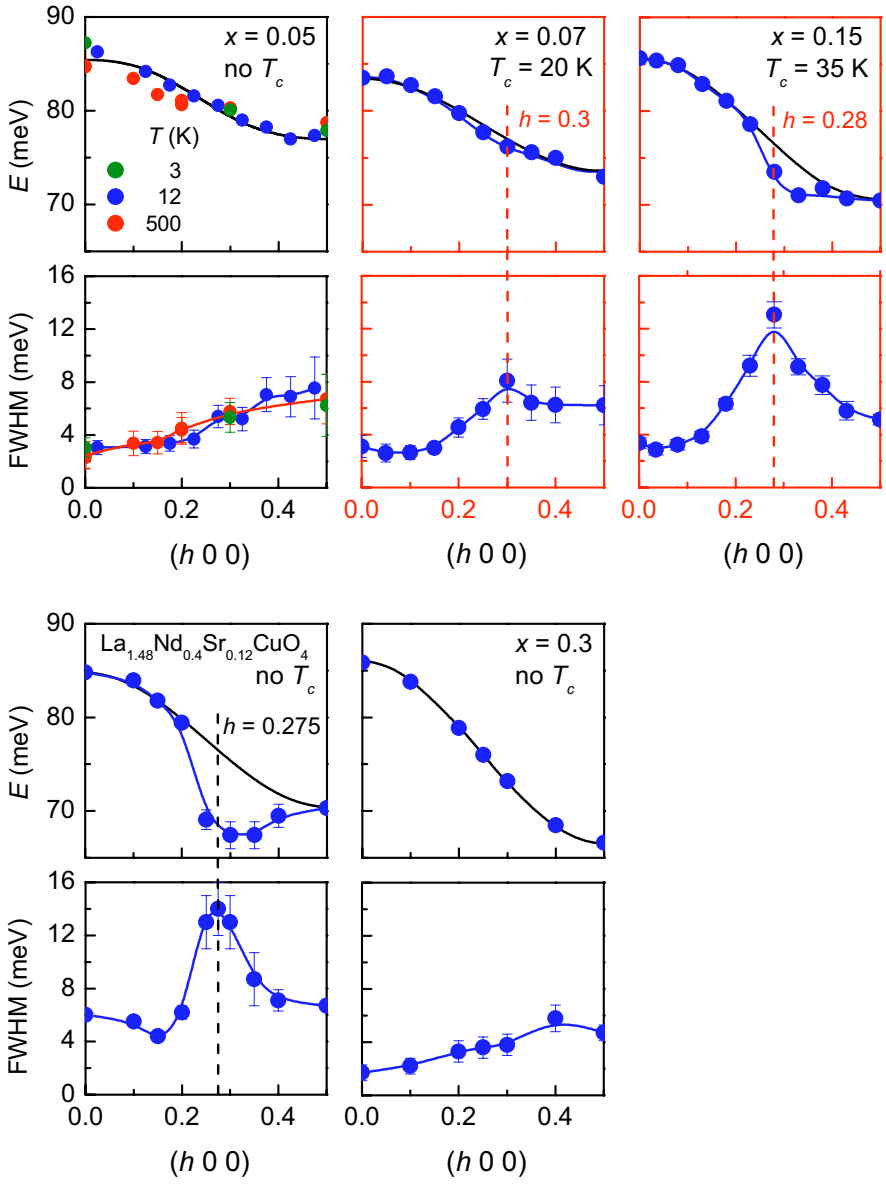

Figure 4.8: Dispersion and concurrent intrinsic linewidth of the Δ_1-branch in LSCO for several Sr-doping ratios x in comparison to $La_{1.48}Nd_{0.4}Sr_{0.12}CuO_4$. Data corresponding to $x = 0.05$ and 0.07 were extracted from an analysis such as discussed in Sec. 4.2.1.2. Other data were adopted from [89]. Black lines illustrate the 'normal' downward dispersion following a cosine function. Other lines are a guide to the eye. Data shown in blue correspond to a temperature about 12 K. Compounds revealing superconductivity below the respective critical temperature T_c are marked by the red frame. Note that the phonon anomaly is most pronounced in $La_{1.48}Nd_{0.4}Sr_{0.12}CuO_4$ revealing a static stripe phase that is detrimental to superconductivity.

new data on underdoped non-superconducting LSCO confirm the general point of view:

- In non-superconducting LSCO ($x = 0.05$ and $x = 0.3$) the Δ_1-branch is characteristic of a cosine-like downward dispersion and a concurrent gradual (almost linear) broadening of the phonon linewidth towards the zone boundary. For $x = 0.05$, the dispersion and the broadening are nearly T-independent between 3 K and 500 K. The softening at the zone boundary (compare Fig. 4.3) is least pronounced for LCO. It increases continuously with increasing doping through the superconducting regime and is most pronounced for non-superconducting but metallic $La_{1.7}Sr_{0.3}CuO_4$.

- On the other hand, data obtained on superconducting LSCO reveal a distinct maximum of the FWHM at around half-way to the zone boundary that is accompanied by a dip in the dispersion, strongly deviating from a simple cosine function and most pronounced in the optimally doped system (here also above T_c [72]).

- Non-superconducting LNSCO with $x = 0.12$ reveals static stripe order. This compound is indicative of the same anomalous behavior, yet even more pronounced.

To conclude, the above scenario strongly suggests a relation of the phonon anomaly in LSCO to superconductivity. The anomalous behavior has the same signature that is observed in the charge channel of LNSCO ($x = 0.12$) and there attributed to emerging static stripe order that is detrimental to superconductivity. In LNSCO ($x = 0.12$), the effect is most pronounced in close vicinity to $\mathbf{q} = (0.275\ 0\ 0)$ (note the dashed line in Fig. 4.8). On the other hand, a little smaller $\mathbf{q}_{co} = (2\varepsilon\ 0\ 0)$ would be expected from $\varepsilon \approx 0.12$ in $\mathbf{q}_{so}$ where the corresponding signature was found in the magnetic channel (compare Fig. 4.4). This indicates that the simple picture of spin charge segregation as presented in that Figure might be somewhat oversimplifying because the charge ordering wave vector is not just double the magnetic ordering wave vector.

In superconducting samples of LSCO, the phonon anomaly is strongest around $h = 0.3$ ($x = 0.07$) and $h = 0.28$ ($x = 0.15$). Again, smaller values are expected according to the magnetic channel (Fig. 4.4) and, most surprisingly, almost no doping dependence is revealed in the charge channel. If the phonon anomaly is interpreted in terms of dynamic stripes, then the corresponding fluctuating *charge* order seems to favor the same wave vector $\mathbf{q}_{fco}$ for both x as opposed to fluctuating *magnetic* order appearing at $\mathbf{q}_{so}$ with increasing ε towards increasing doping. Assuming a superposition of a 'normal' linear broadening and some anomalous peak-like broadening, the maximum of the latter is shifted towards the zone boundary, i.e., to slightly bigger h. Consequently, the anomalous behavior would be found most pronounced at somewhat smaller h when isolated from the linear 'background'. This might partly compensate for $\mathbf{q}_{fco}$ being too large.

However, the fact that there is no doping dependence of $\mathbf{q}_{fco}$ in the charge channel in contrast to the pronounced doping dependence of $\mathbf{q}_{so}$ in the magnetic channel remains a puzzling issue and renders further investigation necessary.

4.3 $HgBa_2CuO_{4+\delta}$

Phonon anomalies such as observed in the LSCO family are also found in other cuprate superconductors [9, 10]. In $YBa_2Cu_3O_{7-\delta}$ (YBCO) at optimal doping, certain bond-stretching phonons reveal an anomaly that is in many respects similar to the one in LSCO [90]. The orthorhombic unit cell contains two inequivalent CuO_2 layers introducing two bond-stretching branches of Δ_1- and Δ_4-symmetry, respectively, complicating the analysis [10]. Moreover, even the electron-doped cuprate $Nd_{2-x}Ce_xCuO_4$ (NCCO) shows a similar anomaly which is further discussed in [9].

In this section, new results obtained on $HgBa_2CuO_{4+\delta}$ (Hg1201) are presented in comparison to previous data. The crystal structure is tetragonal and the unit cell contains one completely flat CuO_2 plane, as depicted in Fig. 4.9 (left panel). In contrast to the complex structure in YBCO and the tetragonal to orthorhombic phase transition in LSCO, the comparatively simple structure of Hg1201 makes it an ideal candidate for phonon studies. Despite its simple structure, the transition temperature T_c of the optimally doped system of about 98 K is even higher than in YBCO (93 K [90]). In fact, members of the Hg-based family even have the highest $T_c \approx 135$ K demonstrated to date.

In LSCO, the interesting longitudinal Cu-O bond-stretching vibration is the one with the highest energy among all phonon branches of Δ_1-symmetry. The next closest mode of this symmetry (the bond-bending mode) appears at considerably lower energy (at least in the case of low Sr-doping that was considered in the last Section) and is therefore without influence on the longitudinal bond-stretching mode. Consequently, Δ_1-modes other than the bond-stretching vibration did not have to be taken into account and the latter was simply referred to as the 'Δ_1-branch'. On the contrary, three phonon modes of Δ_1-symmetry have to be distinguished in Hg1201 in the energy range of interest: the bond-stretching branch is closely surrounded by the *c*-polarized apical oxygen mode (towards higher energy) and by the bond-bending mode (towards lower energy). This scenario is illustrated by solid lines in the right panel of Fig. 4.9 indicating the respective dispersions around (3 0 0) as calculated with a shell model. In addition, the measured dispersion of the bond-stretching branch as obtained with inelastic X-ray scattering (IXS) is shown as black dots [11]. (Note that the vertical bars indicate the FWHM of corresponding peaks and are not to be mistaken as error bars.) These results are indicative of an anomalous softening (dip in the dispersion) similar to LSCO and YBCO.

Group theory tells us that phonon branches of the same symmetry class (e.g., Δ_1)

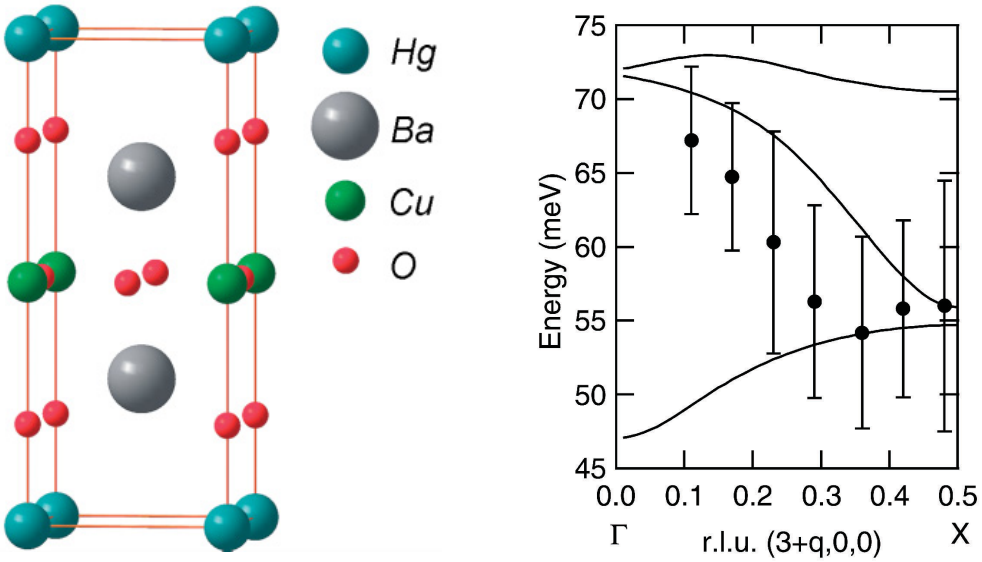

Figure 4.9: (Left panel) Tetragonal unit cell of Hg1201 with the lattice constants of $a = 3.875\,\text{Å}$ and $c = 9.513\,\text{Å}$ revealing a completely flat CuO_2 plane. The Figure was adopted from [91]. (Right panel) Previous results obtained with IXS on Hg1201 at $T = 55\,\text{K}$ well below $T_c = 94\,\text{K}$ as presented in [11]. The measured dispersion of the bond-stretching branch is shown as black dots with the vertical bars indicating the FWHM of corresponding peaks. Solid lines indicate shell model calculations of (top to bottom) the c-polarized apical oxygen mode, the bond-stretching mode and the bond-bending mode.

are not allowed to cross each other. If, due the special nature of the interatomic interactions, two such branches tend to cross each other in a particular part of the Brillouin zone, a mixing of their polarization patterns and a mutual repulsion of the eigenfrequencies will be the result [92] (analogous to the problem of coupled harmonic oscillators). As this is the case for the bond-stretching and the bond-bending branch in the vicinity of the zone boundary, a clear assignment of a measured peak to either of the branches is difficult. Uchiyama et al. argue in [11] that the calculated structure factor of the bond-bending mode is much weaker than the structure factor of the bond-stretching mode. (The intensity predicted for the apical oxygen mode is so weak as to be unobservable.) And even if one cannot completely exclude the possibility of mixing above $q \approx 0.3$, the bond-bending mode should give a signal that is close to resolution limited (as reported for YBCO and LSCO). The observed FWHM of $\geq 12\,\text{meV}$ at $q \geq 0.3$ is much larger than the resolution ($6.0 - 6.3\,\text{meV}$) and is thus indicative of a dominant contribution from the bond-stretching mode. However, data presented in [11] are somewhat marginal especially in the vicinity of the zone-boundary where the influence of the bond-bending branch should be addressed in further investigations.

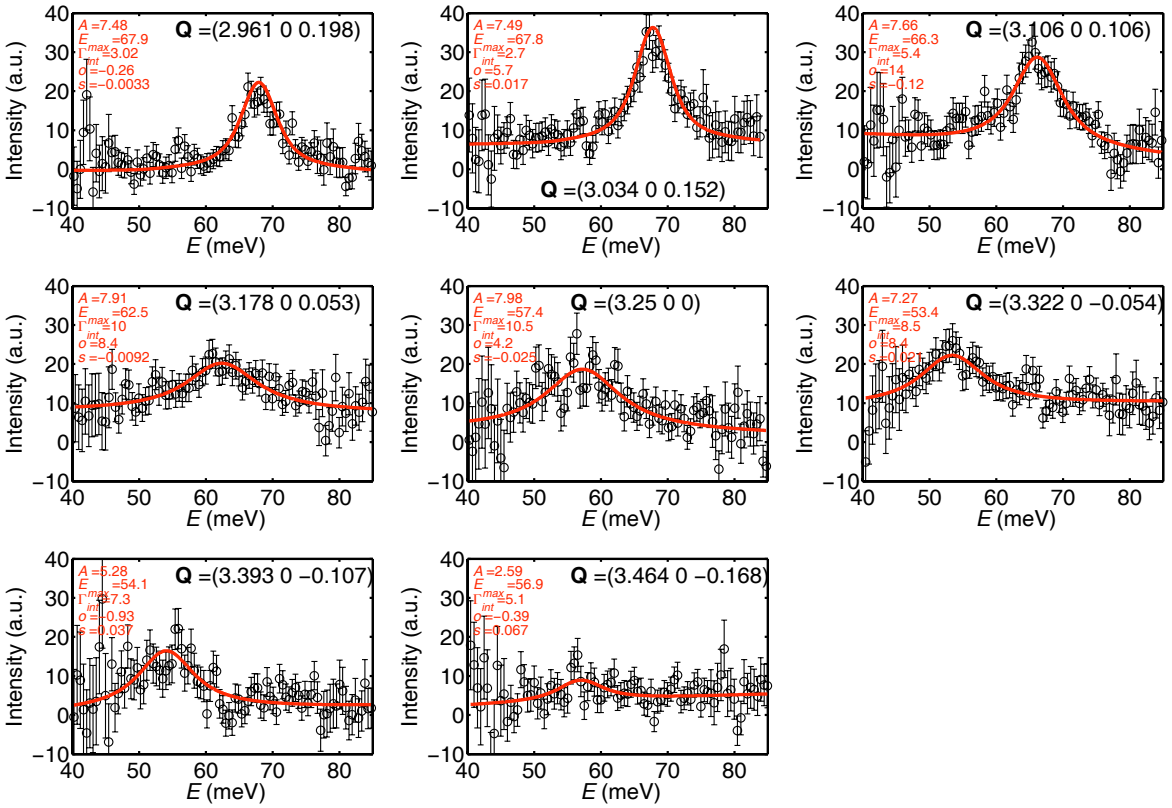

Figure 4.10: E scans on Hg1201 at $T = 250\,\mathrm{K}$ tracing the Δ_1-branch from close to the zone center (upper left panel) towards close to the zone boundary (lower right panel). Contributions from low-energy phonons and the elastic line are subtracted. Solid lines show fits to data where the measured resolution function is convoluted with a Lorentzian accounting for the intrinsic linewidth.

4.3.1 Experimental results

Anomalous phonon behavior might be a consequence of superconductivity, thus emerging below T_c only. To actually confirm a possible relation of the anomaly to the mechanism *causing* superconductivity, its presence in the non-superconducting phase above T_c is crucial (as it is the case in LSCO and YBCO). Therefore, we investigated the bond-stretching phonon branch in Hg1201 at a temperature of 250 K well above $T_c = 94\,\mathrm{K}$. Single crystals of a size amenable to neutron scattering have recently become available [91]. Unfortunately, our first experiments on a single-crystalline sample[9] performed on the 1T spectrometer suffered from a huge background hampering a reliable

[9]The sample of about 1.2 g with a mosaic of less than half a degree was provided by the 'Department of Applied Physics' of the Stanford University, Stanford (USA).

analysis. Alternatively, we used inelastic X-ray scattering (IXS) at ESRF in Grenoble (France) to investigate the anomalous phonon behavior. Scans were performed in the vicinity of the nuclear (3 0 0) Bragg peak to maximize the dynamic structure factor and to facilitate a comparison with previous data at 55 K such as presented in Fig. 4.9.

It is important to note some crucial differences between IXS and INS: IXS allows to measure much smaller samples because the typical diameter of the beam is in the order of 100 μm as opposed to centimeters in the case of neutrons. Due to the strong interaction of photons with electrons, the penetration depth into the sample is much smaller for X-rays than for neutrons and decreases considerably with the increasing atomic number. In particular, heavy elements such as Hg and Ba reduce the illuminated sample volume, e.g., by a factor of three compared to previous IXS studies of NCCO [11]. Compared to neutron scattering IXS provides superior wavevector and energy resolution at large energy transfers but lower resolution at low energies. A major drawback of IXS is the Lorentzian-like resolution function (vs. Gaussian for INS). Resulting tails of the elastic line and intense low-energy excitations contribute significantly to the background at high energies. In addition, the dynamic structure factor of the bond-stretching branch in Hg1202 decreases much more quickly towards the zone boundary for IXS than for INS complicating a reliable measurement of the intrinsic FWHM.

The ID-28 beamline at ESRF provides nine analyzer crystals (each with an independent detector) allowing to measure nine different $\mathbf{Q}$, simultaneously. In order to get a proper estimate of the experimental resolution function in each of the nine channels, we measured a sample of polymethyl methacrylate under exactly the same conditions used to investigate Hg1201: A Pseudo-Voigt function $V_i(E)$ (i enumerates respective channels) consisting of a Gaussian and up to six Lorentzians properly describes the measured spectra and hence is used in the following to model the elastic line (scaled accordingly). Furthermore, phonon peaks are modeled by convoluting the normalized Pseudo-Voigt function $V_{0,i}(E)$ with a Lorentzian $L_i(E - E_{max}; A, \Gamma_{int})$ to account for finite intrinsic linewidths (FWHM) Γ_{int}. We used density functional theory (DFT) in the local density approximation (LDA) to calculate expected energy positions (E_{max}) and dynamic structure factors (related to area A) [93], considering the Bose-factor and $1/\omega$ such as shown in Eq. (1.29). The measured scattering intensity in the energy range of the bond-stretching branch is depicted in Fig. 4.10. Contributions from lower energy phonons and the elastic line are already subtracted. The small structure factor at the zone boundary hampered a reliable detection of the phonon peak there. Consequently, this analyzer channel is omitted in the Figure. At all $\mathbf{Q}$, the area A is fixed to the calculated value and the background resulting from multi-phonon and incoherent scattering is assumed to vary linearly with energy. Corresponding offset (o) and slope (s) are fitted at each $\mathbf{Q}$, respectively, to compensate for slight changes in the background among the nine detectors. The peak position E_{max} and the intrinsic linewidth Γ_{int} are adapted at every $\mathbf{Q}$ as well.

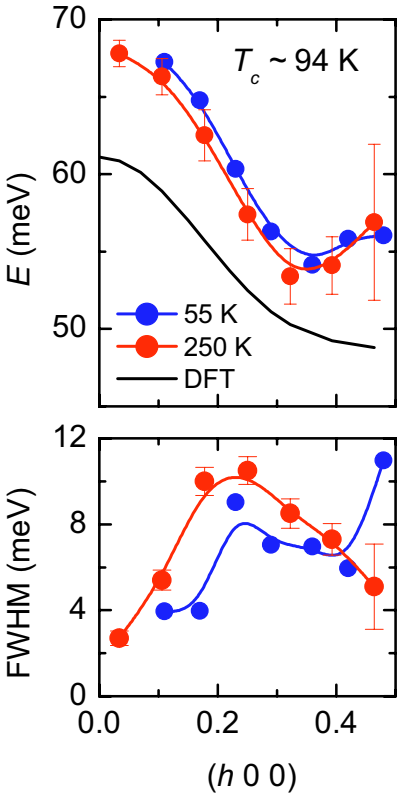

Figure 4.11: Dispersion and concurrent intrinsic linewidth (FWHM) of the bond-stretching branch at temperatures well below (blue) and above (red) T_c in comparison to the calculated dispersion according to DFT (black line). Red and blue lines are a guide to the eye. Data at 55 K correspond to those exhibited in the right panel of Fig. 4.9 as adopted from [11]. Note that the resolution-based FWHM of about 6 meV was subtracted in order to facilitate a comparison with data at 250 K revealing the intrinsic linewidth Γ_{int} as extracted from fits shown in Fig. 4.10.

4.3.2 Discussion

The measured dispersion and concurrent intrinsic linewidth as extracted from the above analysis is depicted in Fig. 4.11. It reveals a dip in the dispersion of the bond-stretching phonon branch that is in pronounced contrast to the monotonic behavior expected from DFT. The latter obviously underestimates the phonon energies throughout the Brillouin zone but yet predicts a cosine-like behavior similar the shell model. The comparison with previous data obtained at $T = 55$ K from [11] demonstrates that the dispersion does not change significantly upon heating to 250 K. Moreover, anomalous broadening most pronounced around half-way to the zone boundary is found at both temperatures. Judging from the tiny phonon intensity at the zone boundary, the value of about 11 meV at $h = 0.48$ and $T = 55$ K might be somewhat overestimated. Fixing the area of respective phonon peaks to the DFT-calculated value seems to have improved our analysis at 250 K. However, neither previous data nor our results allow for a reliable extraction of the intrinsic FWHM at the zone boundary.

To summarize, the anomalous phonon behavior observed in the bond-stretching phonon branch is present not only in the superconducting phase but also well above T_c. Although extending this study to different dopings, temperatures and nonzero wavevectors is important, it strongly suggests already at this stage a relation of the

phonon anomaly to the mechanism responsible for superconductivity.

4.4 Conclusion

Previous experiments revealed anomalous phonon behavior of the longitudinal plane-polarized Cu-O bond-stretching vibration in LSCO: Around $\mathbf{q} = (0.3\ 0\ 0)$, this phonon mode is softer and broader than expected from conventional theory such as DFT or shell models. The effect may be related to incipient instability with regard to the formation of dynamic (fluctuating) stripes or another charge-order or inhomogeneous state. The phonon anomaly reveals a distinct doping dependence as it is absent in overdoped non-superconducting LSCO and is very pronounced in the optimally doped system with $T_c = 35\,\mathrm{K}$. Here, it is present also above T_c.

In this work, measurements on underdoped LSCO were performed to complete the systematic study of this compound. Special emphasis was laid on considering the 4D resolution function of the spectrometer in $\mathbf{Q}$ and ω in order to extract the intrinsic linewidth of the phonons. We found that the anomalous phonon behavior is present in superconducting $La_{1.93}Sr_{0.07}CuO_4$ ($T_c = 20\,\mathrm{K}$), albeit less pronounced than in optimally doped LSCO. Furthermore, it is absent in non-superconducting $La_{1.95}Sr_{0.05}CuO_4$.

Similar phonon anomalies have been found in other cuprate superconductors with a higher T_c as well, such as YBCO and Hg1201. However, the data for Hg1201 reported in the literature are of marginal quality. Moreover, measurements were done only for a temperature well below T_c. This motivated us to perform another study on the same compound. Unfortunately, we could not substantially improve the data quality. Nevertheless, we achieved some progress by basing our analysis on DFT-results rather than on a simple phenomenological model as was done previously. Further, we were able to show that the phonon anomaly persists above T_c.

The results presented in this work together with the results reported in the literature strongly suggest that the phonon anomaly in the Cu-O bond-stretching branch is intimately connected to superconductivity. However, there is as yet no theory available to unravel the role of the anomalous phonons for the mechanism of high-T_c superconductivity.

Summary

Thanks to the high versatility of neutron scattering, a variety of phenomena in different classes of strongly correlated electron systems could be studied by this technique: Quasielastic scattering from spin fluctuations in MnSi above $T_C = 29.5\,K$ revealed the detailed temperature dependence of their dynamics and signature in $\mathbf{Q}$ space. Elastic scattering from magnetic order in $CeCu_{5.5}Au_{0.5}$ was performed at temperatures below 100 mK to investigate the pressure dependence of the magnetic ordering wave vector $\mathbf{q}_m$ up to $p = 8\,kbar$. Finally, neutrons were scattered inelastically from nuclear excitations (phonons) in cuprate superconductors at temperatures between 3 K and 500 K to study their anomalous behavior. In the following, the main results obtained on each system are briefly summarized.

Dynamic spin clusters in the paramagnetic phase of MnSi

A unique magnetic state referred to as 'partial order' (PO) had been found previously in MnSi at high pressures above $p \sim 14\,kbar$ and below some crossover temperature T_0. PO is characterized by long-range helical correlations but disordered propagation directions. At ambient pressure and above T_C, small-angle neutron measurements were indicative of a structure very similar to PO that quickly disappears upon heating.

We were able to show by measurements with a triple-axis spectrometer that there are indeed magnetic correlations at ambient pressure which resemble the PO at high pressures. Their dynamics is extremely slow, even at temperatures far above T_C, i.e., at 100 K. For a better understanding of this state, we performed calculations on finite-size spin clusters with the structure of MnSi. The results of these calculations allow us to interpret the experimental results of this work and those of previous studies in a qualitative manner:

PO is most likely a collection of chiral-ordered spin clusters that form above T_C at all pressures and slowly diffuse in the paramagnetic background. The calculated structure is similar to packed double-helices known from the blue phases of chiral liquid crystals but features a third independent twist direction that leads us to the terminology of 'triple-helices'. Their Fourier transform resembles the experimentally observed scattering function. On increasing the temperature, the number and size of magnetically ordered clusters is gradually reduced but small clusters survive up to

fairly high temperatures. The phase transition to the locked helix, that is favored once the correlation length exceeds a certain value at T_C, happens in a first order fashion because both phases are topologically distinct. This is why the specific heat $C(T)$ shows a clear first-order-like spike at the phase transition. Our model further explains the reduction of T_C by replacing a part of the Mn atoms by Fe, because the correlation length is reduced by Fe impurities, thus stabilizing the PO phase at a given temperature. The non - Fermi liquid (NFL) behavior in MnSi in certain parts of the phase diagram might originate from the scattering of conduction electrons by the triple-helix clusters. Calculations of the transport properties are necessary to test these ideas further.

Tuning behavior of magnetic order in $CeCu_{6-x}Au_x$

$CeCu_{6-x}Au_x$ is one of most extensively studied heavy-fermion systems that offers unique possibilities to investigate NFL behavior related to a quantum critical point (QCP) which can be tuned by different parameters such as Au concentration x, hydrostatic pressure p or magnetic field B. A striking equivalence of the tuning behavior with x or p had been found with respect to macroscopic properties such as the specific heat, the magnetic susceptibility and the electrical resistivity.

We succeeded to confirm this x - p equivalence on a microscopic level by showing that a microscopic quantity, i.e., the magnetic ordering wave vector $\mathbf{q}_m$, can be tuned accordingly. At ambient pressure $CeCu_{5.5}Au_{0.5}$ orders at $\mathbf{q}_m \approx (0.59\ 0\ 0)$. Upon applying $p = 4.1\,\mathrm{kbar}$, $\mathbf{q}_m \approx (0.61\ 0\ 0.21)$ is found corresponding to $CeCu_{5.6}Au_{0.4}$ at ambient pressure. The transition seems to happen in a first order fashion. However, increasing the pressure further $\mathbf{q}_m$ of $CeCu_{5.5}Au_{0.5}$ saturates at a value that is somewhat smaller than expected from a comparison with corresponding systems at ambient p. This issue needs further attention and should be addressed in future investigations. A higher pressure than achievable in this study would allow one to tune $CeCu_{5.5}Au_{0.5}$ into quantum criticality and to investigate the fluctuations there. This might help to gain more insight into the mechanisms that drive the quantum phase transition.

Anomalous phonon behavior in cuprate high-T_c superconductors

It was known for a long time that the longitudinal plane-polarized Cu-O bond-stretching vibrations in $La_{2-x}Sr_xCuO_4$ (LSCO) show a strong doping dependence: whereas the zone center frequency remains essentially unchanged, the zone boundary frequencies decrease substantially with increasing x, in particular along the $\langle 1\ 0\ 0\rangle$ direction. Later, it became clear that the softening of the zone boundary modes is not related to superconductivity because it continues into the overdoped regime where superconductivity vanishes. On the other hand, a very pronounced softening and broadening (pointing towards a strong electron-phonon coupling) around $\mathbf{q} = (0.3\ 0\ 0)$ observed in the op-

timally doped system with $x = 0.15$ did seem to be correlated with superconductivity because it was absent in overdoped, non-superconducting LSCO with $x = 0.3$. We note that this effect is not expected from conventional theories such as density functional theory (DFT) or shell models. It is thought to be related to an incipient instability with regard to the formation of charge stripes (spin charge segregation). In order to confirm the conjecture that this anomaly is linked to superconductivity, it was crucial to extend the measurements to the underdoped side of the phase diagram. We found that the anomalous phonon behavior is present in superconducting $La_{1.93}Sr_{0.07}CuO_4$ ($T_c = 20\,\mathrm{K}$), albeit less pronounced than in optimally doped LSCO, but is absent in non-superconducting $La_{1.95}Sr_{0.05}CuO_4$. Thus, our results corroborate the hypothesis that this particular type of phonon anomaly is associated with superconductivity.

Similar phonon anomalies have been found in other cuprate superconductors with a higher T_c as well, such as $YBa_2Cu_3O_{7-\delta}$ (YBCO) or $HgBa_2CuO_{4+\delta}$ (Hg1201). However, the data for the latter compound reported in the literature were of marginal quality. This motivated us to perform another study on the same compound. Unfortunately, we could not substantially improve the data quality because of the high absorption cross-section of mercury. Nevertheless, we achieved some progress by basing our analysis on DFT results rather than on a simple phenomenological model as was done previously. Further, we were able to show that the phonon anomaly persists at a temperature of 250 K, i.e., well above T_c.

The results presented in this work together with the results reported in the literature strongly suggest that the phonon anomaly in the Cu-O bond-stretching branch is intimately connected to superconductivity. However, there is as yet no theory available to unravel the role of the anomalous phonons for the mechanism of high-T_c superconductivity.

Appendix A

MnSi

A.1 Optimization of spin clusters

The spin cluster calculations where performed using the program package MATLAB® in the version R2008b. 8 to 16 CPUs provided by the 'Institut für Wissenschaftliches Rechnen und Mathematische Modellbildung' (IWRMM) and the 'Steinbuch Centre for Computing' (SCC) of the 'Karlsruhe Institute of Technology' (KIT) calculated for about four months to achieve the results presented in Sec. 2.3. The algorithm developed to optimize the spin clusters is very briefly introduced in the following.

First, a cluster of a certain rectangular shape is initialized with ferromagnetic, helical or random spin configurations on a simple cubic lattice or Mn sites in the B20 MnSi structure. Thereby, the lattice sites are enumerated and mapped injectively onto a one-dimensional list (a so-called 'field array') that is to contain all information about the cluster and can be handled much more efficiently than a true 3D object. Let N be the number of lattice sites, i.e., the number of spins[1], then each of the N 'fields' contains the orientation of the normalized spin (in spherical coordinates) and pointers to other fields corresponding to the respective nearest neighbors.

Orientation optimization with regard to Eq. (2.6) is performed for individual spins one-by-one in random order keeping their magnitudes constant. In initialized clusters none of the spins is optimized and hence all spins are selectable. After optimization of the spin at site i, this spin remains non-selectable until one of its nearest neighbors at sites $j(i)$ has been optimized. In comparison to selecting the next spin among *all* spins, this method significantly accelerates the convergence of the total energy.

After each $10N$ spin optimizations the total energy E_{new} of the cluster $\mathbf{C}_{\mathrm{new}}$ is calculated and is compared with the old value E_{old} of the corresponding cluster $\mathbf{C}_{\mathrm{old}}$.

[1] Sec. 2.4 addresses Fe-doped clusters on page 45. There, the number of spins is smaller than the number of lattice sites because Fe impurities are modeled by empty sites. This special case is not considered here.

If $E_{\text{new}} < E_{\text{old}}$, i.e., if the optimization of the spin configuration has been effective, the new cluster is taken to be further optimized. If the configuration could not be improved, i.e., if $E_{\text{new}} \geq E_{\text{old}}$, $\mathbf{C}_{\text{new}}$ is discarded and the old cluster is tried to be optimized once again (using a different random seed). This process is repeated until $|E_{\text{new}} - E_{\text{old}}|$ falls below a certain threshold value. On the other hand, it is interrupted triggering an error message if $E_{\text{new}} \geq E_{\text{old}}$ three times in a row.

The actual optimization of a spin at site i with respect to its nearest neighbors is achieved by a standard MATLAB® routine called '`fmincon`' of which we limited the maximum number of iterations not to exceed 30 to further accelerate the convergence of the total energy.

A.2 Quantitative energy considerations

In the following, the Hamiltonian $\mathcal{H}_0$ as presented in Eq. (2.7) is considered. For given D and J, the energy for just one pair of spins (one bond) is given by

$$E = -J\mathbf{s}_i \cdot \mathbf{s}_j - \mathbf{D} \cdot (\mathbf{s}_i \times \mathbf{s}_j) \ . \tag{A.1}$$

Assuming that $\mathbf{D} = (D, 0, 0)$, $\mathbf{s}_i = (0, 0, 1)$ and $\mathbf{s}_j = (0, s, \sqrt{1 - s^2})$ (spins are normalized), it is easy to show that Eq. (A.1) is minimized for

$$s = s_0 = -\sqrt{\frac{\frac{D^2}{J^2}}{1 + \frac{D^2}{J^2}}} \tag{A.2}$$

and correspondingly,

$$E_{\text{1D}} := E(s_0) = -J\sqrt{1 - \frac{\frac{D^2}{J^2}}{1 + \frac{D^2}{J^2}}} - D\sqrt{\frac{\frac{D^2}{J^2}}{1 + \frac{D^2}{J^2}}} \ . \tag{A.3}$$

E_{1D} corresponds to case of a fully optimized and unfrustrated 1D chain as shown in Fig. 2.10. A cluster of random spins yields an average of zero energy per bond:

$$E_{\text{rand}} = 0 \ . \tag{A.4}$$

Ferromagnetically aligned spins optimize the first term in Eq. (A.1) but cancel the second resulting in

$$E_{\text{FM}} = -J \ . \tag{A.5}$$

In our model each spin has six nearest neighbors. The perfect helix structure with Energy E_{helix} (crystal potential neglected) can be considered as a 3D extension of a 1D helix because spins are parallel to each other in 2D planes perpendicular to the helix propagation vector $\mathbf{k}_{\text{h}}$. Thus, in the B20 structure with $\mathbf{k}_{\text{h}}$ along $\langle 1\ 1\ 1 \rangle$, in

average four neighboring spins are parallel (in the same plane perpendicular to the helix propagation vector) and two spins are perfectly optimized such that

$$E_{\text{helix}} = \frac{2}{3}E_{\text{FM}} + \frac{1}{3}E_{\text{1D}} \,, \tag{A.6}$$

and consequently

$$E_{\text{h}} := E_{\text{helix}} - E_{\text{FM}} = \frac{1}{3}J + \frac{1}{3}E_{\text{1D}} \tag{A.7}$$

$$= \frac{J}{3}\left(1 - \sqrt{1 - \frac{\frac{D^2}{J^2}}{1+\frac{D^2}{J^2}}}\right) - \frac{D}{3}\sqrt{\frac{\frac{D^2}{J^2}}{1+\frac{D^2}{J^2}}} \,. \tag{A.8}$$

List of Figures

Bibliography

[1] L. D. Landau, *The Theory of a Fermi Liquid*, Sov. Phys. JETP, **3**, 920 (1957).

[2] D. Pines, P. Nozières, *The Theory Of Quantum Liquids* (W. A. Benjamin inc., New York, 1966).

[3] C. Pfleiderer, D. Reznik, L. Pintschovius, H. v. Löhneysen, M. Garst, A. Rosch, *Partial order in the non-Fermi-liquid phase of MnSi*, Nature, **427**, 227 (2004).

[4] S. V. Grigoriev, S. V. Maleyev, A. I. Okorokov, Yu. O. Chetverikov, R. Georgii, P. Böni, D. Lamago, H. Eckerlebe, K. Pranzas, *Critical fluctuations in MnSi near T_C: A polarized neutron scattering study*, Phys. Rev. B, **72**, 134420 (2005).

[5] H. v. Löhneysen, *Non-Fermi-liquid behaviour in the heavy-fermion system $CeCu_{6-x}Au_x$*, J. Phys. Cond. Matt., **8**, 9689 (1996).

[6] H. v. Löhneysen, A. Rosch, M. Vojta, P. Wölfle, *Fermi-liquid instabilities at magnetic quantum phase transitions*, Rev. Mod. Phys., **79**, 1015 (2007).

[7] O. Stockert, H. v. Löhneysen, A. Rosch, N. Pyka, M. Loewenhaupt, *Two-Dimensional Fluctuations at the Quantum-Critical Point of $CeCu_{6-x}Au_x$*, Phys. Rev. Lett., **80**, 5627 (1998).

[8] J. Bardeen, L. N. Cooper, J. R. Schrieffer, *Theory of Superconductivity*, Phys. Rev., **108**, 1175 (1957).

[9] L. Pintschovius, *Electron-phonon coupling effects explored by inelastic neutron scattering*, Phys. stat. sol. (b), **242**, 30 (2005).

[10] D. Reznik, *Giant Electron-Phonon Anomaly in Doped La_2CuO_4 and Other Cuprates*, Advances in Condensed Matter Physics, **2010**, 523549 (2009).

[11] H. Uchiyama, A. Q. R. Baron, S. Tsutsui, Y. Tanaka, W. Z. Hu, A. Yamamoto, S. Taijima, Y. Endoh, *Softening of Cu-O Bond Stretching Phonons in Tetragonal $HgBa_2CuO_{4+\delta}$*, Phys. Rev. Lett., **92**, 197005 (2004).

[12] G. Ekspong, *Nobel Lectures in Physics 1991-1995* (World Scientific, Singapore, 1997).

[13] Gen Shirane, Stephen M. Shapiro, John M. Tranquada, *Neutron Scattering with a Triple-Axis Spectrometer* (Cambridge University Press, New York, 2002).

[14] G. L. Squires, *Introduction to the theory of thermal neutron scattering*, 2^{nd} edition (Dover publications, Inc., Mineola, New York, 1996).

[15] W. Marshall, S. Lovesey, *Theory of Thermal Neutron Scattering* (Oxford University Press, Ely House, London, 1971).

[16] O. Stockert, *Spindynamik und magnetische Ordnung in* $CeCu_{6-x}Au_x$, Dissertation, Physikalisches Institut, Universität Karlsruhe, Cuvillier Verlag Göttingen, 1999.

[17] P. M. Chaikin, T. C. Lubensky, *Principles of condensed matter physics* (University Press, Cambridge, 1995).

[18] P. Bak, M. H. Jensen, *Theory of helical magnetic structures and phase transitions in MnSi and FeGe*, J. Phys. C: Solid St. Phys., **13**, (1980).

[19] I. E. Dzyaloshinski, *A thermodynamic theory of "weak" ferromagnetism of antiferromagnetics*, J. Phys. Chem. Solids, **4**, 241 (1958).

[20] T. Moriya, *Anisotropic Superexchange Interaction and Weak Ferromagnetism*, Phys. Rev, **120**, 91 (1960).

[21] B. Roessli, P. Böni, W. E. Fischer, Y. Endoh, *Chiral Fluctuations in MnSi above the Curie Temperature*, Phys. Rev. Lett., **88**, 237204 (2002).

[22] D. Lamago, private communication, 2009, (Institut für Festkörperphysik, Karlsruhe Institute of Technology (KIT), Germany).

[23] C. Pfleiderer, G. J. McMullan, S. R. Julian, G. G. Lonzarich, *Magnetic quantum phase transition in MnSi under hydrostatic pressure*, Phys. Rev. B, **55**, 8330 (97).

[24] Y. Ishikawa, K. Tajima, D. Bloch, M. Roth, *Helical spin structure in manganese silicide MnSi*, Solid State Comm., **19**, 525 (1976).

[25] Y. Ishikawa, T. Komatsubara, D. Bloch, *Magnetic Phase Diagram of MnSi*, Physica, **86 - 88B**, 401 (1977).

[26] N. Doiron-Leyraud, I. R. Walker, L. Taillefer, M. J. Steiner, S. R. Julian, G. G. Lonzarich, *Fermi-liquid breakdown in the paramagnetic phase of a pure metal*, Nature, **425**, 595 (2003).

[27] L. M. Levinson, G. H. Lander, M. O. Steinitz, *Magnetism and Magnetic Materials – 1972 (Denver)* (Proceedings of the 18th Annual Conference on Magnetism and Magnetic Materials, edited by C. D. Graham and J. J. Rhyne (American Institute of Physics), New York, 1973), p. 1138.

[28] Y. Ishikawa, Y. Noda, C. Fincher, G. Shirane, *Low-energy paramagnetic spin fluctuations in the weak itinerant ferromagnet MnSi*, Phys. Rev. B, **25**, 254 (1982).

[29] C. Pappas, E. Lelièvre-Berna, P. Falus, P. M. Bentley, E. Moskvin, S. Grigoriev, P. Fouquet, B. Farago, *Chiral Paramagnetic Skyrmion-like Phase in MnSi*, Phys. Rev. Lett., **102**, 197202 (2009).

[30] U. K. Rößler, A. N. Bogdanov, C. Pfleiderer, *Spontaneous skyrmion ground states in magnetic metals*, Nature, **442**, 797 (2006).

[31] C. Pfleiderer, D. Reznik, L. Pintschovius, J. Haug, *Magnetic field and pressure dependence of small angle neutron scattering in MnSi*, Phys. Rev. Lett., **99**, 156406 (2007).

[32] D. Reznik, private communication, 2009, (Department of Physics, University of Colorado, Boulder, USA).

[33] D. Lamago, R. Georgii, C. Pfleiderer, P. Böni, *Magnetic-field induced instability surrounding the A-phase of MnSi: Bulk and SANS measurements*, Physica B, **385 - 386**, 385 (2006).

[34] A. Petrova, S. Stishov, *Ultrasonic studies of the magnetic phase transition in MnSi*, J. Phys.: Condens. Matter, **21**, 196001 (2009).

[35] Y. J. Uemura, T. Goko, I. M. Gat-Malureanu, J. P. Carlo, P. L. Russo, A. T. Savici, A. Aczel, G. J. MacDougall, J. A. Rodriguez, G. M. Luke, S. R. Dunsiger, A. McCollam, J. Arai, Ch. Pfleiderer, P. Böni, K. Yoshimura, E. Baggio-Saitovitch, M. B. Fontes, J. Larrea, Y. V. Sushko, J. Sereni, *Phase separation and suppression of critical dynamics at quantum phase transitions of MnSi and* $(Sr_{1-x}Ca_x)RuO_3$, Nat. Phys., **3**, 29 (2007).

[36] D. C. Wright, N. David Mermin, *Crystalline liquids: the blue phases*, Rev. Mod. Phys., **61**, 2 (1989).

[37] S. Mühlbauer, B. Binz, F. Jonietz, C. Pfleiderer, A. Rosch, A. Neubauer, R. Georgii, P. Böni, *Skyrmion Lattice in a Chiral Magnet*, Science, **323**, 915 (2009).

[38] S. V. Grigoriev, S. V. Maleyev, A. I. Okorokov, Yu. O. Chetverikov, P. Böni, R. Georgii, D. Lamago, H. Eckerlebe, K. Pranzas, *Magnetic structure of MnSi under*

an applied field probed by polarized small-angle neutron scattering, Phys. Rev. B, **74**, 214414 (2006).

[39] Y. Ishikawa, G. Shirane, J. A. Tarvin, M. Kohgi, *Magnetic excitations in the weak itinerant ferromagnet MnSi*, Phys. Rev. B, **16**, 11 (1977).

[40] N. Manyala, Y. Sidis, J. F. DiTusa, G. Aeppli, D. P. Young, Z. Fisk, *Magnetoresistance from quantum interference effects in ferromagnets*, Nature, **404**, 581 (2000).

[41] D. Belitz, T. R. Kirkpatrick, A. Rosch, *Theory of helimagnons in itinerant quantum systems. II. Nonanalytic corrections to Fermi-liquid behavior*, Phys. Rev. B, **74**, 024409 (2006).

[42] C. Meingast, Q. Zhang, Th. Wolf, F. Hardy, K. Grube, W. Knafo, P. Adelmann, P. Schweiss, H. v. Löhneysen, *Resistivity of $Mn_{1-x}Fe_xSi$ single crystals: evidence for quantum critical behavior*, Properties and Applications of Thermodynamic Materials (edited by V. Zlatic and A. C. Hewson, Springer Science + Business Media B. V. 2009) .

[43] K. Grube, private communication, 2010, (Institut für Festkörperphysik, Karlsruhe Institute of Technology (KIT), Germany).

[44] T. Pietrus, B. Bogenberger, S. Mock, M. Sieck, H. v. Löhneysen, *Pressure dependence of the Néel temperature in antiferromagnetic $CeCu_{6-x}Au_x$ for $0.3 \leq x \leq 1.3$*, Physica B, **206 & 207**, 317 (1995).

[45] A. C. Hewson, *The Kondo Problem to Heavy Fermions* (University Press, Cambridge, 1993).

[46] H. G. Schlager, A. Schröder, M. Welsch, H. v. Löhneysen, *Magnetic Ordering in $CeCu_{6-x}Au_x$ Single Crystals: Thermodynamic and Transport Properties*, J. Low Temp. Phys., **90**, 181 (1993).

[47] A. Amato, D. Jaccard, *Thermodynamic and Transport Properties of $CeCu_6$*, J. Low Temp. Phys., **68**, 371 (1987).

[48] Y. Onuki, Y. Shimizu, T. Komatsubara, *Anisotropic Magnetic Property of Kondo Lattice Substance: $CeCu_6$*, J. Phys. Soc. Jpn., **54**, 304 (1985).

[49] H. R. Ott, H. Rudigier, Z. Fisk, J. O. Willis, G. R. Stewart, *Specific Heat And Resistivity of $CeCu_6$ below 1 K*, Solid State Comm., **53**, 235 (1985).

[50] H. Tsujii, E. Tanaka, Y. Ode, T. Katoh, T. Mamiya, S. Araki, R. Settai, Y. Onuki, *Magnetic Order in the Heavy Fermion Compound $CeCu_6$ at mK Temperatures*, Phys. Rev. Lett., **84**, 5407 (2000).

[51] J. Rossat - Mignod, L. P. Regnault, J. L. Jacoud, *Inelastic Neutron Scattering Study Of Cerium Heavy Fermion Compounds*, J. Magn. Magn. Mater., **76 & 77**, 376 (1988).

[52] B. Bogenberger, H. v. Löhneysen, *Tuning of Non - Fermi - Liquid Behaviour with Pressure*, Phys. Rev. Lett., **74**, 1016 (1995).

[53] H. v. Löhneysen, O. Stockert, M. Enderle, *Magnetic fluctuations at the field-tuned vs. concentration-tuned quantum phase transition in $CeCu_{6-x}Au_x$*, J. Magn. Magn. Mater., **0**, 1 (2006).

[54] O. Stockert, private communication, 2010, (Max-Planck-Institut für Chemische Physik fester Stoffe, Dresden, Germany).

[55] J. A. Hertz, *Quantum critical phenomena*, Phys. Rev. B, **14**, 1165 (1976).

[56] A. J. Millis, *Effect of a nonzero temperature on quantum critical points in itinerant fermion systems*, Phys. Rev. B, **48**, 7183 (1993).

[57] T. Moriya, T. Takimoto, *Anomalous Properties around Magnetic Instability in Heavy Electron Systems*, J. Phys. Soc. Jpn., **64**, 960 (1995).

[58] D. Belitz, T. R. Kirkpatrick, J. Rollbühler, *Tricritical Behavior in Itinerant Quantum Ferromagnets*, Phys. Rev. Lett., **94**, 247205 (2005).

[59] A. Rosch, A. Schröder, O. Stockert, H. v. Löhneysen, *Mechanism for the Non - Fermi - Liquid Behavior in $CeCu_{6-x}Au_x$*, Phys. Rev. Lett., **79**, 159 (1997).

[60] A. Schröder, G. Aeppli, E. Bucher, R. Ramazashvili, P. Coleman, *Scaling of Magnetic Fluctuations near a Quantum Phase Transition*, Phys. Rev. Lett., **80**, 5623 (1998).

[61] A. Schröder, G. Aeppli, R. Coldea, M. Adams, O. Stockert, H. v. Löhneysen, E. Bucher, R. Ramazashvili, P. Coleman, *Onset of Antiferromagnetism in Heavy - Fermion Metals*, Nature, **407**, 351 (2000).

[62] P. Coleman, C. Pépin, Q. Si, R. Ramazashvili, *How do Fermi Liquids get heavy and die ?*, J. Phys.: Condens. Matter, **13**, R 723 (2001).

[63] Q. Si, S. Rabello, K. Ingersent, J. L. Smith, *Locally critical quantum phase transitions in strongly correlated metals*, Nature, **413**, 804 (2001).

[64] A. Schröder, J. W. Lynn, R. W. Erwin, M. Loewenhaupt, H. v. Löhneysen, *Magnetic structure of the heavy fermion alloy $CeCu_{5.5}Au_{0.5}$*, Physica B, **199 & 200**, 47 (1994).

[65] H. v. Löhneysen, A. Neubert, T. Pietrus, A. Schröder, O. Stockert, U. Tutsch, M. Loewenhaupt, A. Rosch, P. Wölfle, *Magnetic order and transport in the heavy-fermion system $CeCu_{6-x}Au_x$*, Eur. Phys. J. B, **5**, 447 (1998).

[66] M. Sieck, F. Huster, H. v. Löhneysen, *Uniaxial pressure dependence of the Néel temperature in $CeCu_{5.8}Au_{0.2}$*, Physica B, **230 - 232**, 583 (1997).

[67] H. Okumura, K. Kakurai, Y. Yoshida, Y. Onuki, Y. Endoh, *Magnetic structure of $CeCu_{6-x}Au_x$*, J. Magn. Magn. Mater., **177 - 181**, 405 (1998).

[68] H. v. Löhneysen, H. Bartolf, S. Drotziger, C. Pfleiderer, O. Stockert, D. Souptel, W. Löser, G. Behr, *Rare-earth intermetallic compounds at a magnetic instability*, J. All. Comp., **9**, 408 (2006).

[69] K. McElroy, *Death of a Fermi surface*, Nature, **2**, 441 (2006).

[70] B. Keimer, A. Aharony, A. Auerbach, R. J. Birgeneau, A. Cassanho, Y. Endoh, R. W. Erwin, M. A. Kastner, G. Shirane, *Néel transition and sublattice magnetization of pure and doped La_2CuO_4*, Phys. Rev. B, **45**, 7430 (1992).

[71] C. Niedermayer, C. Bernhard, T. Blasius, A. Golnik, A. Moodenbaugh, J. I. Budnick, *Common Phase Diagram for Antiferromagnetism in $La_{2-x}Sr_xCuO_4$ and $Y_{1-x}Ca_xBa_2Cu_3O_6$ as Seen by Muon Spin Rotation*, Phys. Rev. Lett., **80**, 3843 (1998).

[72] D. Reznik, L. Pintschovius, *Electron-Phonon Anomaly Related to Charge Stripes: Static Stripe Phase Versus Optimally Doped Superconducting $La_{1.85}Sr_{0.15}CuO_4$*, J. Low Temp. Phys., **147**, 353 (2007).

[73] L. Pintschovius, D. Reznik, K. Yamada, *Oxygen phonon branches in overdoped $La_{1.7}Sr_{0.3}Cu_3O_4$*, Phys. Rev. B, **74**, 174514 (2006).

[74] S. L. Chaplot, W. Reichardt, L. Pintschovius, N. Pyka, *Common interatomic potential model for the lattice dynamics of several cuprates*, Phys. Rev. B, **52**, 10 (1995).

[75] J. M. Tranquada, B. J. Sternlieb, J. D. Axe, Y. Nakamura, S. Uchida, *Evidence for stripe correlations of spins and holes in copper oxide superconductors*, Nature, **375**, 561 (1995).

[76] J. M. Tranquada, *Handbook of High-Temperature Superconductivity Theory and Experiment, chapter 6: Neutron Scattering Studies of Antiferromagnetic Correlations in Cuprates* (Springer, New York, 2007).

[77] K. Yamada, C. H. Lee, K. Kurahashi, J. Wada, S. Wakimoto, S. Ueki, Y. Kimura, Y. Endoh, S. Hosoya, G. Shirane, R. J. Birgeneau, M. Greven, M. A. Kastner, Y. J. Kim, *Doping dependence of the spatially modulated dynamical spin correlations and the superconducting-transition temperature in* $La_{2-x}Sr_xCuO_4$, Phys. Rev. B, **57**, 10 (1998).

[78] N. Ichikawa, S. Uchida, J. M. Tranquada, T. Niemöller, P. M. Gehring, S. H. Lee, J. R. Schneider, *Local Magnetic Order vs Superconductivity in a Layered Cuprate*, Phys. Rev. Lett., **85**, 1738 (2000).

[79] M. Ito, Y. Yasui, S. Iikubo, M. Soda, M. Sato, A. Kobayashi, K. Kakurai, *Effects of 'stripes' on the magnetic excitation spectra of* $La_{1.48}Nd_{0.4}Sr_{0.12}CuO_4$, J. Phys. Soc. Jpn., **72**, 1627 (2003).

[80] M. Fujita, H. Goka, K. Yamada, J. M. Tranquada, L. P. Regnault, *Stripe order, depinning, and fluctuations in* $La_{1.875}Ba_{0.125}CuO_4$ *and* $La_{1.875}Ba_{0.075}Sr_{0.050}CuO_4$, Phys. Rev. B, **70**, 104517 (2004).

[81] J. Zaanen, O. Gunnarson, *Charged magnetic domain lines and the magnetism of high-*T_c *oxides*, Phys. Rev. B, **40**, 7391 (1989).

[82] K. Machida, *Magnetism in* La_2CuO_4 *based compounds*, Physica C, **158**, 192 (1989).

[83] S. A. Kivelson, I. P. Bindloss, E. Fradkin, V. Oganesyan, J. M. Tranquada, A. Kapitulnik, C. Howald, *How to detect fluctuating stripes in the high-temperature superconductors*, Rev. Mod. Phys., **75**, 1201 (2003).

[84] E. Kaneshita, M. Ichioka, K. Machida, *Phonon Anomalies due to Collective Stripe Modes in High* T_c *Cuprates*, Phys. Rev. Lett., **88**, 11 (2002).

[85] D. Reznik, L. Pintschovius, M. Ito, S. Iikubo, M. Sato, H. Goka, M. Fujita, K. Yamada, G. D. Gu, J. M. Tranquada, *Electron-phonon coupling reflecting dynamic charge inhomogeneity in copper oxide superconductors*, Nature, **440**, 1170 (2006).

[86] M. Fujita, K. Yamada, H. Hiraka, P. M. Gehring, S. H. Lee, S. Wakimoto, G. Shirane, *Static magnetic correlations near the insulating-superconducting phase boundary in* $La_{2-x}Sr_xCuO_4$, Phys. Rev. B, **65**, 064505 (2002).

[87] M. Braden, private communication, 2010, (II. Physikalisches Institut, Universität zu Köln, Germany).

[88] B. G. Dick, A. W. Overhauser, *Theory of the Dielectric Constants of Alkali Halide Crystals*, Phys. Rev., **112**, 90 (1958).

[89] L. Pintschovius, private communication, 2010, (Institut für Festkörperphysik, Karlsruhe Institute of Technology (KIT), Germany).

[90] D. Reznik, L. Pintschovius, J. M. Tranquada, M. Arai, Y. Endoh, T. Masui, S. Tajima, *Temperature dependence of the bond-stretching phonon anomaly in* $YBa_2Cu_3O_{6.95}$, Phys. Rev. B, **78**, 094507 (2008).

[91] X. Zhao, G. Yu, Y.-C. Cho, G. Chabot-Couture, N. Barisic, P. Bourges, N. Kaneko, Y. Li, L. Lu, E. M. Motoyama, O. P. Vajk, M. Greven, *Crystal Growth and Characterization of the Model High-Temperature Superconductor* $HgBa_2CuO_{4+\delta}$, Adv. Materials, **18**, 3243 (2006).

[92] L. Pintschovius, D. Reznik, W. Reichardt, *Oxygen phonon branches in* $YBa_2Cu_3O_7$, Phys. Rev. B, **69**, 214506 (2004).

[93] R. Heid, private communication, 2008, (Institut für Festkörperphysik, Karlsruhe Institute of Technology (KIT), Germany).